Chapter 7
Distributed Radioactivities

Roland Diehl, Dieter H. Hartmann, and Nikos Prantzos

Radioactive nuclei freshly produced in compact sources of cosmic nucleosynthesis are ejected into the source surroundings. Then, their decay may be directly observable through characteristic gamma-ray lines, or they may be transported directly to a terrestrial detector. Also, condensation into dust and solids may occur, and then freeze the composition of gas at the dust formation site, which can be inferred from such stardust as found in meteorites. The intrinsic clocks provided by the radioactive decay of each isotope then provide a tool to investigate the characteristics of transport away from the sources, and through interstellar medium, and in the solidification and planet formation phase of our solar system around its earliest history. In this Chapter we discuss what radioactive isotopes such as ^{26}Al, ^{60}Fe, ^{129}I, ^{59}Ni, but also very heavy element isotopes such as ^{244}Pu, or positrons from β^+ decay can teach us about sources and transport of radioactive nuclei.

7.1 Radioactivities in the Interstellar Medium

Radioactive isotopes are ejected into the surroundings of their sources, and become observable through their gamma-ray line emission once having left dense production sites where not even gamma-rays may escape. Thus, radioactivity sources of

R. Diehl (✉)
Max Planck Institut für extraterrestrische Physik, Garching, Germany
e-mail: rod@mpe.mpg.de

D. H. Hartmann
Clemson University, Clemson, SC, USA
e-mail: hdieter@g.clemson.edu

N. Prantzos
Institut d'Astrophysique, Paris, France
e-mail: prantzos@iap.fr

R. Diehl et al. (eds.), *Astrophysics with Radioactive Isotopes*, Astrophysics and Space Science Library 453, https://doi.org/10.1007/978-3-319-91929-4_7

gamma-ray lines are *diffuse* by this very nature. A second path for us as observers arises when dusts and solids form in interstellar space, and include radioactive nuclei: The composition of such solids as frozen in at their formation is altered from radioactive decay, and recognition of daughter isotopes thus tells us about the radioactivity in the surroundings of the dust/solid formation site.

In this Chapter, we discuss such radioactivities as seen or inferred in interstellar space, tracing them back to their sources, and extracting what they may tell us about the links between sources and interstellar medium. Complementing the discussions of isotopes which originate from single sources (the short-lived isotopes) in Chaps. 3–5, here we address the ejections of sources as accumulated in interstellar space. The radioactive lifetime of each of these isotopes is related to its specific role in astrophysical research (see Table 1.1 in the Introduction of this book).

When the lifetime of a radioactive nucleus is not very large compared to the timescale of its propagation away from its source into interstellar space, we may not be able to distinguish between a point source and a diffuse source. This depends also on the resolving power of the observing instrument, i.e. diffuse emission is seen if typical distances—projected on the sky—between point sources are larger than the instrument's resolution. Our definition of *diffuse* here attempts to focus on the physical connection between the source and what we observe: When the observed source is identical to the object of our study, we call this a *point source*. Examples are novae, supernovae, and type-I X-ray bursts, and are addressed in Chaps. 4 and 5. When the observed source includes a transport process between the production site of radioactivity and its observational manifestation, we call this a *diffuse source or emission*.

Key isotopes and their specific astrophysical implications are summarised here first:

- ^{56}Ni and ^{44}Ti isotopes decay as the supernova that produced them explodes and expands into a supernova remnant. The emerging gamma rays from the ^{56}Ni decay chain, with radioactive lifetimes of 8.8 days (^{56}Co* lines) and 111 days (^{56}Fe* lines), primarily tell us about how the supernova unfolds and dilutes after explosion. This information is convolved with the known radioactive clock of the decays. A supernova becomes transparent to gamma rays within a few months. Late emission from ^{56}Co and ^{44}Ti decay, therefore, tells us about the total amount of radioactivity produced in the source, and about ejecta kinematics and spatial distribution. Comparing to other radiation measured from the remnant, the amount of radioactive energy deposit and the remnant leakage of positrons from β^+ decay can be inferred. All of these are properties related more to the source rather than to circum- or interstellar medium. Therefore, the sources of these isotopes and their science are not considered 'diffuse', and are therefore discussed in preceding Chaps. 4 and 5. Also, short-lived actinides and lanthanides, which are inferred to power light from neutron star collisions in the form of macro-novae (also called kilonovae; see Chap. 4), belong into this characteristic class of radioactivities that radiate from an expanding explosive nucleosynthesis source. They are mentioned here to illustrate the key aspect of

astronomy with radioactive nuclei: an emission with known characteristics and energy output, leaving behind material that was not present originally.

- ^{26}Al and ^{60}Fe have radioactive decay times of 1.04 and 3.8 My, respectively. Therefore, they may safely assumed to have left their production sites. The dispersal of nucleosynthesis ejecta from a single source can be traced over a time scale of millions of years, from observing their decay or daughter isotopes. This is approximately the time scale expected to characterise the return of stellar gas through an explosive event into the ambient interstellar gas in the source surroundings. One of the questions addressed would be how far out in space away from the source ejecta may travel within a few My. Another question would be if the dispersal shows any preferred directions, such as possibly escape flows from the galactic-plane (*chimneys*). Yet another aspect is the state of circum-source, hot interstellar medium with cavities of age 1 My or younger, yet older than the 0.1 My scale which can be addressed through observations of gas in supernova remnants by observations of atomic transitions in partly-ionized plasma. Measuring the width of radioactive-decay gamma-ray lines encodes turbulence and bulk flow through Doppler broadening and shifts of the gamma-ray lines, respectively. These long-lived isotopes ^{26}Al and ^{60}Fe are neither part of the *light-element* family (originating from primordial or cosmic-ray spallation nucleosynthesis) nor of the *heavy-element* family (originating from probably explosive sites with extreme densities of matter, energy, and neutrons). Rather, ^{26}Al and ^{60}Fe most likely originate from (normal and frequent/omnipresent) stellar sources, hence from nuclear reactions inside stars with contributions from their terminal explosions. But the explosions mainly help to eject stellar matter into interstellar space, while their contribution to production probably is sub-dominant (see Chaps. 3 and 4). Thirty years of gamma-ray and meteoritic measurements carried the celestial signal from ^{26}Al decay through a history from *establishing proof of past and current nucleosynthesis* in the Galaxy to *identifying ^{26}Al origin* predominantly from massive stars into an *astronomical tool* for the study of massive-star/ISM interactions in nearby stellar groups.
- Isotopes such as ^{129}I, ^{146}Sm, ^{182}Hf, and ^{244}Pu are parent radioactivities inferred to have existed once in the early solid material that formed the Earth. They are rather long-lived with decay lifetimes of 23–115 Myrs, but *extinct* and only evident through their characteristic decay products. The isotopic composition of solids of different formation times thus reveal characteristic anomalies, found through precision mass spectroscopy in terrestrial laboratories. The inferred existence of those radioactivities thus tell us about pre-solar nucleosynthesis in the surroundings accessible to interstellar transport during the radioactive lifetime of each isotope. Early-solar system astrophysics involving homogeneity and effectiveness of mixing before first meteorites were formed can be addressed by 'shortlived' (0.1-few My) radioactivities, including the above-mentioned ^{26}Al and ^{60}Fe, but also ^{10}Be, ^{36}Cl, ^{41}Ca, and ^{53}Mn. Probes on a somewhat longer time scale are ^{129}I, ^{146}Sm, ^{182}Hf, and ^{244}Pu. This application of radioactivity focuses on the early solar system, hence is dealt with in detail in the book's Chap. 6 dedicated to the Solar System.

- The even more long-lived (>100 My) radioactivities of ^{187}Re, ^{235}U, ^{238}U, ^{232}Th connect us to nucleosynthesis at cosmic time scales. They provide age dating nucleosynthesis since the formation of the Galaxy, and also dating of the age of the solar system. Therefore you find more details in book Chaps. 2 and 6.
- ^{59}Ni is an example of a useful subclass of radioactive isotopes, which can decay only through electron capture. Therefore, its decay implies an environment of incomplete if any ionization, i.e., an environmental temperature below 10^5 K. Cosmic ray nuclei are characterised by the other extreme, they are relativistic and always fully ionized. Therefore, the observed abundance of ^{59}Ni in cosmic ray nuclei directly encodes the delay time between nucleosynthesis of this ^{59}Ni ($\tau_{decay} \sim 10^5$ years) and its acceleration to cosmic-ray energies (and hence full ionization) (see Sect. 7.4). ^{57}Co and ^{56}Ni are more-shortlived electron-capture only radio-isotopes, similarly useful to constrain the times between their ionization and recombination. Here, the property of radioactivity (the clock) combines with (otherwise usefully-unimportant, but here diagnostic impact) of the atomic shell. More sophisticated analysis is required to understand the cosmic-ray abundances of unstable isotopes which include electron capture as a main decay mechanism, such as ^{7}Be, ^{49}V, ^{51}Cr, and ^{55}Fe: Their abundances result from how much of their trajectory had involved low energies with chances to attach electrons. Hence they address the topic of cosmic-ray re-acceleration and/or successive cosmic-ray acceleration by different shock regions along their journey.
- In direct detections of cosmic rays also radioactive species and their abundances can be measured. The observed abundance, e.g. as seen for ^{60}Fe, can be combined with known production cross sections for spallation reactions to determine the distance to the source, that is, the effectively-traversed path length of cosmic rays producing such abundance from collisions with ambient interstellar gas. Cosmic-ray isotopes ^{10}Be, ^{26}Al, ^{36}Cl, and ^{54}Mn have thus been used to constrain the time spent in the Galaxy to $\sim 10^7$ years, while the more-shortlived ^{60}Fe was attributed to supernova explosions rather nearby and recent (see Sect. 7.4).
- Positrons produced in various radioactive decays add interesting aspects. Their propagation properties as charged particles are reminiscent of cosmic rays: they will be directed by the morphology of the magnetic field, and will lose energy in collisions with ambient gas. Their annihilation provides a characteristic gamma-ray signature, thus making positrons a rather special astronomical messenger. Annihilation is favoured in a rather narrow energy range between ~7 and 200 eV (corresponding to temperatures in the 1000 K regime). This makes positron annihilation gamma rays special probes of this phase of the interstellar medium. On the other hand, positrons from radioactive decays may deposit radioactive energy efficiently in expanding envelopes from stellar explosions, and their abundance in interstellar space must reflect a significant contribution from nucleosynthesis from a variety of sources, and throughout the Galaxy. This yields information which complements other observables of the same radioactive decays (e.g. bolometric broad-band emission, or ^{26}Al-decay gamma-rays). Even

though there are other candidate sources of positrons, the research with positrons and their annihilation is included in this Chapter (see Sect. 7.5).

In the following, we discuss candidate sources with their astrophysical and nuclear-reaction aspects, then their observations are presented, and we close the treatment with a summary of the lessons learned and the remaining questions.

7.2 ^{26}Al

7.2.1 Nuclear Reactions, Candidate Sources, and Observability

^{26}Al is produced by proton capture on ^{25}Mg, the ^{25}Mg (p,γ) ^{26}Al reaction that is characteristic for hydrogen burning (Iliadis et al. 2011). Pre-existing ^{25}Mg is processed in this way, although more-abundant ^{24}Mg could also be transferred into ^{25}Mg by proton capture and successive β decay. The amount of ^{26}Al thus depends on pre-existing Mg, and scales with the metallicity of the star as it was formed. In principle, such hydrogen-burning environments may further process ^{26}Al by proton capture into ^{27}Si; but the rising Coulomb repulsion makes this destruction channel rather negligible (see experimental constraints and discussion by Parikh et al. 2014), compared to the neutron capture reactions that may destroy ^{26}Al through ^{26}Al(n, p)^{26}Mg and ^{26}Al(n, α)^{23}Na. The ^{27}Al(p, α)^{24}Na reaction will close a nuclear-reaction cycle against further nuclear reaction flow towards heavier isotopes. This avoids loss of nucleons away from locking them into the cycle around ^{26}Al and its neighbouring isotopes, as long as the leakage reaction from that cycle ^{27}Al(p, γ)^{28}Si proceeds at a low rate. Within this reaction cycle, shown in Fig. 7.1, an equilibrium abundance of ^{26}Al would be established, balancing production and destruction reaction flows. Due to its relative stability (lifetime against β decay is 1.04×10^6 years), the ^{26}Al abundance in such an equilibrium is rather high and comparable to the Mg isotopes. In explosive environments, only the charged-particle and photon reactions are dominant, as the dynamics of the explosion disfavours the slower β decay reactions.

In sufficiently-hot environments, ^{26}Al may be thermally excited to its higher levels at excitation energies of 228, 417, and 1058 keV with spin states 0+, 3+, and 1+, respectively. Although only the high-energy tail of the thermal distribution will make such excitations possible, the daughter spin states of ^{26}Mg (2+ for the excited state at 1809 keV, 0+ for the ground state) allow much higher transition rates than the highly-forbidden transition from ^{26}Al's ground state with spin 5+ to any of the two Mg states. Therefore, in hot environments, the excited states of ^{26}Al must be included in a nuclear reaction network, and lead to a much larger destruction of ground state ^{26}Al; ^{26m}Al decays in just 0.109 s. Thermal excitation with subsequent rapid decay of ^{26}Al^m through this energy level of ^{26}Al at 228 keV excitation energy thus becomes relevant at T $\geq$ 0.1 10^9 K, adding destruction channels to the otherwise dominant neutron capture reactions. For ^{26}Al, a lifetime

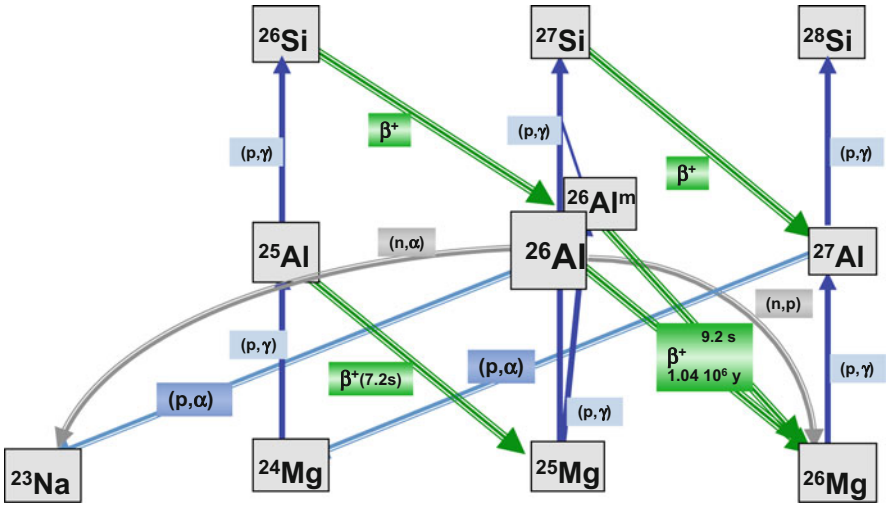

Fig. 7.1 The Na-Al-Mg reaction cycle, characterised by proton capture reactions and β decays, mainly, and closed by a (p,α) reaction (after Prantzos and Diehl (1996), Fig. 3.1)

of 1.042×10^6 years (or, equivalently, a half-life of 722,000 years) is obtained from averaging over four independent measurements; the value recommended in the *Table of Isotopes* is (1.034 ± 0.046) My, Endt 1990).

In principle, all hydrogen-burning environments are expected to process pre-existing ^{25}Mg into ^{26}Al. Depending on these other reactions occurring in those environments, the yield of a particular source can vary substantially. Mixing processes among regions containing Mg seeds and hydrogen, as well as rapid convective transport away from the hot zones and thus avoiding destruction reactions, all have important impact on the final ^{26}Al yields (see Chap. 3). Here, 'yield' defines the amount of ^{26}Al that emerges from the source. Therefore, core hydrogen burning in stars less massive than several $M_\odot$ is unimportant, as any ^{26}Al produced during main sequence hydrogen burning will decay before any interior material could be ejected in a giant phase (see Chap. 3). But for stars more massive than about 3 $M_\odot$, shell hydrogen burning further out becomes interesting. Modeling convective overturn may implement the *Schwarzschild criterion* where buoyancy of a homogeneous gas mixture is compared to restoring forces from pressure gradients (gravity and thermal), or the *Ledoux criterion* where the net effect of all restoring forces is evaluated, including chemical-diffusion gradients. More complexity may be added by chemical-diffusion gradient, which leads to *thermohaline mixing* or *semiconvection*, depending on the direction of dominance of between chemical-diffusion gradient and thermal gradient forces. Stellar rotation brings in exchanges between local and global angular momenta inside a star, adding other origins of mixing processes. This has been shown to be an important ingredient, significantly enhancing mixing and transport of fuel and ashes into and away from the nuclear

reaction regions within a star. As a result, typically the inclusion of stellar rotation enhances the amounts of ejected ^{26}Al (Palacios et al. 2005). Also in the Ne-O layers, where ^{25}Mg nuclei are abundant from Ne-burning reactions, and protons may be produced by (X, p) reactions, ^{26}Al may be produced through hydrogen burning. Stellar structure instabilities are characteristic of those more-massive stars in their evolution along the asymptotic giant branch (AGB), as Luminous Blue Variables (LBV), and more-intense mass ejections during those evolutionary phases help to make them candidate sources of interstellar ^{26}Al. An ambient-medium abundance of ^{25}Mg of log(Mg) = 6.6 (where log(H) = 12) (Asplund et al. 2009, solar abundance assumed for the current Galaxy) would thus be available for ^{26}Al synthesis in more-massive stars; for hotter environments, more abundant ^{24}Mg (abundance of log(Mg) = 7.49) may provide ^{26}Al fuel as well, as it is processed into ^{25}Mg through p capture reaction and intermediate β-decay.

Also in stellar explosions, novae (Chap. 5) and core-collapse supernovae (Chap. 4), explosive nucleosynthesis of ^{26}Al may occur, as stellar plasma is heated by the explosion shock wave to temperatures where protons are released and may undergo nuclear reactions on ambient ^{25}Mg nuclei. The intense flux of neutrinos from the collapsed stellar core may produce additional ^{26}Al depending on the poorly known average neutrino energy (Woosley and Weaver 1995)—a process that has not been included in many ^{26}Al source models yet. These neutrino reactions on infalling material in the region close to the proto-neutron star result in a *neutrino process* , releasing nucleons (protons, neutrons, α particles) from heavier nuclei, and thus enabling ^{26}Al synthesis on Mg again. It has been estimated that this could enhance ^{26}Al yields by 20–30% (Sieverding et al. 2017).

In interstellar space, nuclear reactions occur from cosmic ray collisions with ambient gas. Cosmic rays predominantly have a nucleonic component, with protons and nuclei as heavy as iron, while electrons are a small contribution at the percent level. If energetic nuclei collide with interstellar gas, they will be broken up and fragment into lighter nuclei such as ^{26}Al. Similarly, heavy nuclei in interstellar gas will be broken up by collisions with any component of energetic cosmic rays. Such spallation reactions therefore may produce ^{26}Al—either from heavy-nuclei cosmic rays being broken up or from ambient-gas nuclei being broken up to produce ^{26}Al with its 13 nucleons only. The cross sections for such reactions are rather well known, and thus, yields have been estimated for plausible cosmic-ray intensities and interstellar medium parameters (Ramaty et al. 1979). From this, the cosmic-ray produced ^{26}Al appears to be several orders of magnitude below detectability by gamma ray telescopes.

The amount of ^{26}Al ejected into the interstellar medium depends on many ingredients of the process from its production until release from the star. Typical values are 10^{-5} to 10^{-4} $M_\odot$ (see Fig. 4.20). Several factors within stellar models play a significant role:

Theoretical predictions ^{26}Al yields from models of massive stars and their supernovae have been provided by Woosley and Weaver (1995), Timmes et al. (1995), Thielemann et al. (1996) and Limongi and Chieffi (2006b, the 'first-generation' models), the Wolf-Rayet contributions which crucially depend on mass

loss properties were discussed in specific detail by Palacios et al. (2005), later the aspects of stellar rotation and lessons from 3D considerations were included (Meynet et al. 2006; Ekström et al. 2012; Chieffi and Limongi 2013). Extended sets of model yields for stars of masses up to 120 $M_\odot$ are available from Ekström et al. (2012), Chieffi and Limongi (2013), Pignatari et al. (2016) and Sukhbold et al. (2016) (see also Chap. 4). For the less massive AGB stars, yields from Meynet et al. (1997, first generation) with a recent detailed treatment by Karakas and Lattanzio (2014) (see also Chap. 3). Nova contributions to ^{26}Al are addressed by Jose and Hernanz (1998) and Gehrz et al. (1998) (see also Chap. 5).

It turned out that, from all these candidate sources, massive stars such as Wolf-Rayet and possibly the high-mass fraction of AGB stars, and the core-collapse supernovae that mark the end points of their evolution, very likely dominate above the other candidate sources in producing interstellar ^{26}Al (see the detailed discussion of observational results below, and considerations on astrophysical source models as presented in Chaps. 3–5).

A supernova explosion will obviously disperse ejecta in the interstellar medium, including ^{26}Al as the synthesis occurs in outer regions (the O/Ne shell), far above the inner supernova core where some material may fall back onto the remnant star or black hole. ^{26}Al produced hydrostatically in stars is ejected only in two possible ways: Either the supernova explosion occurs sufficiently soon after its production so that it still has not decayed, or else convective transport within the star will bring it up to the surface and a sufficiently-strong wind will carry it away from the star. Two types of stars fulfill the latter conditions: In asymptotic-giant branch stars (AGB), ashes from hydrogen-shell burning are brought to the surface, the convective shell may be a *hot-bottom*-producer of ^{26}Al (see Chap. 3). Alternatively, core hydrogen-burning ashes from the Helium shell are revealed in the strong winds of the massive-stars' Wolf-Rayet phase, in a later stage of this phase after the hydrogen envelope has been stripped (see Chap. 4).

Once transported away from the site of its production and of any further nuclear reactions, ^{26}Al will β-decay with its 1.04 Myr-lifetime (see Fig. 1.3 in the Introduction of this book). ^{26}Al decay produces a characteristic gamma-ray line signature. From above-mentioned spin states and selection rules, decay is inhibited, leading to its relative stability with τ 1.04 $\times$ 10^6 years. In 99.76% of all decays, a gamma-ray photon of energy 1808.63 keV ($\pm$0.07 keV uncertainty) is emitted. 82.1% of decays are β^+-decays which also emit a positron, the remainder of decays occur through capture of an electron from the atomic shell. Photon yields at 1130 (2.4% of decays) and 2938 keV (0.24 of decays) are weak by comparison with the 1808.63 keV line, and the photon yield from positron annihilation ($\simeq$1.6 photons of 511 keV, depending on annihilation conditions) is more indirect, as the positron's lifetime depends on gas and magnetic-field conditions and can reach the order of 10^5 years (Jean et al. 2009).

7.2.2 *Observations of ^{26}Al*

The first report of a gamma-ray line from a radioactive nucleus of cosmic origin arose from the HEAO-C instrument's 1979/1980 measurements, from a satellite mission carrying a Ge detector which located a line at 1809 keV and plausibly attributed it to decay of live ^{26}Al in the Galaxy's interstellar medium (Mahoney et al. 1984). ^{26}Al radioactive decay within 1 My requires a source within the past million years, which is a rather brief recent time span in the Galaxy's history which spans 12 Gy or more. Therefore this is proof of currently-ongoing nucleosynthesis.

Independently, meteoritic studies had shown (Schramm et al. 1970; Lee et al. 1976; Wasserburg et al. 1977) an excess of the abundance of ^{26}Mg in Al-rich inclusions, which pointed to an earlier existence of the ^{26}Al parent isotope in the aluminium minerals at the time this material had condensed (see discussion in MacPherson et al. 1995, for consolidated meteoritic results). It turned out that ^{26}Al is among the most informative nucleocosmochonometers to study the formation of first solids in the young, pre-solar, nebula (Srinivasan and Chaussidon 2013, see also Chapter 6). The origin of ^{26}Al in the early solar nebula remained unclear, and a subject of (see Chap. 6). With improvements of methods to study also different components within meteorites, in particular refractory SiC grains, ^{26}Al traces were also found in inclusions in meteorites which are clearly not of solar-system origin, and called 'stardust' (Nittler et al. 2008). Their origins could be related to an origin in AGB stars, from isotope ratios in C, N, Si, and Al (see Chaps. 3 and 10).

The COMPTEL sky survey, accumulated over 9 years, then provided a sky image in the ^{26}Al gamma-ray line. This reflects a map of nucleosynthesis activity in our current Galaxy.[1] The resulting ^{26}Al map showed structured ^{26}Al emission, extended along the plane of the Galaxy (Plüschke et al. 2001a; Knödlseder et al. 1999; Oberlack et al. 1996; Diehl et al. 1995) (see Fig. 7.2), in broad agreement with earlier expectations of ^{26}Al being produced throughout the Galaxy and mostly from massive stars and their supernovae (Prantzos 1993; Lingenfelter and Ramaty 1978).

COMPTEL's detectors lacked the spectral resolution required for line identification and spectroscopic studies, with $\simeq$200 keV instrumental resolution, compared to $\simeq$3 keV for Ge detectors, at the energy of the ^{26}Al line. A 1995 balloon experiment also carrying high-resolution Ge detectors had provided an indication that the ^{26}Al line was significantly broadened to 6.4 keV (Naya et al. 1996). This implied kinematic Doppler broadening of astrophysical origin of 540 km s^{-1}. Considering the 1.04×10^6 years decay time of ^{26}Al, such a large line width would naively translate into kpc-sized cavities around ^{26}Al sources or major fractions of ^{26}Al to be condensed on grains (Chen et al. 1997; Sturner and Naya 1999). The INTEGRAL space observatory was launched in 2002. With its Ge-detector based spectrometer SPI, it provided high-quality spectroscopic results (Fig. 7.3), adding a wealth of

[1] Exposure time is million years, while the Galaxy's age is 10–13 Gyrs.

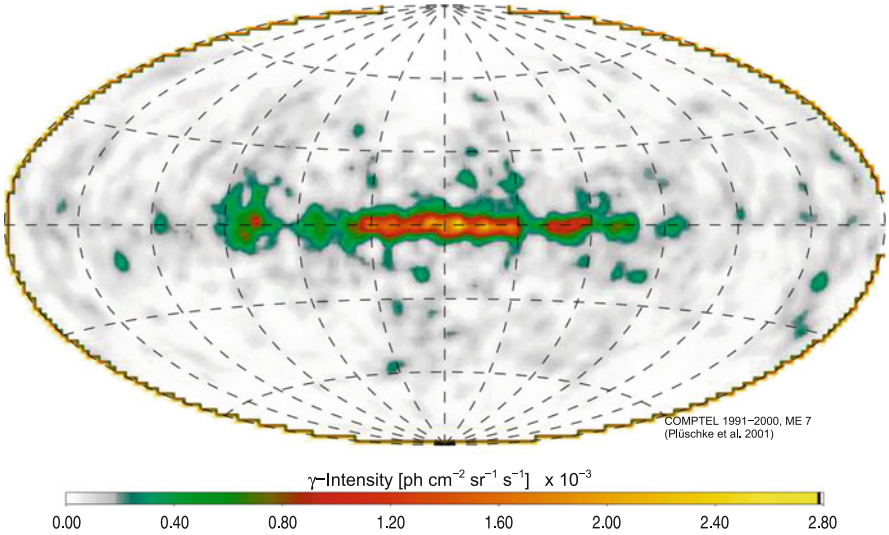

Fig. 7.2 The ^{26}Al sky as seen with the COMPTEL telescope. This image was obtained from measurements taken 1991–2000, and using a maximum-entropy regularization together with likelihood to iteratively fit a best image to the measured photons (from Plüschke et al. 2001)

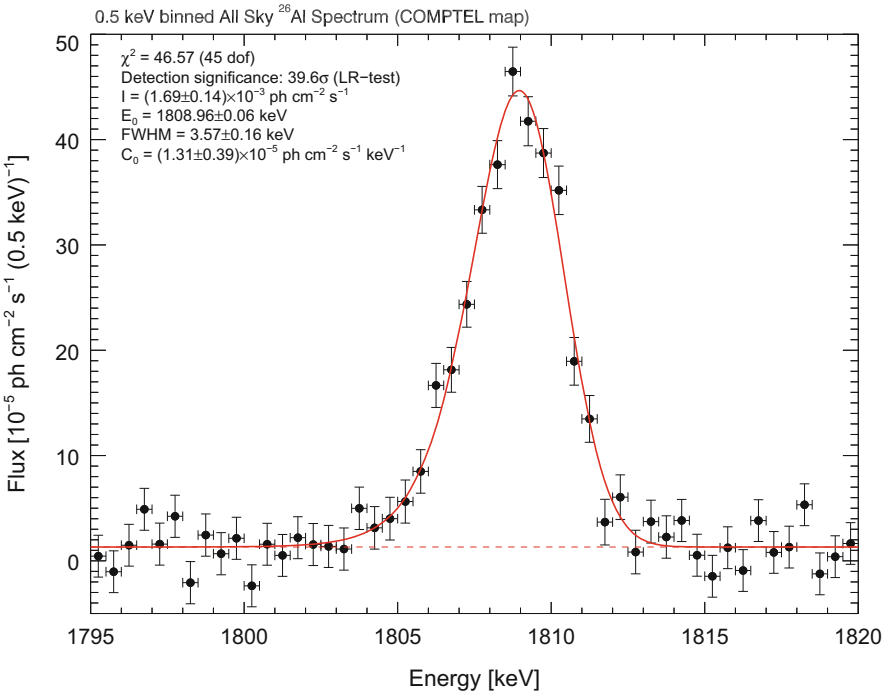

Fig. 7.3 The ^{26}Al line as seen with INTEGRAL's high-resolution spectrometer SPI and 13 years of measurements integrated (Siegert 2017)

detail from data accumulated over its more than 15-year long mission. This allowed not only higher precision study of the Galaxy-wide ^{26}Al aspects (Diehl et al. 2006a,b), but also the detailed test of our understanding of massive-star activity in specific and well-constrained massive star groups such as in Orion or Scorpius-Centaurus. Kinematic constraints from the ^{26}Al line width and centroid (Kretschmer et al. 2013), and multi-messenger studies using the stellar census and information on atomic and molecular has from radio data as well as hot plasma from X ray emission (Voss et al. 2009, 2010; Krause et al. 2013, 2014), all have led to a kind of ^{26}Al astronomy as part of the studies of stellar feedback and massive-star nucleosynthesis (e.g., Krause et al. 2015).

^{26}Al gamma-rays had established proof of current nucleosynthesis in our Galaxy. With better observations, this is now turned into an astronomical window of its own. The brightness of Galactic ^{26}Al emission allows measurement constraints not only from the integrated Galaxy's signal, but also for specific regions. A dream of cosmic nucleosynthesis studies through radioactivity gamma-ray lines had come true: Astrophysical models of massive stars and their evolution could be confronted with observations of source aggregates in our Galaxy to learn about validity of such models.

7.2.3 ^{26}Al Throughout the Galaxy

7.2.3.1 Large-Scale Aspects

The distribution of ^{26}Al emission on the sky and within the Galaxy hold the clues to the ^{26}Al sources. Already in HEAO-C data (Mahoney et al. 1984), it had been shown that an extended emission region in the inner Galaxy is plausible, rather than assuming a point-like source or an assembly of such The COMPTEL image (Fig. 7.2) confirmed and firmly established the extended nature of ^{26}Al gamma-ray emission along the entire disk of the Galaxy.

The image shown in Fig. 7.2 is one of many possible representations of the celestial distribution of emission that are consistent with measurements. For an instrument with a rather broad instrumental imaging-response function from its Compton scattering measurement principle, and a large instrumental background, the process of image extraction, which is constrained by statistical fluctuations, also must include constraints from prior knowledge, in order to direct the otherwise under-determined imaging process. In the image shown, the two criteria are maximum likelihood (i.e., quality of the data fit to the image), and maximum image entropy, which prefers an image with least new information content. One of the alternative choices is to build up the image successively from largest to smaller scales, at each stage estimating statistical noise if the image were true already, and suppressing its effects in the iterative addition of next-finer spatial information; this obtains a smooth image, by design (Fig. 7.4, top). Many images would be consistent with the measured data, and careful evaluation of priors, biases, and systematics are important to judge the constraints on astrophysics.

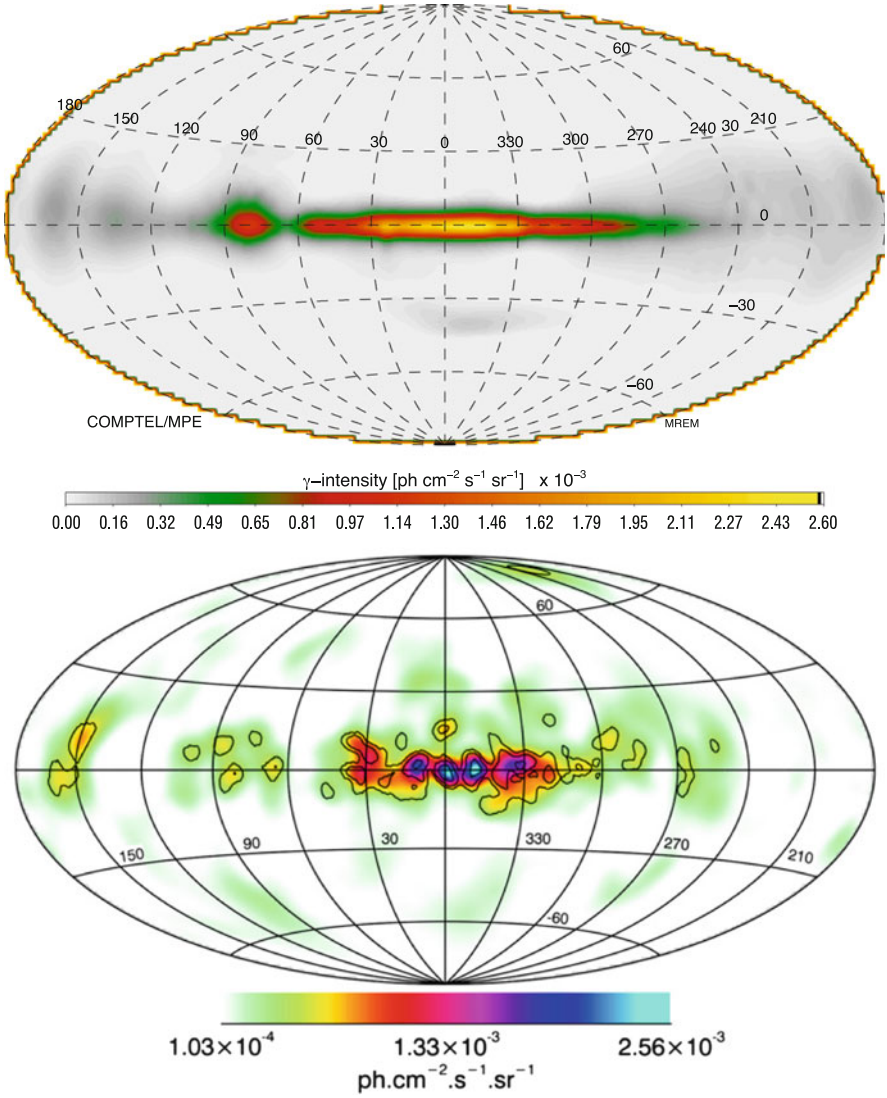

Fig. 7.4 *Top:* The ^{26}Al sky as deconvolved from the same data as shown in Fig. 7.2, now using a multi-resolution expectation maximization based on likelihood and wavelet-domain hierarchical noise filtering (Knödlseder et al. 1999). *Bottom:* The ^{26}Al sky as deconvolved from INTEGRAL's sky survey from 10 years of data with the SPI imaging spectrometer, and a maximum-likelihood imaging method (Bouchet et al. 2015)

Following the science principle of reproducibility of results, it is helpful to also have entirely-different instruments measuring the same celestial information. The spectrometer SPI on ESA's INTEGRAL space observatory features Ge detectors with high spectral resolution, and obtains its imaging information from a coded

mask shadow onto its hexagonal 19-detector camera. Although the sky exposure during the INTEGRAL mission was largely emphasised on the inner Galaxy, an all-sky image had been constructed from 10 years of data (Bouchet et al. 2015), shown in Fig. 7.4 (lower graph). This image also is potentially susceptible to systematics and uncertainties from the instrument, yet those will be different here. The total background count rate of this kind of instrument is much higher than for the Compton telescopes, and its imaging principle is more straightforward with a single interaction and detector type. The images show striking similarities, and several features of the ^{26}Al image shown in Fig. 7.2 reappear. In view of the different ways those images were obtained, we consider as confirmed that there is diffuse emission all along the plane of the galaxy, with emission peaks or hot spots reminiscent of known massive star groups.

The irregular distribution of ^{26}Al emission all along the plane of the Galaxy provided a main argument for the idea that massive stars dominate the production of ^{26}Al (Prantzos and Diehl 1996). Massive stars preferentially form in clusters; nearby massive-star regions appear prominent in ^{26}Al emission (e.g. the Cygnus region appears in all three images).

A Galaxy-wide interpretation of the ^{26}Al gamma-ray measurements needs to resolve the distance uncertainty when assigning a measured flux along a line of sight to source intensities. The possibility of localised regions which may efficiently produce ^{26}Al needs a proper account. Since the massive star census in the Galaxy is well known from astronomical measurements in thermal emission from those stars only out to distances of a few kpc, and many regions of the Galaxy are occulted for direct measurements, one is left with some uncertainty about their Galaxy-wide distribution. Probably, the *molecular ring* around the center of our Galaxy at a radial distance of 3–4 kpc from the center is a prominent birth site for massive stars, as are molecular clouds swept up along the Galaxy's spiral arms. The Doppler shift systematics for the ^{26}Al line as measured with INTEGRAL/SPI suggests that much or most of the ^{26}Al seen towards the inner Galaxy directions is taking part in large-scale Galactic rotation. Therefore, this ^{26}Al emission originates from sources at kpc distances reaching to the Galaxy's center and beyond, and thus are not local or foreground sources.

Supported by this, the total amount of ^{26}Al in the Galaxy can be estimated from the measured gamma ray flux, using as a plausible assumption for the distances to the emission regions a galaxy-wide distribution. This has been done by several authors, based on COMPTEL and on INTEGRAL data, and using as models smooth double-exponential disk models, or models including more structure such as spiral arms (such as Robin et al. 2003; Taylor and Cordes 1993). With such methods, an ^{26}Al amount between 1.5 and 3 $M_\odot$ is found, depending on data and models used; INTEGRAL/SPI data were used to obtain (2.8±0.8) $M_\odot$ of ^{26}Al (Diehl et al. 2006a) in a study comparing many alternative views of massive star activity in the Galaxy. A systematic limitation of any galaxy-wide parameter determination is potential local bias. Gamma rays are at an advantage here due to their penetrating nature, reaching us also from sources of the distant regions of our Galaxy. However, there may be sources in the vicinity of our vantage point in the solar system, 8 kpc from the

Galaxy's center. The Cygnus region is prominent as an ^{26}Al source, and, although with member associations at distances between 800 and 1500 pc (Plüschke et al. 2001b). The Gould Belt has been recognised as a region of local stellar associations arranged in an elliptical-belt-like structure(Olano 1982; Pöppel 1997; Pöppel et al. 2010; Maíz-Apellániz 2004; Perrot and Grenier 2003). Several member associations of the Gould Belt appear to be aligned with ^{26}Al emission peaks. In particular, the most-nearby association of Scorpius-Centaurus at merely 120–150 pc distance was detected as an ^{26}Al source with INTEGRAL (Diehl et al. 2010), supporting indications from COMPTEL. Accounting for such foreground sources leads to a reduction of the Galaxy-wide ^{26}Al content. Values range from $1.7 \pm 0.2\ M_\odot$ (Martin et al. 2009) to $2.0 \pm 0.3\ M_\odot$ (Diehl et al. 2010; Diehl 2016), depending on estimates of residual systematics uncertainty.

Such ^{26}Al mass determination based on observations sampling the *entire* Galaxy now allows a comparison with what would be expected from their candidate sources on theoretical grounds. Early predictions for supernovae from core collapse of massive stars were $2.1 \pm 1.1\ M_\odot$ (Timmes et al. 1995); the earlier Wolf-Rayet phase was estimated to contribute a galactic total of $0.5\,M_\odot$ with a factor $\sim$3 uncertainty (see Prantzos and Diehl 1996, and references therein). Uncertainties are due to the incomplete census of WR stars in our Galaxy (van der Hucht 2001) and metallicity dependence uncertainties. Recent models have assessed a Galactic contribution from WR stars of $\sim$0.6–1.4 $M_\odot$ (Palacios et al. 2005), accounting for new insights on impacts of stellar rotation and WR winds (see also Chap. 4). Models for these two candidate sources were best established, models for novae and AGB stars were uncertain, by comparison. Estimates for novae ranged from 0.1 to $5\,M_\odot$ with large uncertainties, mainly from a lack of progenitor knowledge, and from lacking still an also quantitatively-realistic nova model. About $0.2\ M_\odot$ of Galactic ^{26}Al may be due to classical novae, with again a factor $\sim$3 uncertainty (see Jose and Hernanz 1998, for a description of nova nucleosynthesis, but Chapter 5 presents an updated discussion in detail). Although AGB stars were once thought to be possibly important ^{26}Al sources (e.g. Forestini and Charbonnel 1997), their contribution is presently estimated (Karakas and Lattanzio 2014) to be below 10% of that of massive stars (see Chap. 3). Note that both AGB stars and novae are clearly identified as ^{26}Al producers from interstellar-grain inclusions in meteorites (see Clayton and Nittler 2004, for a review, and Chapters 3,5). Both these two types of sources are copious dust producers, more so than supernovae or WR stars; interstellar grain samples are biased towards measuring dust-producing sources. But in summary, none of the ^{26}Al sources discussed so far can be ruled out, based on such global, galaxy-wide considerations.

We now conclude at least that massive stars are the *dominating* contributors. Then we may use their theoretical yield estimates per mass and integrate over the mass distribution function to compare with the observed ^{26}Al amount. The normalization factor in such comparison is the Galactic supernova rate (see discussion in Chap. 11). ^{26}Al measurements interpreted within this framework yield a core-collapse supernova rate; values of $1.9 \pm 1.1\,\mathrm{SN\,century^{-1}}$ (Diehl et al. 2006a),

or, correspondingly reduced from foreground sources, 1.3 ± 0.4 SN century (Diehl 2016) have been estimated.

The line width of the ^{26}Al line as seen from the Galaxy reflects Doppler broadening from the large-scale rotation within the Galaxy, but also from turbulent ^{26}Al nuclei motions in the presumably-hot interstellar gas phase that ^{26}Al may still reside in at the time of its decay, after its ejection from the source now typically traveling through interstellar space for $\simeq$1 My. A balloon experiment based report of a rather broad ^{26}Al line with 5.4 keV broadening beyond instrumental resolution of the Ge detector (Naya et al. 1996), the My-averaged velocity broadening correspondingly would be about 500 km s^{-1}. Over such long time scale, either ^{26}Al would have to reside in highly-turbulent regions of the ISM, or cavities surrounding Al sources would be kpc-sized, or ^{26}Al would have to condense on grains early-on so that its coasting through lower-velocity ISM at original ejecta velocities would be possible (Chen et al. 1997). As shown above, the kinematic signature from large-scale Galactic rotation has been detected with sufficient exposure (see discussion in Diehl 2013, for how sufficient detail had been accumulated over the years of the INTEGRAL mission to enable such a measurement). An astrophysical broadening of the all-sky integrated ^{26}Al line was discovered also with INTEGRAL. The broadening value of 1.4 keV ($\pm$0.3 keV) is much smaller than what had been reported from the above balloon instrument data, and corresponds to 175 km s^{-1} ($\pm$45 km s^{-1}) in velocity space.

The bulk velocities seen in the Doppler shifts of the ^{26}Al line as viewed towards different Galactic longitudes (Fig. 7.5) turn out to be on the order of several 100 km s^{-1}. If interpreted as large scale Galactic rotation on Keplerian orbits around

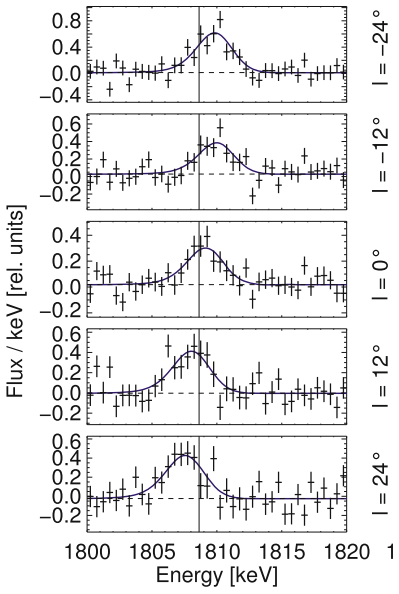

Fig. 7.5 ^{26}Al line variation with Galactic longitude (Diehl et al. 2006a). This shift of the line centroid reflects the kinematics of ^{26}Al towards the inner Galaxy in INTEGRAL/SPI measurements (Kretschmer et al. 2013)

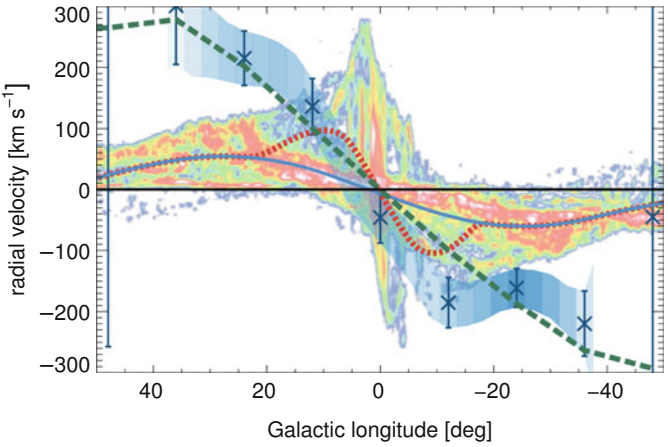

Fig. 7.6 Kinematics of ^{26}Al towards the inner Galaxy, from INTEGRAL/SPI measurements. This longitude-velocity diagram for hot ISM as traced through ^{26}Al in the inner Galaxy shows the trend from the Galaxy's large-scale rotation. The underlying color plots show the corresponding kinematics from molecular gas as traced through CO data. The ^{26}Al traced hot gas shows systematically higher velocities by about 200 km s^{-1} in the direction of Galactic rotation (Kretschmer et al. 2013)

the central regions of the Galaxy, this should be consistent for different objects within the Galaxy. Figure 7.6 compares the velocities determined from ^{26}Al and thus representing hot interstellar medium around sources of nucleosynthesis, with measurements of bulk velocities of molecular clouds as traced by carbon monoxide (Dame et al. 2001). Evidently, the velocities measured from ^{26}Al kinematics exceed typical Galactic rotation significantly, by about 200 km s^{-1}. Something must be different for hot gas near nucleosynthesis sources; but such generally more rapid rotation is not possible, and radioactive decay probably is part of the explanation.

When we consider that ^{26}Al will stream into the medium surrounding its sources while decaying, it is clear that the velocity measurement from ^{26}Al will be biased towards the conditions in the vicinity of the source, and ^{26}Al at locations more distant from the source will have decayed to ^{26}Mg and not emit gamma rays. Ejection from the sources plausibly should be isotropic. Typical ejection velocities are on the order of a few 1000 km s^{-1}, both for corec-collapse supernovae and for Wolf-Rayet stellar winds. But streaming away from its sources, if there would be an asymmetry of circum-source medium density such that in the direction of Galactic rotation more ^{26}Al would be streaming freely than in directions opposing Galactic rotation, the measurements could be understood. Based on such ideas, an asymmetry scenarion was proposed: Massive stars inside the Galaxy's co-rotation radius would be formed within spiral arms, but travel towards the leading edges of spiral arms while evolving into their Wolf Rayet phases, and in any case before they explode as supernovae. Then, the ejection of nucleosynthesis ejecta would occur in a region with a density gradient, higher density surroundings from the spiral arm

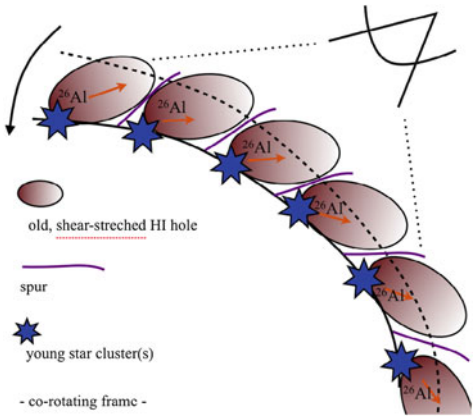

Fig. 7.7 Scenario for asymmetric surroundings of ^{26}Al sources. At time of nucleosynthesis product ejection, massive star groups could be located at the leading edges of spiral arms, thus presenting more material moving away from spiral arms at higher velocities than moving 'backwards' into higher density regions (Krause et al. 2015)

being located preferentially behind the massive stars, as seen from the perspective of an object at large-scale Keplerian rotation. So, ejecta would be decelerated if streaming towards the spiral arms, while streaming at higher velocities would be allowed into the inter-arm regions. Such a scenario (Krause et al. 2015), placing the candidate ^{26}Al sources along inner spiral arms and preferentially onto their inner ends approaching the Galaxy's bar, is illustrated in Fig. 7.7, and results in a longitude-velocity trend as shown by the green-dashed line in Fig. 7.6. In these calculations, the pitch angle of a logarithmic spiral structure model has been fitted (and obtains values in agreement with common results inferred otherwise), and an ejecta velocity of 200 km s^{-1} had been assumed, which corresponds to the typical expected sound velocity in superbubbles.

The significant enhancement of apparent velocities as observed from ^{26}Al therefore suggests that sources of ^{26}Al may be typically surrounded by interstellar cavities. These could have been created by previous stellar generations, or, alternatively, by the winds of the most-massive stars of a massive-star group, which evolve on shortest time scales and thus enter their Wolf-Rayet phase with strong winds only about 3 My after their formation. Superbubbles as typical surroundings of massive stars with ages of few to tens of My then presents a new scenario for how new nuclei may be recycled into the general flow of cosmic gas as part of cosmic chemical evolution. The sizes of such cavities plausibly extend up to kpc (Krause et al. 2015). Ejecta may thus be returned into ambient interstellar medium only as the walls of such superbubbles fragment and dissolve, on time scales beyond 10^7 years. ^{26}Al has shed new light onto the evolution of enriched gas on such time scales, which are difficult to constrain through observations otherwise.

Excess ^{26}Mg has been found in meteorites and associated with prior existence of ^{26}Al within these samples. Within meteoritic samples, one finds characteristic condensations, the CAI chondrules, which are associated with the first solids condensing in the early solar system which are preserved in their original composition.

These show a rather well-determined isotopic ratio ^{26}Al/^{27}Al of 4.5×10^{-5} (MacPherson et al. 1995, 2010), and are shown in the upper graph of Fig. 7.8 (see details in Chap. 6). Much smaller particles of stardust are also found as inclusions in meteorites, and these show a large spread of ^{26}Al/^{27}Al with generally higher values up to 1. Figure 7.8 (below) shows a more-recent representation of such stardust results. These are understood to originate from the immediate vicinity of sources of nucleosynthesis, where copious ^{26}Al production can lead to such high values, in particular for AGB stars (see Chap. 3). It is now interesting to see if, at the larger scale of the Galaxy which is sampled by the gamma ray measurements, the isotopic ratio for Al would be similar to values found for solar system material. Estimating the ^{27}Al amount from the Galaxy's gas mass estimates and solar abundance, and using the ^{26}Al mass derived from the gamma ray data as discussed above, one obtains a present-day ratio ^{26}Al/^{27}Al of $(6\pm3)\times10^{-6}$; the uncertainty of the current-ISM ratio was estimated from the gamma-ray flux uncertainty and uncertain ^{27}Al abundance. The result shown in Fig. 7.8 (top) is consistent with the conjecture (discussed in detail in Chap. 6) that the solar system is particularly enriched in ^{26}Al from some nearby nucleosynthesis.

7.2.4 ^{26}Al from Specific Regions

The deep exposures of regions along the Galactic plane provided by the long-duration missions of COMPTEL and INTEGRAL were sufficient to identify and discriminate emission from specific source regions within the Galaxy (Fig. 7.9). In the following, the most-prominent regions are discussed in more detail (see also Chap. 11 and Sect. 11.1.2.4).

7.2.4.1 ^{26}Al in the Cygnus Region

The ^{26}Al gamma-ray images show emission from the Cygnus region at Galactic longitude near 80° as the clearest and most-prominent feature beyond the bright ridge in the inner Galaxy (see Figs. 7.2 and 7.4). From 13 years of INTEGRAL observations, the ^{26}Al line is seen at 11σ significance and an intensity of $9.3 \pm 1.8)\times10^{-5}$ ph cm^{-2} s^{-1} (Fig. 7.10, from Siegert 2017).

Along the line of sight towards Cygnus, there are six prominent OB associations at distances ranging from 0.7 to 2.5 kpc (Plüschke et al. 2002), plus about a dozen open clusters, some associated to those OB associations (Fig. 7.11). Their ages range from 2.5 to 7.5 My.

It appears that the Cygnus OB2 association dominates by far the stellar census of this *Cygnus complex*; possibly, the associations Cyg OB1, 2, and 9 are related to OB2 and may originate from the same parental molecular cloud (Knödlseder et al. 2002). Cyg OB2 may even be considered the most prominent case in our Galaxy of

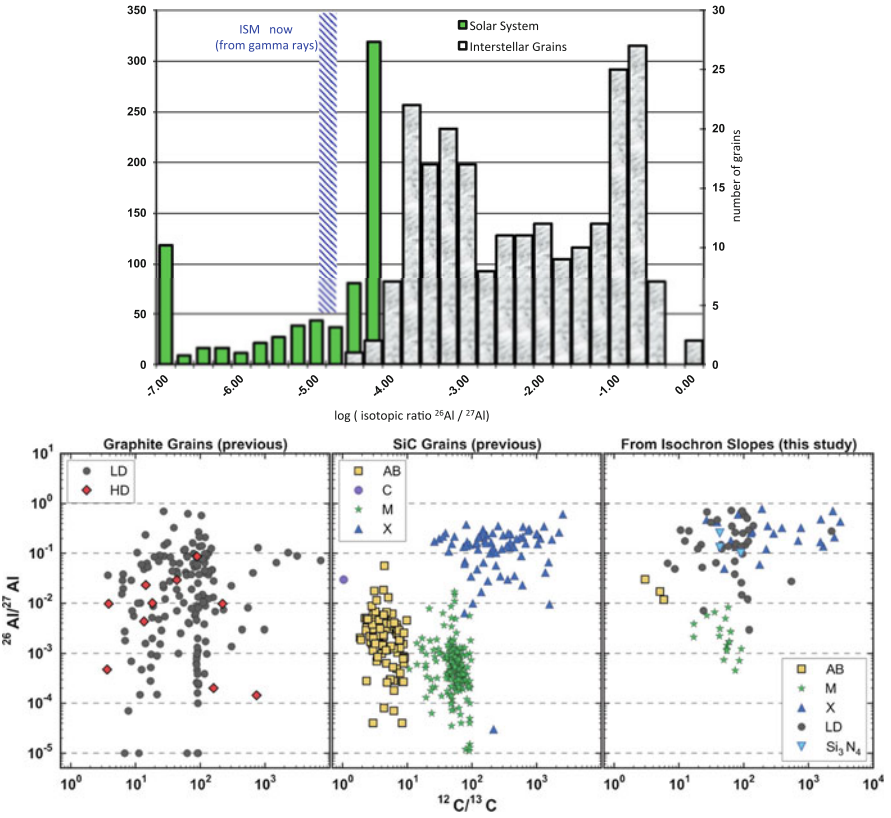

Fig. 7.8 *Top:* Isotopic ratios of radioactive versus stable Al, $^{26}Al/^{27}Al$, are determined rather accurately for meteoritic components. Stardust particles (grey) show high values, while solids associated with the early solar system condensations (green) yield a limiting value of 4.5×10^{-5}. The global galactic value inferred from the gamma-ray data (blue hatched) lies somewhat below this, consistent with the early solar system's special enrichment discussed in detail in Chap. 6. *Bottom:* Stardust sample isotopic signatures. In three-isotope graphs, the characteristics of the dust formation site are imprinted, and compositional patterns of ^{26}Al enrichments show that high ratios of $^{26}Al/^{27}Al$ up to 1 were characteristic in the formation sites of this stardust. This is orders of magnitude above the ratio of $^{26}Al/^{27}Al$ that is estimated for the Galaxy's interstellar gas as a whole, from the ^{26}Al gamma ray line observations. Grains of type AB are thought to originate from AGB stars, while grain types X and LD are attributed to a supernova origin (after Groopman et al. 2015)

extremely-rich superclusters, which appear prominent in other galaxies but are hard to recognize within our own Galaxy; about 120 stars in the high-mass range (20–120 $M_\odot$) have been identified to relate to Cyg OB2; the other associations typically are ten times smaller. The age and distance of Cyg OB2 is 2.5 My and 1.57 kpc, respectively.

Other prominent objects towards this line of sight include the Cygnus Loop supernova remnant, and a diffuse and extended structure of X-ray emitting (hot) gas

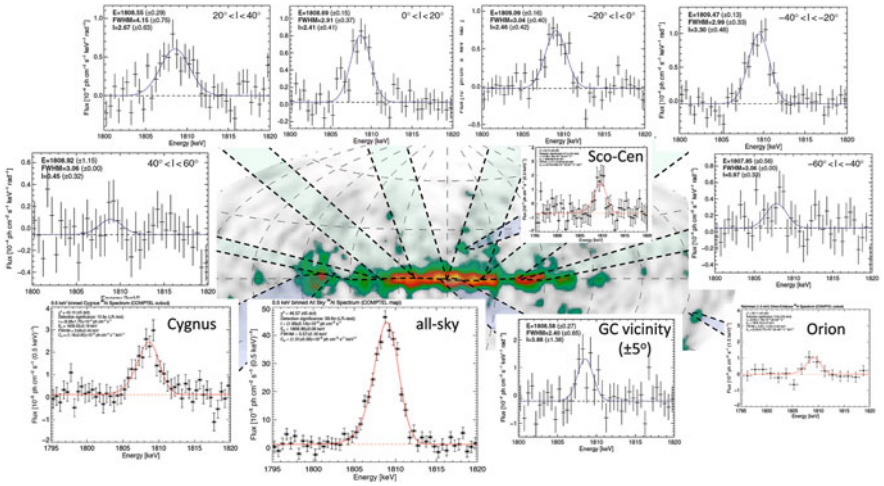

Fig. 7.9 The ^{26}Al line is measured separately for different emission regions along the plane of the Galaxy (from 5 years of INTEGRAL/SPI observations, Wang et al. 2009, and updates from internal reports MPE)

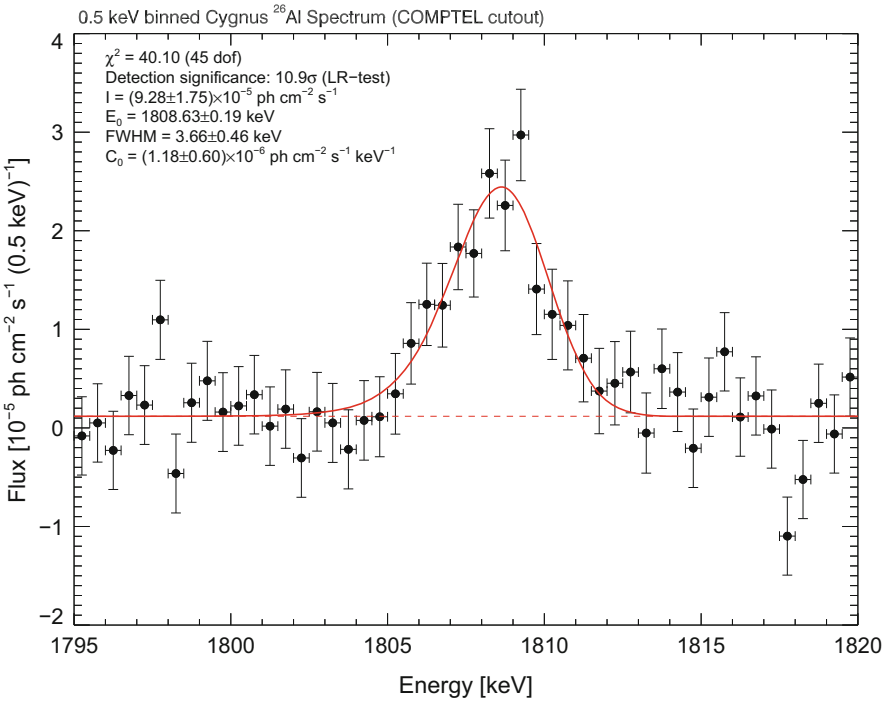

Fig. 7.10 Gamma-ray spectrum with the ^{26}Al line as measured with INTEGRAL/SPI towards Cygnus (see also Fig. 7.11; from Siegert 2017)

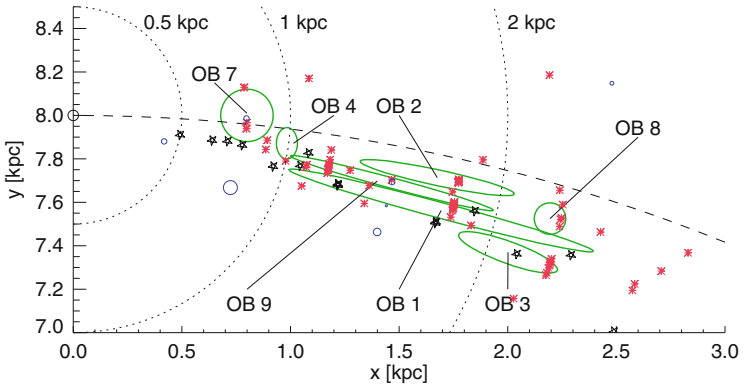

Fig. 7.11 Top view of the Galactic plane, showing the position of the Sun and prominent objects towards Cygnus. The OB associations along the line of sight towards the Cygnus region cover a rather large range of distances (ellipses illustrate distance uncertainties; Plüschke et al. 2002). The Cygnus OB2 group is by far the richest group of stars, and probably dominates ^{26}Al production

called the Cygnus Superbubble. The Cygnus Loop is a young supernova remnant with an estimated age of 10,000 years, and relatively nearby at 540 pc distance (Blair et al. 2005), attributed to a $\sim$12 $M_\odot$ progenitor star. By itself, it is a candidate ^{26}Al source, yet not more prominent than other massive stars if viewed at the characteristic ^{26}Al time scale of 1 My. Its proximity and age makes it appear as a bright X-ray and radio source; its ^{26}Al contribution appears unrelated to the Cygnus complex, however. The Cygnus Superbubble (Cash et al. 1980) is potentially more interesting for ^{26}Al studies, as it is much more extended and thus may be related to the collective effects of many past supernovae and/or massive-star winds. It has been re-assessed from radio observations as being most likely a superposition of many smaller hot-gas filaments at a range of distances (Uyanıker et al. 2001). The current picture is that within the Cygnus region, star formation has been ongoing for more than 10 My, and has led to a significant population of field and dispersed stars, in addition to the now-observed relatively-young OB associations. The large variations of visual magnitude extinction over small angular scales also supports a picture where the interstellar medium in the Cygnus complex is very heterogeneous and filamentary, with hot cavities bounded by dense remains of the parental molecular clouds (Lozinskaya et al. 2002; Comerón et al. 2008). Thus, one difficulty is to constrain the stellar population of a specific OB association (such as Cyg OB2) from all O stars seen towards this sightline, and to avoid inclusions of indirectly or even unrelated stars in such stellar budget (as discussed in detail by Comerón et al. 2008).

The total ^{26}Al gamma-ray brightness towards the Cygnus direction in the longitude interval [70°, 96°] has been associated to the specific sources in Cygnus with $\sim 6 \times 10^{-5}$ ph cm^{-2} s^{-1} (from the line of sight towards the Cygnus OB associations, accounting for a large-scale Galactic-disk background), and the contribution from

the *Cygnus complex* alone was estimated as $\sim 3.9 \times 10^{-5}$ ph cm^{-2} s^{-1} (Martin et al. 2009).

Because of this young age of the dominant source region of Cyg OB2, stellar evolution even for the most-massive stars should still not be completed, and contributions from core-collapse supernovae to ^{26}Al production should be small or absent. Wolf-Rayet-wind ejected ^{26}Al from hydrostatic nucleosynthesis may be assumed to dominate, currently originating from Cyg OB2 stars. In that case ^{26}Al gamma-rays from the Cygnus region potentially could disentangle the different ^{26}Al production phases and regions within the same massive stars: In galactic-averaged analysis, one assumes a *steady state* situation of ^{26}Al decay and production, such that the complete age range of stars is represented and contributes to ^{26}Al production with its time-averaged numbers of stars per age interval and their characteristic ^{26}Al ejection from either process (hydrostatic, or late-shell burning plus explosive; Limongi and Chieffi (see 2006b, and Chapter 4)).

From a first comparison of measured versus expected ^{26}Al emission, as estimated from the number of massive stars in the region, ^{26}Al emission seemed surprisingly bright. But a revision of the stellar census using IR data of the 2MASS survey brought population synthesis estimates into closer agreement with expectations (Knödlseder et al. 2002; Martin et al. 2009, 2010). One can use *population synthesis* to account for time dependent ^{26}Al ejections from a coeval group of massive stars. In such an approach, the stellar evolution model results for different initial masses of a star are evaluated and accumulated, for a group of stars with a specified total stellar mass and individual mass values and numbers drawn from an initial-mass distribution function (for details of the method see Voss et al. 2009). Martin et al. (2009) applied this to the stellar groups of the Cygnus complex. The resulting time dependent ejection of ^{26}Al is shown in Fig. 7.12, and compared to the observed ^{26}Al intensity. It appears that the measurement and prediction are in agreement, within uncertainties. Then, indeed, the observed ^{26}Al should be attributed to Wolf Rayet wind ejections, with contributions from core-collapse supernovae just beginning or expected in the near future. This seems consistent with the absence of signs of core collapse supernovae such as radio- or X-ray supernova remnants and pulsars (see discussion by Martin et al. 2010). Martin et al. (2010) point out, however, that there is some uncertainty about the metallicity in the Cygnus region, which could be lower than solar by a factor of a few. Then, the Wolf Rayet winds would likely be weaker, shifting the time of most ^{26}Al ejection towards a peak driven by supernovae, and at a later time. The consistency shown in Fig. 7.12 is suggestive that this is not the case.

For a young and active region of massive-star action, one may plausibly assume that the interstellar medium would be peculiar and probably more dynamic than in a large-scale average. With the Fermi satellite, evidence for cosmic ray produced high-energy gamma ray emission has been found at GeV energies (Tibaldo and Grenier 2013), confirming such turbulent interstellar medium with likely production of the shock fronts that are plausible cosmic-ray accelerators. With the fine spectroscopic resolution of the INTEGRAL measurements, therefore constraints

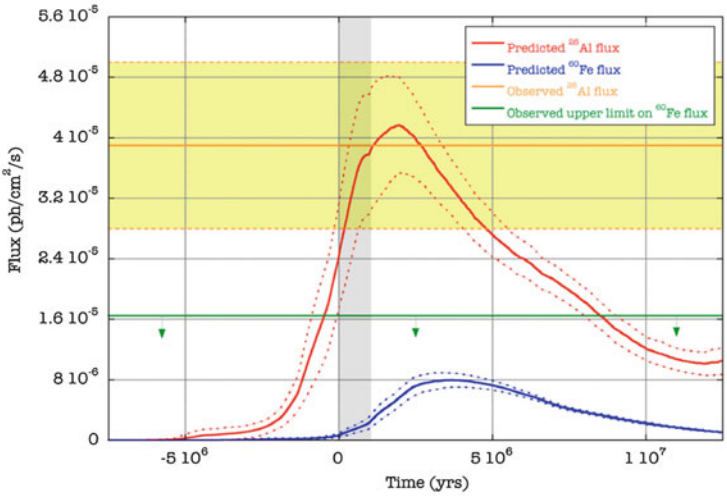

Fig. 7.12 The time history of ^{26}Al production in the Cygnus complex, as compared to the gamma-ray observations. Expectations from such populations synthesis are on the low side of observed ^{26}Al gamma-rays, in particular if a lower metallicity is adopted for the Cygnus region (solar metallicity is assumed, 0.04). The horizontal shaded area presents the range given by the ^{26}Al gamma-ray data, the dashed lines bracket the uncertainty range of predictions from recent massive-star models through population synthesis, and the vertical shaded area indicates the current time (from adopted cluster ages; the impact of stellar rotation on age estimates determines the width of the shaded area) (Figure adapted from Martin et al. 2010)

for a broadened ^{26}Al gamma-ray line would be interesting. As shown in Fig. 7.10, broadening is modest but present, at a level comparable to the Galactic-averaged value (see Fig. 7.3), i.e. at or below $\sim$200 km s^{-1}).

7.2.4.2 ^{26}Al in the Orion Region

The Orion region is the most-nearby region of massive stars, at a distance of $\sim$450 pc (Bally 2008; Genzel and Stutzki 1989). Its location towards the outer Galaxy and at Galactic latitudes around 20° is favorable, as potential confusion from other Galactic sources is negligible. The groups of massive stars, and in particular the Orion Nebula Cluster of stars, have been studied extensively, and are considered the prototype laboratory for astrophysical studies of *normal* massive-star activity. The dominating group of massive stars is the Orion OB1 association (Brown et al. 1994) with three major subgroups of different ages, one oldest subgroup *a* at 8–12 My, and two possibly coeval subgroups *b* (5–8 My) and *c* (2–6 My); subgroup *d* is the smallest and youngest at 1 My or below (see re-assessment of the stellar census by Voss et al. 2010). Subgroup c hold most massive stars, about 45 in the mass range 4–120 $M_\odot$. These groups are located on the near side of the Orion A and B molecular

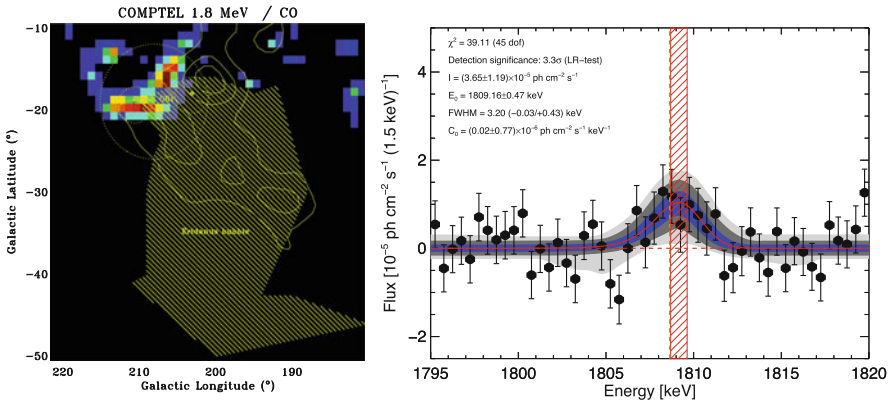

Fig. 7.13 The ^{26}Al gamma-ray signal seen by COMPTEL (left) and INTEGRAL/SPI (right) towards Orion. The gamma-ray intensity map contours from COMPTEL measurements are inconsistent with a concentrated source, and suggest extended emission away from the Orion molecular clouds (color pixels in the map, from CO) and the OB1 association subgroups (circles). The location of the interstellar cavity of Eridanus is indicated (hatched). From Diehl et al. (2003). The spectrum measured with SPI's Ge detectors shows a clear detection of the ^{26}Al line, at instrumental line width, with an indicated bulk motion blue shift (from Siegert and Diehl 2017)

clouds, which extend from 320 to 500 pc distance away from the Sun, and span a region of ∼120 pc perpendicular to our viewing direction.

With the COMPTEL imaging telescope, only faint hints for emission in the wider Orion region were noticed, at low surface brightness and apparently only at the level of typical noise (Fig. 7.13). Upon a closer inspection, a clear line at 1.8 MeV could be seen (which is typically not seen for other low-brightness regions in the COMPTEL map), and a model fit suggested a significant (5σ) detection of ^{26}Al from Orion (Diehl 2002)). INTEGRAL observations could confirm this signal, though marginally at 3σ, at an intensity of $(3.65 \pm 1.2) \times 10^{-5}$ ph cm^{-2} s^{-1} (Fig. 7.13, from Siegert 2017).

Earlier X-ray studies and HI maps had revealed that a huge interstellar cavity was extending from the Orion molecular clouds towards the Sun, banana-shaped and extending over almost 300 pc (Burrows et al. 1993) (see sketch in Fig. 7.14). The oldest, and most-nearby, OB1 subgroup *a* plausibly may have created the Eridanus cavity on the near side of the Orion molecular clouds, triggering subsequent star formation (the later and more-distant OB1 subgroups) into the molecular cloud. The scenario illustrated in Fig. 7.14 plausibly explains the offset of ^{26}Al gamma-rays from their sources, as well as the indicated blue shift: fresh ejecta propagate further into the cavity, and ^{26}Al decays along with its flow. Population synthesis for the OB1 subgroups and their expected ejections of kinetic energy and ^{26}Al support this scenario (Fig. 7.15): Energy for blowing the Eridanus cavity had been available, and ^{26}Al production appears ongoing almost steadily, from OB1 subgroups. Hydrodynamical simulations of such massive-star feedback resulted

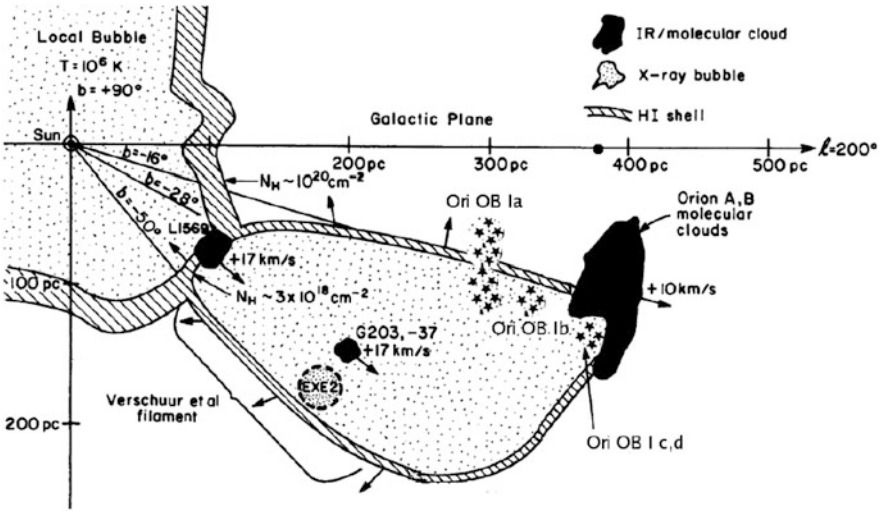

Fig. 7.14 A sketch of the region between us and the molecular clouds in Orion at about 450 pc distance, with the OB1 stellar association and its subgroups on the near side of the clouds, and the Eridanus cavity extending from the clouds towards the Sun. A scenario of ^{26}Al distribution from ejecta of the Orion OB1 association, blown into the Eridanus cavity, is indicated. Adapted from Burrows et al. (1993), see Fierlinger et al. (2016)

in predictions of gas morphology and X-ray emission from the Eridanus cavity, which are consistent with observational constraints from HI and diffuse X-ray emission measurements (Fierlinger et al. 2016; Krause et al. 2013, 2014). Thus, the Orion region appears to resemble one of the massive-star clusters in an asymmetric geometry that was suggested above (Fig. 7.7) to explain the velocity offset of ^{26}Al versus large-scale Galactic rotation (Fig. 7.15).

7.2.4.3 ^{26}Al in the Sco-Cen Region

The most-nearby groups of stars with members massive enough to significantly shape their surrounding medium is the stellar association of Scorpius-Centaurus and its subgroups, at a distance of about 100–150 pc (de Geus 1992; de Zeeuw et al. 1999; Preibisch and Zinnecker 1999).

Its location in the sky is up to 20° above the plane of the Galaxy, quite extended though, due to its proximity; the member stars are recognised through their coherent motion, as shown in Fig. 7.16 in the righthand graph.

The COMPTEL ^{26}Al image shows some hints for emission that may be associated to Sco-Cen, only recognisable due to its location above the Galactic plane. INTEGRAL observations obtained a very deep exposure of the region of the inner Galaxy, so that ^{26}Al emission from Sco-Cen could be detected from an emission region of about 50 degrees^2 centered at $(l, b) = 350°, 20°$) (Diehl et al. 2010). The

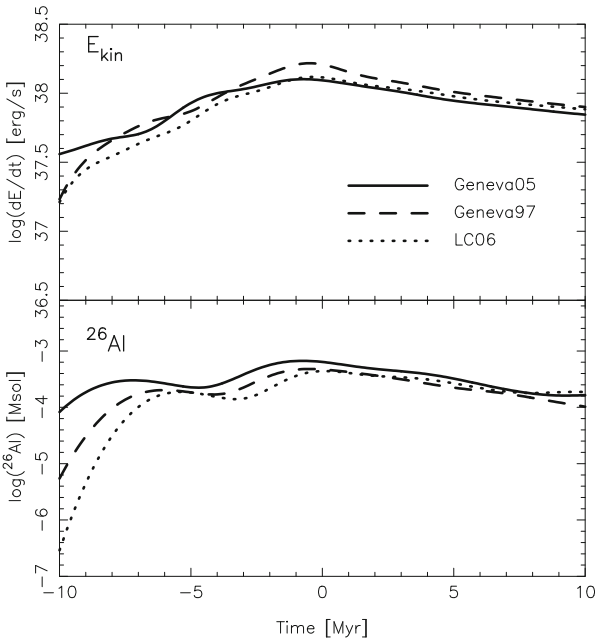

Fig. 7.15 The predicted time dependence of ejections of kinetic energy (above) and ^{26}Al (below), from population synthesis of the Orion OB1 association and its subgroups (Voss et al. 2010)

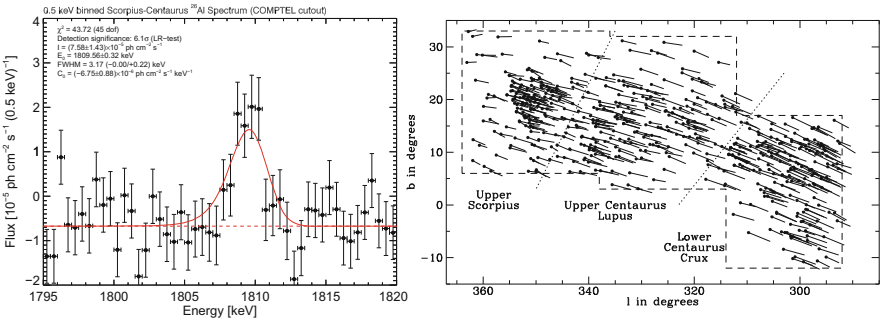

Fig. 7.16 The ^{26}Al signal disentangled from the Scorpius-Centaurus region with INTEGRAL (left; Diehl et al. 2010; Siegert 2017), and an illustration of the stars as tracked by Hipparcos in this nearby region (right, de Zeeuw et al. 1999)

spectrum from a similar region from 13 years of data is shown in Fig. 7.16 (left) (from Siegert 2017). The intensity in the ^{26}Al line of $(7.6 \pm 1.4) \times 10^{-5}$ ph cm^{-2} s^{-1} can plausibly be associated to massive star outputs from the Upper Sco subgroup (Diehl et al. 2010); the population synthesis estimate predicts 7×10^{-5} ph cm^{-2} s^{-1} from the stellar census, which should be rather complete for this nearby association.

Signs of past supernova activity from these stars are imprinted on the morphology of the nearby interstellar medium, which could be mapped in quite some detail from

absorption line measurements towards nearby stars (Frisch 1995; Lallement 2007). Estimates are that the most massive star in Upper Sco presumably had $\sim 50\,M_{\odot}$ and thus may have exploded as a supernova about 1.5 Myr ago, and the pulsar PSR J1932+1059 may be its compact remnant (Hoogerwerf et al. 2000; Chatterjee et al. 2004). Several loops/shells reminiscent of supernova remnants have been identified (de Geus 1992). The Local Bubble is the most-nearby of such a cavity, surrounding the Sun (Breitschwerdt et al. 1998), as seen in X-ray emission from hot gas in its interior. Its origin has been related to subgroups associated with the Sco-Cen association (Breitschwerdt and de Avillez 2006; Fuchs et al. 2009; Welsh and Shelton 2009). Also, the supernova origin of live radioactivity of ^{60}Fe that was found in oceanfloor and lunar material (Wallner et al. 2016) is attributed to an origin related to Sco-Cen (Breitschwerdt et al. 2016) (see details in Chaps. 4 and 6).

At least three subgroups of different ages can be distinguished among the Sco-Cen stars (de Geus et al. 1989; de Zeeuw et al. 1999): The Upper Centaurus-Lupus (UCL), Lower Centaurus Crux (LCC), and Upper Centaurus (USco) groups, as shown in Fig. 7.16 in the righthand graph. Their ages are 17, 15, and 5 My, respectively, where typical age uncertainties are 1–2 My (de Geus et al. 1989; Slesnick et al. 2008; Pecaut and Mamajek 2016). Stellar subgroups of different ages would result from a star forming region within a giant molecular cloud if the environmental effects of massive-star action of a first generation of stars (specifically shocks from winds and supernovae) would interact with nearby dense interstellar medium, in a scenario of *propagating* or *triggered star formation*. Then later-generation ejecta would find the ISM pre-shaped by previous stellar generations. Such a scenario was proposed (de Geus et al. 1989; Preibisch and Zinnecker 1999) based on the different subgroups of the Scorpius-Centaurus association and the stellar groups surrounding it (e.g. Preibisch and Mamajek 2008; Fernández et al. 2008). It is illustrated in Fig. 7.17 (upper set of graphs).

Indications of recent star formation have been found in the L1688 cloud as part of the ρ Oph molecular cloud, and may have been triggered by the winds and supernovae causing the ^{26}Al we observe. The young ρ Oph stars then could be interpreted as the latest signs of propagating star formation originally initiated from the oldest Sco-Cen subgroup in Upper Centaurus Lupus (Wilking et al. 2008). Also the Lupus cloud shows recent star forming activity (Gaczkowski et al. 2015, 2017).

However, there is tension for a triggering scenario as originally proposed by Preibisch and Zinnecker (1999). Krause et al. (2018) combine data from the entire Sco-Cen region and wavelengths from radio to X- and gamma-rays, and rather propose that a concerted fireworks of star forming activity in different regions of an original, parental giant molecular cloud would be a more plausible description. They argue that the triggering of secondary star formation is more complex, and often arises from converging shells of expanding bubbles and superbubbles. They term this process "surround and squash" (see Fig. 7.17 lower graph) to illustrate how feedback from massive stars destroys the parental cloud little by little.

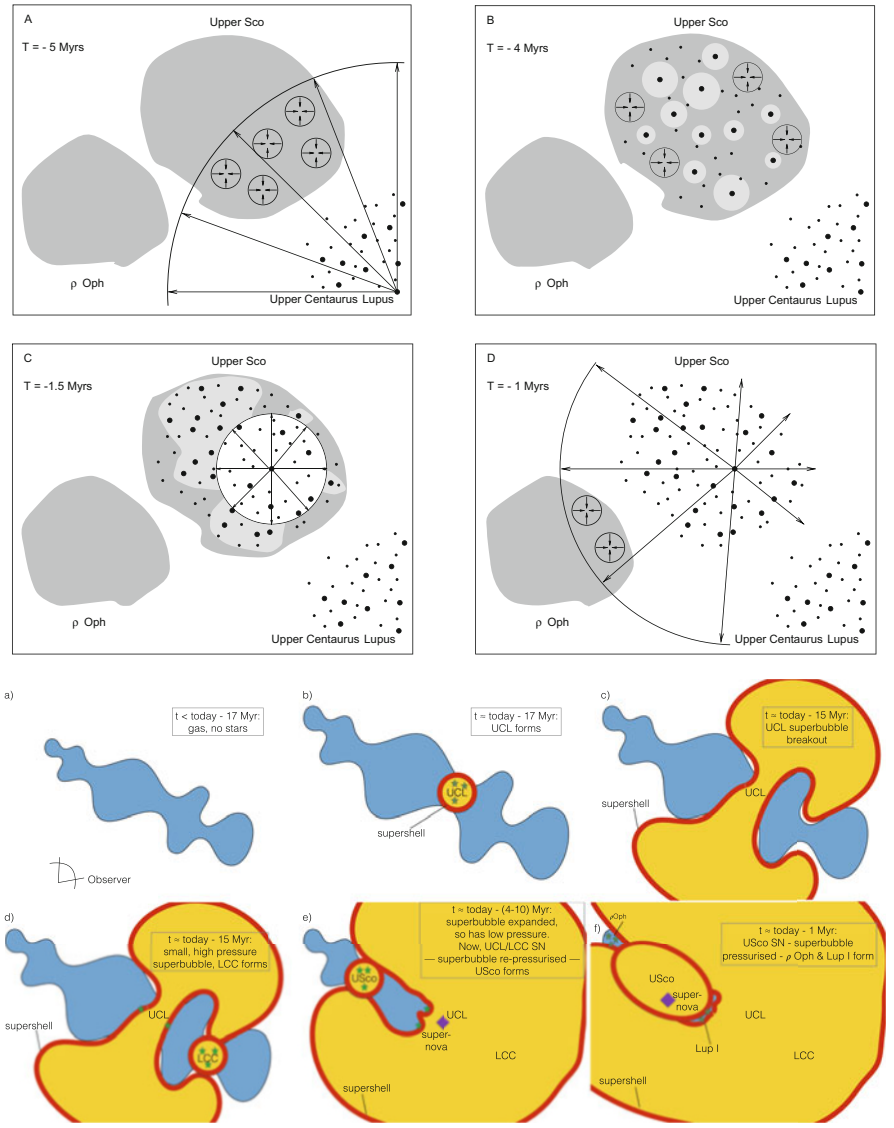

Fig. 7.17 *Top:* The objects in the Sco-Cen region, as they could have evolved in a scenario of *triggered star formation* (from Preibisch and Zinnecker 1999). *Bottom:* A scenario of successive erosion of molecular clouds by *propagating star formation* (from Krause et al. 2018)

7.3 ^{60}Fe

7.3.1 *Nuclear Reactions, Candidate Sources, and Observability*

^{60}Fe is a prominent neutron-rich isotope that can be produced from the abundant stable Fe isotopes if irradiated with neutrons (Fig. 7.18). The characteristic reaction sequence shown in Fig. 7.18 suggest that ^{60}Fe is produced by an s process of slow neutron capture reaction flow, allowing for (some!) intermediate β decay. The reaction path thus remains close to the valley of stable isotopes, as is characteristic for the s process. Note that the reaction domain of the r process (see Chap. 4) is far from the regimes of instability where neutrons cannot be bound easily. With Fe as seed elements being abundant, ^{60}Fe appears to be an excellent astrophysical probe of cosmic s-process environments.

Nuclear reaction uncertainties in ^{60}Fe production, therefore, are the neutron capture cross sections of ^{59}Fe and ^{60}Fe, for the production and destruction of ^{60}Fe, and their β decay rates, reducing ^{60}Fe yields. It is difficult to set up proper experiments for neutron capture, as its lifetime against β decay is 64 days only. Moreover, the resonant neutron capture, which probably dominates at stellar energies, also has a contribution from direct capture. Therefore, different measurements for different aspects and reaction channels involved have to be combined with theoretical estimates for reactions that may occur through excited stages of the nucleus (see Chap. 9).

The β decay itself had been theoretically estimated by FFN, later revised substantially by proper account of the Gamov-Teller transitions... Recently, Li et al. (2016) again revised the rate for ^{59}Fe, to now fall a factor 5 above Langanke+'s values, yet orders of magnitude below FFN's values; this shows that considerable uncertainty remains for the weak reactions involved in ^{60}Fe production.

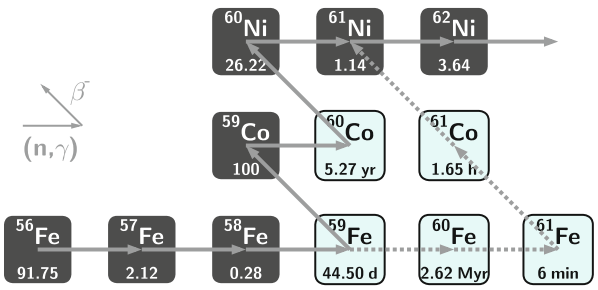

Fig. 7.18 The ^{60}Fe production through successive neutron capture reactions, with competing β decays indicated (from Heftrich et al. 2015)

The astrophysical setting of ^{60}Fe production is the existence of a neutron source in an environment where heavy elements such as Fe still may exist. These appear to be the shell burning stages of massive stars. Chapters 3 and 4 discuss these regions inside stars more thoroughly. Similar to ^{26}Al, ^{60}Fe also is a rather long-lived isotope, with a radioactive lifetime of 3.8×10^6 years (Rugel et al. (2009); corresponding half-life is 2.62 My). And, again, this lifetime is also short compared to a normal star's evolution, and on the order of the lifetime of the more-massive stars only. Hence, again, the ejection from the production site into interstellar space appears to be an issue. More-massive stars which undergo a supernova explosion soon after shell burning has been activated appear as most plausible sources.

Candidate production environments of ^{60}Fe are the zones of helium burning inside the more-massive stars. Here, the ^{22}Ne(α,n)^{25}Mg reaction liberates neutrons as helium undergoes this reaction with pre-existing neon that is convectively mixed into the reaction zone (Limongi and Chieffi 2006a,b). Later shell burning stages of more-massive stars may also produce some ^{60}Fe, as α particle release reactions again produce helium for this neutron-producing reaction. But, at those higher temperatures, ^{60}Fe production is less efficient, as it now must compete with increased rates of the β decays of ^{59}Fe and ^{60}Fe, as well as with photo-destruction reactions that begin to destroy heavier nuclei such as neon. Hence, the production of ^{60}Fe is a delicate process, requiring several conditions to be favourable. Conversely, if produced, the abundance of ^{60}Fe may reveal details about the conditions in the reaction site, that cannot be measured otherwise.

Contrary to the case of ^{26}Al, ^{60}Fe is expected to be ejected *only* by the SN explosion and not by the stellar wind, since it is buried to deep (up to the Ne-O shell) for ejection into interstellar space during any pre-supernova wind phase. It had been suggested, therefore, that detection of ^{60}Fe in the Galaxy would help to decide whether WR stars or core-collapse SN are the major sources of observed ^{26}Al. Stated more precisely, any massive-star region which is not in a steady state of production versus decay of these radioactivities from continued star formation, would show a variation of the γ-ray flux ratio from ^{26}Al and ^{60}Fe with age (see Voss et al. 2009, for model predictions) (see following section).

Also in rare thermonuclear explosions, ^{60}Fe could be produced (Woosley and Weaver 1994). If ignition occurs at highest densities, nuclear burning is expected to produce several neutron rich species, among them ^{60}Fe, which could be produced in substantial amounts. The necessary high central ignition densities will probably rarely be obtained, if the accretion is not exceptionally slow so that the white dwarf can remain cold up to reaching the Chandrasekhar mass limit. Accretion induced collapse, however, is a competing pathway for the evolution in such binary systems.

Upon its radioactive decay, ^{60}Fe emits gamma-rays from β^- decay. Through this radiation signature, it is suitable for remote studies of cosmic nucleosynthesis. Gamma-ray energies are 1173 and 1332 keV from cascade transitions in the final ^{60}Ni daughter nucleus of the β-decay in 99.85 and 99.98% of decays, respectively.

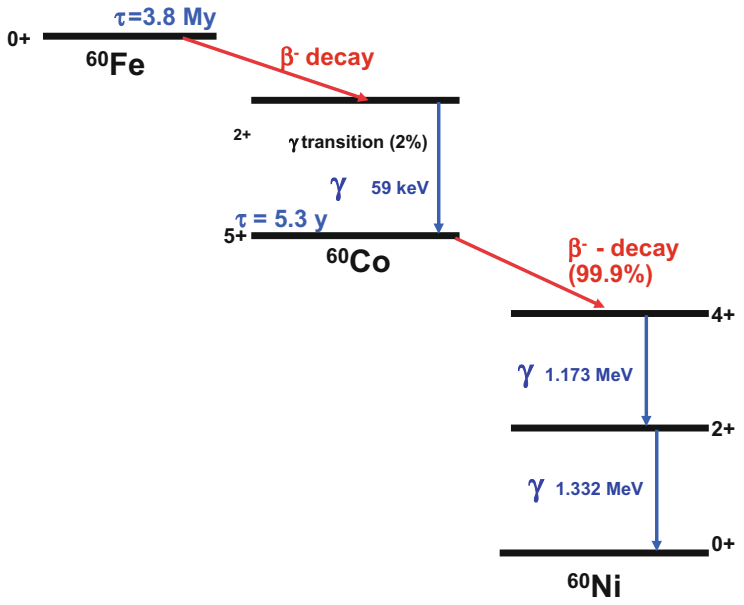

Fig. 7.19 The ^{60}Fe isotope decays with a radioactive lifetime of 3.8 My through ^{60}Co to ^{60}Ni. Note that per decay, two gamma-ray photons are obtained

A photon at 59 keV energy accompanies this ^{60}Fe–^{60}Co–^{60}Ni-decay chain, from a transition in the primary daughter nucleus ^{60}Co, is seen in 2% of ^{60}Fe-decays only (most de-excitations occur through internal conversion), and thus relatively unimportant. The decay chain of ^{60}Fe (see Fig. 7.19) involves intermediate ^{60}Co and produces two gamma-rays at 1332 and 1173 keV, respectively, which are well-known from laboratory work through the ^{60}Co calibration sources.

7.3.2 Observations Throughout the Galaxy

^{60}Fe gamma-rays are hard to detect with current telescope sensitivities. RHESSI reported a marginal signal (2.6 σ for the combined ^{60}Fe lines at 1.173 and 1.332 MeV) (Smith 2004) from the inner Galaxy, at the 10%-level of ^{26}Al brightness; SPI aboard INTEGRAL obtains a similarly low value, around 10%, also at the 3σ-level from early analysis (Harris et al. 2005), but more convincingly the ^{60}Fe lines were seen at 5σ significance with 4 years of data (Wang et al. 2007)[2] (see Fig. 7.20), and reported a ^{60}Fe to ^{26}Al brightness ratio of 14 (±6)%. Efforts

[2]Instrumental background from ^{60}Co produced locally in the satellite by cosmic rays may be a remaining concern.Wang et al. (2007) have accounted for such contribution within instrumental

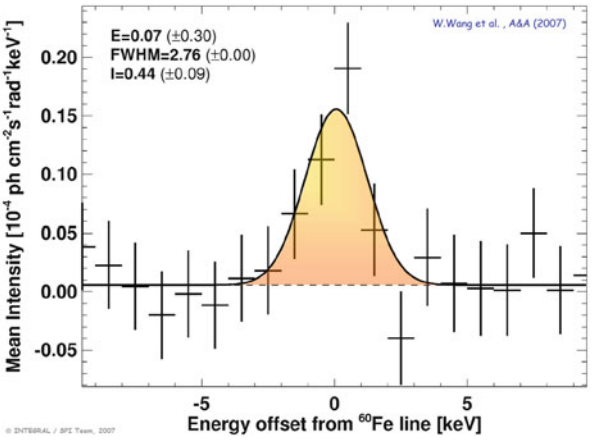

Fig. 7.20 The ^{60}Fe signal (both gamma-ray lines superimposed at their laboratory energies of 1173 and 1332 keV) as observed with INTEGRAL/SPI from the Galaxy (Wang et al. 2007)

are made to improve upon this measurement with deeper exposure collected with INTEGRAL. However, it has been shown that ^{60}Fe detectability suffers from a specific problem: The isotope ^{60}Co apparently is built up within the INTEGRAL spacecraft, background thus growing linearly with time (Diehl et al. 2018). The important test if indeed the spatial distribution of ^{60}Fe emission is identical to that of ^{26}Al thus remains a challenge. Nevertheless, obviously ^{60}Fe γ-ray intensity from the inner Galaxy remains substantially below the brightness from ^{26}Al.

Massive stars are the most plausible sources of both ^{60}Fe and ^{26}Al, but their production occurs at quite different regions and burning episodes in those same stars. The determination of the ratio of their yields $r = Y_{60Fe}/Y_{26Al}$ should be a very sensitive global diagnostic of the validity of massive-star nucleosynthesis models (e.g. Woosley and Heger 2007, and references therein). In steady-state approximation of current galactic nucleosynthesis (i.e. the galactic average synthesis rate of ^{26}Al and ^{60}Fe equals its decay rate), this production ratio and the total gamma-ray flux ratio accessible to gamma-ray telescopes are related through

$$\frac{I(^{60}Fe)}{I(^{26}Al)} = \frac{\dot{M}(^{60}Fe)}{\dot{M}(^{26}Al)} \cdot \frac{26}{60} \cdot 2 \tag{7.1}$$

where $\dot{M}(^{60}Fe)$ is the total Galactic production in $M_\odot$ year^{-1} (similarly for ^{26}Al). The mass of each isotope maintained in steady state throughout the Galaxy then is

$$\langle M(^{60}Fe)\rangle = \dot{M}(^{60}Fe) \cdot \tau(^{60}Fe) \tag{7.2}$$

knowledge. Note that insufficient subtraction of instrumental contributions would make the Galactic ^{60}Fe contribution even smaller.

For determination of the integrated production rate, the yield in ^{60}Fe per star of initial mass M is weighted with the number of stars of mass M, the *initial mass function*, summing over the mass range for massive stars $[M_{low}, M_{up}]$. Normalisation with the star formation rate cancels when the ratio for the ^{60}Fe and ^{26}Al isotopes is determined. This illustrates that much uncertainty related to unknowns of Galactic nucleosynthesis cancel for the isotope ratio ^{60}Fe/^{26}Al, and a measurement of the production ratio for all massive stars is obtained, which only depends on nucleosynthetic yields per star of mass M and the integration over the mass distribution of stars.[3]

Current models predict a gamma-ray flux ratio around 16% (Timmes et al. 1995; Woosley and Heger 2007) or ∼18 (±4)% (Limongi and Chieffi 2006b).[4]

Though apparently observations and predictions agree, there are uncertainties in both (gamma-ray telescope data analysis; nuclear-physics issues; massive-star shell burning). In several simulations, the nucleosynthesis imprint for the ^{60}Fe/^{26}Al ratio has been studied on a larger scale beyond individual sources. If the evolution of an entire star forming region is traced over its evolutionary time scale of order 10^7 years, apparently the ratio observed from gamma rays for the current milky way galaxy is compatible with expectations, for a more-evolved situation where also supernovae from the less-massive of the massive-star population contribute with enhanced ^{26}Al contributions—the earlier evolution with most-massive stars dominating produces ratios up to factors 2–3 higher (Kuffmeier et al. 2016, and references therein). But also, large fluctuations on a local scale of order of a star forming region occur, as well as fluctuations in time. Both are of order of a factor 10. This is relevant for the early solar system, discussed in Chap. 6, and for observations of specific regions: A determination of the ^{60}Fe to ^{26}Al ratio not only for integrated observations of the Galaxy, but more locally for specific regions of massive star nucleosynthesis would be revealing, with respect to the ^{60}Fe sources (see discussion above, Sect. 7.2.4.1).

7.3.3 *Observations of ^{60}Fe in Solar-System Material*

Live ^{60}Fe had been found more than 10 years ago in oceancrust material from the deep pacific ocean (Knie et al. 2004). This initiated a new ‘astronomy’ of radioactivity, the search for ejecta from nucleosynthesis sources near the solar system as captured directly. Radioactivity is the process that allows us to distinguish

[3]The mass range commonly assumed is 8–120 $M_\odot$; but both mass limits are subject to some uncertainty (see discussion in Zinnecker and Yorke 2007). Limongi and Chieffi (2006b) discuss in detail the impact of varying the slope of the mass distribution function, and the upper mass limit for the integrated range of masses.

[4]A period of irritation occurred between 2002 and 2005, as nuclear cross sections and models were updated, and seemed to predict much higher ratios up to 1; see discussion in Woosley and Heger (2007) and Prantzos (2004).

such ejecta samples from the bulk matter of the solar system bodies themselves. ^{60}Fe is located in a domain of atomic nuclei, where the prospects of finding such ejecta tracers are maximised: On one hand, normal solar system matter is made radioactive through energetic interactions with cosmic rays, through spallation reactions (see also Sect. 7.4). Spallation reactions thus break up nuclei, and due to the local abundance maximum around iron group elements, all nuclei lighter than the iron group elements are potentially created from such cosmic ray interactions. As discussed in Sect. 7.4, specific and widely used examples are ^{10}Be and ^{53}Mn, but also ^{26}Al is produced in significant abundance by cosmic ray interactions, for example in the Earth atmosphere. The positive side of such production is that one can measure cosmic ray intensities as well as atmospheric and terrestrial (e.g. subsurface water reservoirs) using radioactive isotopes. But detecting cosmogenic ^{26}Al on Earth is a challenge, due to the high cosmic ray production. Not so for ^{60}Fe, because the abundance of candidate nuclei which could be fragmented by cosmic-ray interactions to produce ^{60}Fe are much smaller, and, additionally, the production of a neutron rich daughter isotope in such a spallation reaction is small. Therefore, ^{60}Fe is a good candidate for studies of terrestrial or lunar samples of nucleosynthesis ejecta, as confirmed by the oceancrust detection of Knie et al. (2004).

Following this exciting discovery, ^{60}Fe as a nucleus was re-investigated, and its radioactive lifetime was found significantly longer in such improved measurements (Rugel et al. 2009; Ostdiek et al. 2017). This was important, as the inference of a nucleosynthetic origin of the terrestrial ^{60}Fe sample implies to calculate the probability that ejecta from an explosion at some recent time can reach the oceanfloor before the radioactive decay wipes out its information.

One might be concerned that a single sample of oceancrust, through carefully selected to minimise anthropogenic contaminations, could be a single outlier. Analysis of a sediment (Fitoussi et al. 2008) had been less significant, which seemed puzzling. Note that the Accelerator Mass Spectrometry method is one of the most sensitive isotopic abundance detection methods, with a sensitivity exceeding 10^{-17} (Korschinek and Kutschera 2015; Kutschera 2013). More than 10 years later, a broad collection of oceancrust and sediment probes from three different regions, the Indian, Pacific, and Atlantic ocean, covering an age range from current to 11 My ago, had been analysed for ^{60}Fe (Wallner et al. 2016). These consistently showed ^{60}Fe signals in an age range 1.5–3.5 My ago, and a possible second marginal signal around 8 My ago. The sediment data here have a much better time resolution around 10,000 years. From the analysis of lunar surface material obtained from the Apollo mission, also a significant signal from ^{60}Fe could be obtained (Fimiani et al. 2016). Here, the turnover of surface material ('gardening') prevents an age determination of the material; but the mere detection of ^{60}Fe was an important, independent, confirmation. Microfossils may help to enhance iron content locally, and were exploited by Ludwig et al. (2016) for yet another independent ^{60}Fe detection on a terrestrial material probe.

The infall period of ^{60}Fe in the composite data from all samples clearly is resolved, that is, it appears to be extended and therefore not likely due to a single supernova ejecta wave crossing the solar system. It would have been tempting to

'date' a nearby supernova explosion in this way. But reality appears to be more complex. Interstellar transport of ejecta from supernova explosions is not easy to model, and ^{26}Al kinematic information from superbubbles as discussed above (see Fig. 7.7 and discussion thereof) may help to understand some of such transport on larger scales. But even on scales of the Local Bubble, the dynamical evolution of the nearby morphology of cavities and walls is complex. Breitschwerdt et al. (2016) showed through 3D hydrodynamical modeling of the nearby interstellar medium, that both, a supernova from a nearby stellar group occurring within the solar cavity, as well as the passing of the cavity wall of this Local Bubble across the solar system, could be explanations for the signal. The extent in time that is observed may originate from multiple supernova ejections, or from ejecta being reflected on the nearby cavity wall (see also Schulreich et al. 2017). This is illustrated in Fig. 7.21, where data are shown as compared to each of these scenarios.

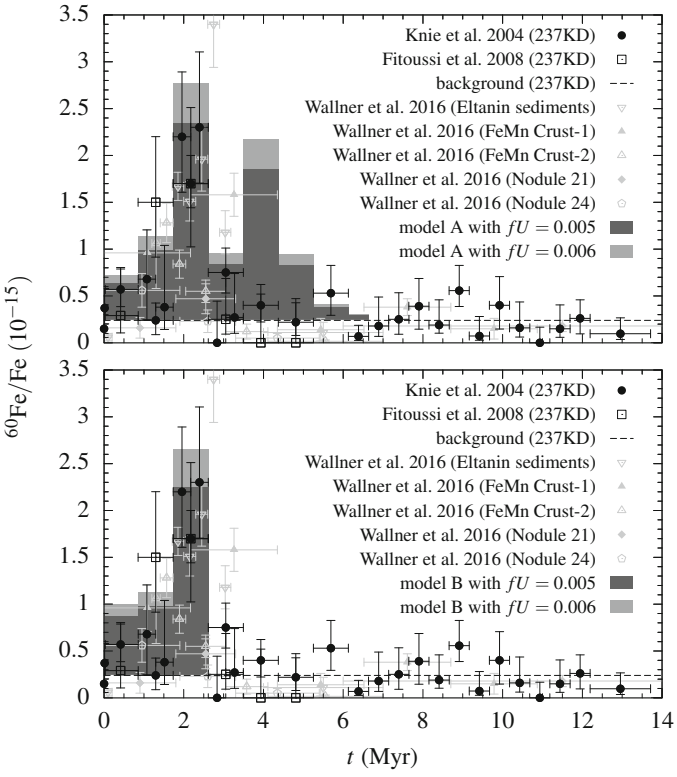

Fig. 7.21 The ^{60}Fe signal from several oceancrust and sediment analyses, as dated in time from age dating of the corresponding layer with cosmic-ray produced radioactive clocks ^{10}Be, ^{26}Al. The cases of ejections from supernovae and transport within the Local Bubble *(above)*, and from passing of the cavity wall across the solar system *(below)* are shown (from Schulreich et al. 2017)

7.4 Radioactivities in Cosmic Rays

Along with stellar grains, Galactic Cosmic Rays (GCR) provide a sample of matter from outside the Solar system. Despite almost a century of active research, the physics of GCR (concerning their sources, acceleration and propagation in the Galaxy) is not yet thoroughly understood. In particular, key questions regarding GCR physics are related to the timescales of various processes (acceleration in one event or in a series of events, confinement in the Galaxy, etc.). Radionuclides unstable to $\beta^{\pm}$ decay or e-capture, with laboratory lifetimes close to the timescales of interest for GCR studies, provide important probes of the aforementioned processes.

7.4.1 Sources, Acceleration, and Propagation of Cosmic Rays

From the previous section one may infer that several steps are involved between the production of the GCR nuclides in stellar interiors and their detection near Earth: (1) stellar nucleosynthesis, (2) ejection by stellar winds and explosions, (3) elemental fractionation, (4) acceleration of primary GCR nuclides, by shocks due to SN and winds of massive stars, (5) propagation through the ISM of the Galaxy, (6) modulation at the heliospheric boundary and (7) detection of arriving GCR. In particular, GCR transport through the ISM has been studied with models of varying sophistication, which account for a large number of astrophysical observables (see the comprehensive review of Strong et al. (2007) and references therein).

To describe the composition data, less sophisticated models are sufficient, like e.g. the *leaky-box* model. In that model, GCR are assumed to fill homogeneously a cylindrical box (the Galactic disk) and their intensity in the ISM is assumed to be in a steady state (equilibrium), between several production and destruction processes. The former involve acceleration in GCR sources and production *in-flight* through fragmentation of heavier nuclides, while the latter include either physical losses from the *leaky box* (*escape* from the Galaxy) or losses in energy space: *fragmentation*, *ionization losses* and *radioactive decay*. Most of the physical parameters describing these processes are well known, although some spallation cross sections still suffer from considerable uncertainties. The many intricacies of GCR transport are encoded in a simple parameter, the *escape length* Λ_{esc} (in $\mathrm{g\,cm^{-2}}$): it represents the average column density traversed by GCR nuclei before escaping the Galactic leaky box.

The abundance ratio of a secondary to a primary nuclide depends essentially on Λ_{esc}. Observations of $\frac{LiBeB}{CNO}$ (and more recently of $\frac{ScTiV}{Fe}$) in arriving GCR, interpreted in this framework, suggest a mean escape length $\Lambda_{esc} \sim 7\,\mathrm{g\,cm^{-2}}$. In fact, the observed GCR secondary/primary ratios display some energy dependence, which translates into an energy dependent $\Lambda_{esc}(E)$, going through a maximum at $E \sim 1$ GeV/nucleon and decreasing both at higher and lower energies. The observed

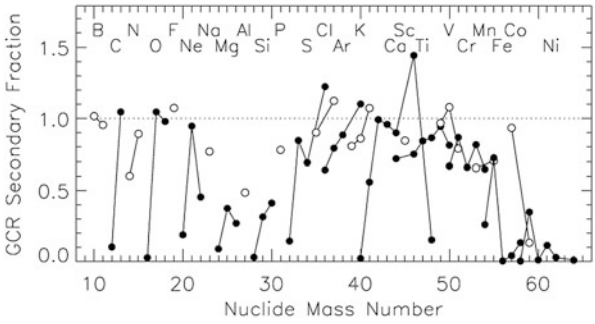

Fig. 7.22 Secondary fractions in arriving GCR for isotopes from B to Ni, after the analysis of ACE/CRIS measurements. Nuclides with filled (open) symbols correspond to isotopes with even (odd) Z, while solid lines connect isotopes of the same element. *From* Wiedenbeck et al. (2007)

energy dependence of that key phenomenological parameter can be interpreted in the framework of more sophisticated GCR transport models and provides valuable insight into the physics of GCR transport (role of turbulent diffusion, convection by a Galactic wind, re-acceleration, etc.); those same models can be used to infer the injection spectra of GCR at the source (see Jones et al. 2001; Strong et al. 2007).

Once the key parameters of the leaky-box model are adjusted to reproduce the key secondary/primary ratios, the same formalism may be used in order to evaluate the secondary fractions (produced by fragmentation in-flight) of all GCR nuclides. Those fractions depend critically on the relevant spallation cross-sections (well known in most cases) and appear in Fig. 7.22. Fractions close to 1 imply an almost purely secondary nature while fractions close to 0 characterize primary nuclides (like, e.g. ^{12}C, ^{16}O, ^{24}Mg, ^{56}Fe etc.). The former are very sensitive to the adopted Λ_{esc}, contrary to the latter (Wiedenbeck et al. 2007).

The *source abundances of primary GCR* (GCRS) derived that way display both similarities and differences when compared to the solar ones (Fig. 7.23). It was recognised quite early on, that the observed pattern of GCRS/Solar abundances shows some correlation with the First Ionisation Potential (FIP): elements of high FIP are depleted in GCRS relatively to low FIP ones. Since the latter are more easily ionized than the former, it is conceivable that they are also more easy to pre-accelerate (in some suitable environment) before SN shocks decerebrate them to relativistic GCR energies (Meyer 1985).Although similar FIP-dependent abundance patterns are observed in the solar corona, this idea did not evolve in a fully self-consistent model for the origin of GCR (Fig. 7.23).

Another, long standing, idea attracted considerable attention in the past 15 years. It invokes chemical volatility to explain fractionation in the GCR sources. Of course, volatility is somewhat related to FIP: high FIP elements (e.g. He, N, Ne, Ar) are, in general, volatile, where low FIP elements are, in general, refractories (e.g. Mg, Si, Fe etc.), and condense readily into dust grains. Meyer et al. (1997) and Ellison et al. (1997) suggested that grains are efficiently accelerated in SN shocks, because of their high mass/charge ratio; subsequent sputtering of atoms from these fast grains creates a *pool* of *suprathermal* ions, that are further accelerated to relativistic GCR energies from SN shocks. Building on those ideas, Meyer et al. (1997) proposed a model explaining quantitatively the inferred pattern of GCRS/Solar abundances.

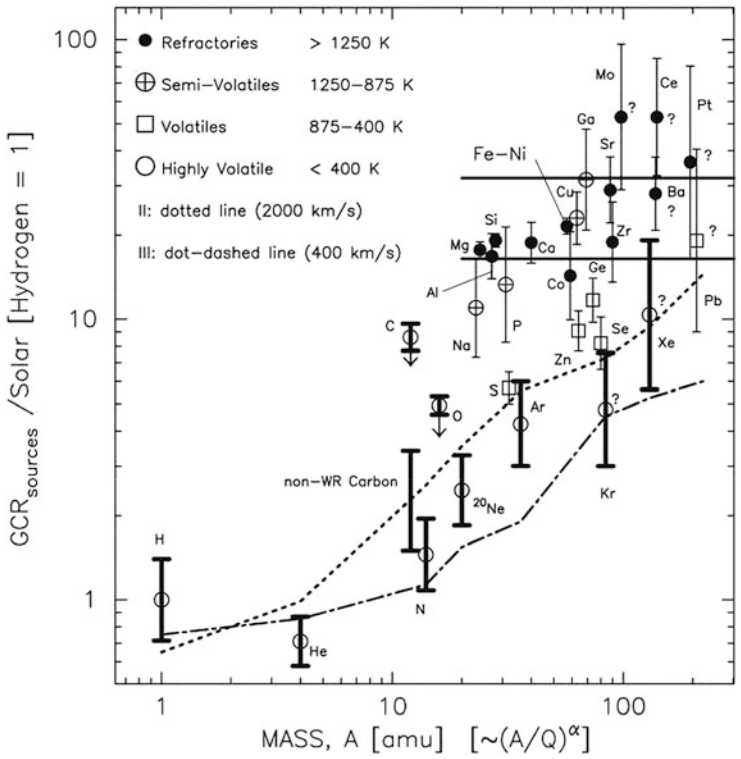

Fig. 7.23 GCR source abundance relative to solar abundance vs. atomic mass number. All values are measured relative to GCR hydrogen at a given energy per nucleon. The elements are divided, on the basis of condensation temperature, into refractory, semivolatile, volatile, and highly volatile groups. The refractories are essentially completely locked in grains in the ISM, while the highly volatile ones are gaseous. The arrows on carbon and oxygen indicate that these elements have an additional source from ^{22}Ne-C-O enriched Wolf-Rayet wind material. Model predictions for the abundances of volatile elements from a high Mach number shock model are shown with a dotted line, and those for a lower Mach number model with a dot-dashed line. The horizontal solid lines on the right side of the plot are limits on predicted abundance of iron and other refractory elements. The label on the abscissa [$\sim(A/Q)^{\alpha}$, where α is some unspecified constant] is a reminder that, for most ionization models, A/Q is a roughly monotonically increasing function of mass. The abundances of Kr, Xe, Mo, Ba, Ce, Pt, and Pb relative to Fe may contain systematic errors that are difficult to evaluate (indicated with a question mark) (from Ellison et al. 1997)

Despite its success, the model relies on several assumptions which lack empirical support (notice, however, that interplanetary dust particles display traces of grain acceleration, as reported by Westphal and Bradley (2004).

In view of the complexities introduced by fractionation, it appears safer to rely either on refractory primary elements (unaffected by fractionation) or to ratios of isotopes belonging to the same element (since fractionation effects cancel out), in order to probe the source composition of GCR. The ACE/CRIS observations allowed to determine the primary GCRS abundances of 19 refractory nuclides,

belonging to Mg, Al, Si, Ca, Fe and Ni. As reviewed in Wiedenbeck et al. (2007) those nuclides have a solar composition (within uncertainties), with the possible exception of ^{58}Fe. Since more than half of solar Fe come from a *long-lived* source (SNIa, Goswami and Prantzos 2000), the GCRS composition has to originate from an extremely well mixed sample of the ISM (or of solar type stars).

Contrary to the refractory nuclides, the volatile ^{22}Ne/^{20}Ne ratio in the GCR source has long been known to exceed its solar value by a factor of $\sim$5. This excess of ^{22}Ne is attributed to the contribution of Wolf-Rayet winds to GCRs, as originally suggested by Casse and Paul (1982) and quantitatively elaborated in subsequent studies (e.g. Prantzos et al. 1985).

It is not clear at present whether the totality of the GCRS composition originates from the same site (where the nucleosynthetic products of many stars and SN are well mixed) or whether it originates as a diversified sample of nuclei (produced from a variety of sources distributed all over the Galaxy), which are mixed well after their acceleration by SN shocks, during their 10^7 years travel through the Milky Way. The latter case corresponds to the, now defunct, FIP-based paradigm of GCRS composition (Meyer 1985). The former possibility is now embodied in the *super-bubble* paradigm, advocated in Higdon et al. (1998) and further supported by Binns et al. (2005) on the basis of the ^{22}Ne/^{20}Ne analysis. GCR (both refractories produced by sputtered grains and volatiles) are accelerated—with higher efficiency than in the normal ISM—from the thermal pool of ions present in a super-bubble, which is created and chemically enriched by the action of dozens or hundreds of stars and SN. In that model, SN explosions have to occur $>10^5$ years apart from each other, in order to allow for *e*-capture decay of ^{59}Ni, which is absent in arriving GCR (see next section).

The super-bubble paradigm has been criticized on several grounds in Prantzos (2012), who showed that a superbubble, resulting from explosions of a representative sample of massive stars, is expected to have a solar ^{22}Ne/^{20}Ne ratio and cannot explain the excess observed in GCRs.

7.4.1.1 Radioactive Isotopes in Cosmic Rays

Radioactive nuclides present in GCR may provide key information about various timescales concerning the acceleration and propagation of cosmic rays in the Galaxy. Primary nuclides unstable against $\beta^{\pm}$ and α decays or spontaneous fission, are sensitive to the timescale between nucleosynthesis and arrival on Earth; however, U and Th have such large lifetimes that they are essentially stable during the propagation of GCR in the Galaxy and they cannot be used as probes of that timescale. Primary nuclides unstable against *e*-capture only, are sensitive to the timescale from their nucleosynthesis to acceleration, since after acceleration to GCR energies they can hardly capture an orbital electron and they propagate essentially without decay; ^{57}Co and, especially, ^{59}Ni belong to this category. Secondaries unstable against $\beta^{\pm}$ and α decays or spontaneous fission can probe the residence timescale of GCR in the Galaxy, provided their half-lives are comparable to

Table 7.1 Decay modes and half-lives of key secondary radioactivities in GCR (from Yanasak et al. 2001)

Isotope	Decay mode	Mode half-life (year)
^{10}B	β^-	1.51×10^6
^{14}C	β^-	5.70×10^3
^{26}Al	β^+	8.73×10^5
	e-Capture	8.45×10^6
^{36}Cl	β^-	3.07×10^5
	e-Capture	1.59×10^7
^{54}Mn	β^-	$(6.3 \pm 1.7) \times 10^5$
	e-Capture	0.8548

that timescale; a handful of nuclides belong to this class (see Table 7.1). The GCR residence time, combined with the mean path length (obtained from the secondary/primary ratio) and the particle velocity, allows one to evaluate the mean density of the ISM traversed by GCR. Finally, secondary nuclides unstable against e-capture only, can be used as probes of re-acceleration effects, because e-capture is more likely at low energies. The next two subsections summarize the excellent review of Mewaldt et al. (2001) on radioactivities in GCR.

7.4.2 Observations of Cosmic Rays

7.4.2.1 Spectra and Composition

Spectra of Galactic cosmic rays as measured in Earth's vicinity have the same overall shape for all chemical elements. Above a few GeV/nucleon, and up to 10^6 GeV/nucleon, the GCR intensity $I(E)$ (in cm^{-2} s^{-1} st^{-1} GeV^{-1}) is described by a practically featureless power-law as a function of kinetic energy E

$$I(E) \;=\; 1.8\, E^{\alpha} \tag{7.3}$$

with slope $\alpha = -2.7$. At $E \sim 10^6$ GeV/nucleon (the *knee*), the GCR spectrum steepens to $\alpha = -3$. At E<1 GeV/nucleon, the GCR spectrum progressively flattens (with α becoming even positive) and its intensity varies, in a way which anti-correlates with the solar activity (*solar modulation*); the solar wind prevents the lowest energy GCR from entering the heliosphere. Correcting for that effect (*demodulating*) allows one to infer, through the time-averaged locally observed spectra, the *true* spectrum of GCR as they propagate in the ISM (Fig. 7.24). This allows one to evaluate the kinetic energy density of GCR ϵ_{GCR} as

$$\epsilon_{GCR} \;=\; 4\pi \int \frac{E_k}{\upsilon}\, I(E)\, dE \tag{7.4}$$

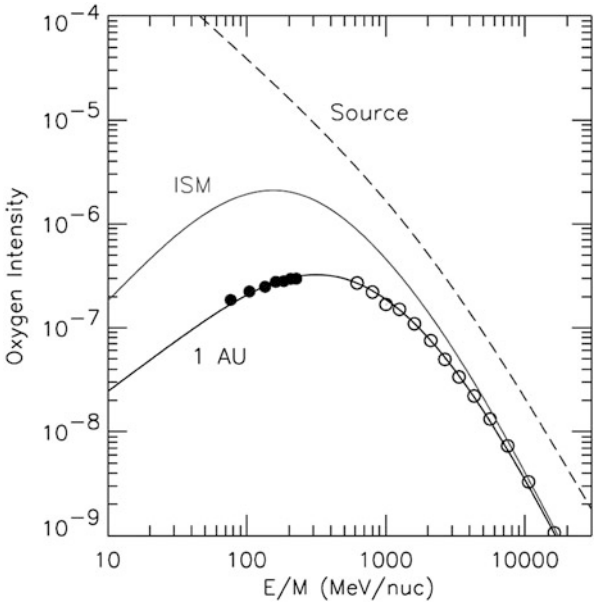

Fig. 7.24 Low energy GCR spectra of oxygen, observed near Earth (*bottom*, in the ISM (demodulated for the solar wind, *middle*) and in the GCR source (theoretically inferred, *top*) (from Wiedenbeck et al. 2007)

where υ is the velocity of a particle with kinetic energy E. The inferred local GCR energy density is $\epsilon_{GCR} \sim 1\,\mathrm{eV\,cm^{-3}}$. It is comparable to the local energy densities of starlight (ϵ_{Light}), of ISM gas thermal motion ($\epsilon_{Gas} \sim n\kappa T$) and of the magnetic field ($\epsilon_B \sim \frac{B^2}{8\pi}$), i.e. GCR constitute an important dynamical agent in the Galaxy.

As seen above, GCR are expected to be confined for a timescale $\tau_{Conf} \sim 10^7$ years in the Galactic disk (before escaping to the halo and then to the intergalactic space), i.e. in a roughly cylindrical volume V of radius $R \sim 15\,\mathrm{kpc}$ and height $h \sim 4\,\mathrm{kpc}$. Assuming that ϵ_{GCR} is the same throughout that volume, one finds that the total GCR power is $P_{GCR} = \epsilon V/\tau_{Conf} \sim 2 \times 10^{41}\,\mathrm{erg\,s^{-1}}$. Taking into account the expected supernova frequencies in the Milky Way ($f_{GalSN} \sim 2\,\mathrm{century^{-1}}$) and assuming a kinetic energy of $E_{SN} = 1.5\ 10^{51}\,\mathrm{erg}$ for each SN, one sees that $P_{GCR} \sim 0.1\ P_{GalSN}$ (where $P_{GalSN} = f_{GalSN} E_{SN} \sim 1.5 \times 10^{42}\,\mathrm{erg\,s^{-1}}$). Those numbers suggest that supernova remnants accelerate cosmic rays in the Galaxy with an efficiency of the order of 10%.

The composition of cosmic rays arriving at Earth is best measured in the low energy range (0.1–1 GeV/nucleon), because in that region GCR intensity is highest and experimental techniques for particle identification have better resolution than at higher energies. In Fig. 7.25, the arriving GCR composition is compared to the solar system one. Both samples of matter are dominated by the elements H, He, C, O, Ne, Mg, Si and Fe. The overall similarity of the two abundance curves suggests that they have similar nucleosynthetic origin, i.e. from massive stars and supernovae (for nuclei in the C-Fe peak range). Volatile elements (He, O, Ne, S and Ar) are somewhat depleted relative to refractory Si, perhaps as a result of some fractionation process, favouring the acceleration of more refractory elements (see next section).

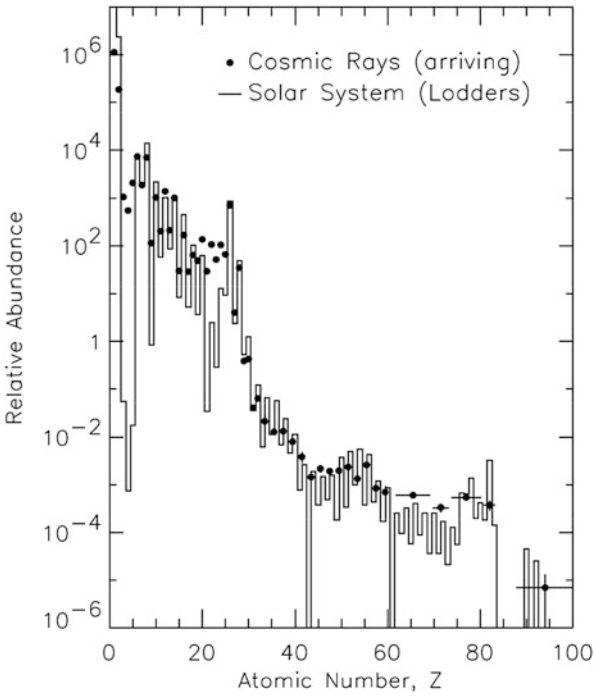

Fig. 7.25 Elemental abundances in arriving GCR (*dots*), compared to the solar system ones (*histogram*) (from Wiedenbeck et al. 2007)

The most striking difference between GCR and solar abundances is the GCR overabundance of some nuclides which are relatively rare in the solar system composition. The atomic numbers of those rare nuclides are only a few units below those of the nuclides dominating the abundance curves. This is the case of e.g. Li, Be and B with respect to the slightly heavier C, N and O nuclei $\left(\left(\frac{LiBeB}{CNO}\right)_{solar} \sim 10^{-6}\right.$, while $\left.\left(\frac{LiBeB}{CNO}\right)_{GCR} \sim 10^{-1}\right)$ or of Sc, Ti and V nuclei with respect to Fe peak nuclei (see Fig. 7.25). The relative overabundance of those rare nuclei in GCR has long been recognised to be the result of their *secondary* nature: they are produced by the nuclear fragmentation (*spallation*) of their heavy progenitors (*primaries*), during the GCR propagation in the ISM.

The properties of GCR secondaries, both stable and radioactive, provide important information on the physics of Galactic cosmic rays.

7.4.2.2 Radioactive Clocks and Cosmic-Ray Timescales

Determination of the confinement (or residence or escape) timescale τ_{Conf} of GCR in the Galaxy is a key issue, because τ_{Conf} determines the power required to sustain the energy density of GCR (see Sect. 7.4.2). All four nuclides of Table 7.1 have been measured in arriving GCR after the Ulusses and ACE results and the situation is summarized in Fig. 7.26. Confinement times are obtained in the framework of a

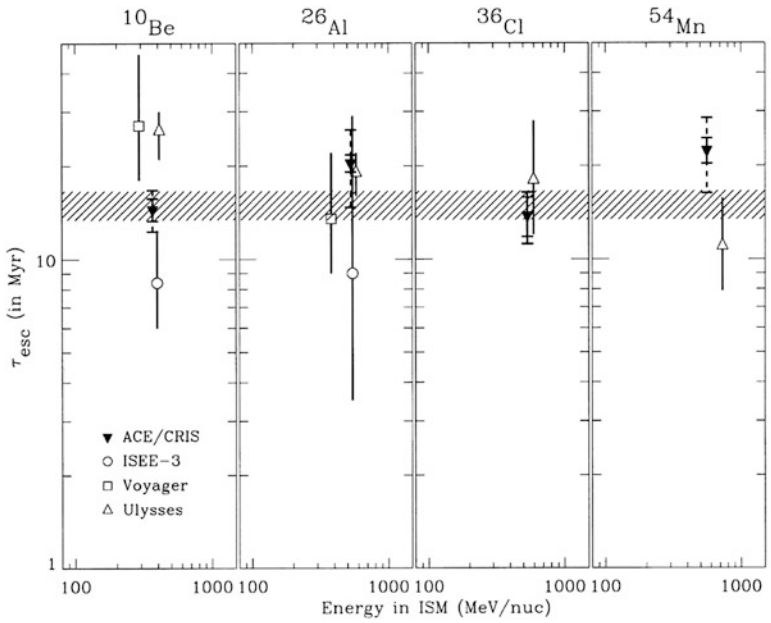

Fig. 7.26 Confinement times obtained by ACE/CRIS and previous experiments. Uncertainties shown with solid error bars are 1 standard deviation statistical. The average value of the confinement time, $\tau_{esc} = 15.0 \pm 1.6$ Myr, indicated by the CRIS data for the four clock isotopes is shown as a hatched band (From Yanasak et al. 2001)

Leaky box model with energy dependent escape length and the average value τ_{Conf} is found to be 15.0 ± 1.6 Myr. In the Leaky box model, $\tau_{Conf} = \Lambda_{esc}/(\upsilon\rho)$, where $\upsilon = \beta c$ is the GCR velocity (at <1 GeV/nucleon, the effects of solar modulation have to be accounted for in the calculation of β). This allows one to evaluate the average ISM density traversed by GCR as $n = \rho/m_p$ =0.36 H atoms cm^{-3} (Yanasak et al. 2001). This is a factor of ~3 lower than the canonical value of the local ISM density (~1 H atom cm^{-3}).

In the Leaky box model, where GCR intensities and ISM densities are uniform in the GCR propagation volume (and in time), such measurements can probe only the average density of the confinement region. The above result implies that GCR spend a large fraction of their confinement time in a volume of smaller average density than the one of the local gas, i.e. in the Galactic halo. In more realistic models, involving e.g. diffusion (see Strong et al. 2007), the aforementioned radioactivities probe a volume of radius R which is limited by their mean life τ, such that $R \sim (\gamma D\tau)^{1/2}$, where D is the spatial diffusion coefficient and $\gamma = (1-\beta^2)^{-1/2}$. In that scheme, at 1 GeV/nucleon, ^{10}Be probes regions out to ~400 pc (i.e. beyond the gaseous layer), while ^{14}C probes the immediate vicinity of the solar system; however, its expected signal is lower than the background due to ^{14}C produced inside the ACE/CRIS instrument. Notice that uncertainties in the derived ISM

densities are dominated by uncertainties in fragmentation cross-sections, rather than by measurement uncertainties (Yanasak et al. 2001).

Finally, in diffusion models of GCR propagation, the expected surviving fraction of secondary radioactivities depends on the assumed diffusion coefficient D. Comparing the ACE/CRIS measurements for ^{10}Be, ^{26}Al and ^{36}Cl at 400 MeV/nucleon with theoretical predictions of Ptuskin and Soutoul (1998), values of $D \sim 2 \times 10^{28}$ cm^2 s^{-1} are found (see Fig. 9 in Mewaldt et al. 2001).

Radionuclides unstable to e-capture, if accelerated to >500 MeV/nucleon, become fully stripped of orbital electrons, and cannot decay. This suggests that, if $f = X/D_X$ (the abundance fraction of such a nuclide X relative to its decay product D_X) arriving on Earth $>>1$, then the timescale Δt between the nucleosynthesis and acceleration of X is smaller than its decay timescale τ_X by e-capture; inversely, an arriving fraction $f = X/D_X <<1$ would imply that $\Delta t > \tau_X$. Three such radionuclides were identified by Soutoul et al. (1978) as potentially important in that respect: ^{56}Ni, ^{57}Co and ^{59}Ni, with half-lives against e-capture from 6 days to 7.6×10^4 years. It is well known now that ^{56}Ni is the dominant product of explosive nucleosynthesis in supernovae, however, GCR composition is dominated by its decay product ^{56}Fe; thus, Δt is much larger than 6 days.

The most interesting case is the one of ^{59}Ni, which probes rather large values of the timescale Δt. Nucleosynthesis calculations (Woosley and Weaver 1995) suggest that ~2/3 of the A = 59 isobars is synthesized as ^{59}Ni The analysis of ACE/CRIS data showed that very little (if any at all) ^{59}Ni exists in arriving GCR, while its daughter nuclide ^{59}Co is present at the level of ^{59}Co/^{60}Ni~0.25 (Fig. 7.27). An absence of ^{59}Ni from GCR implies that $\Delta t > 10^5$ years.

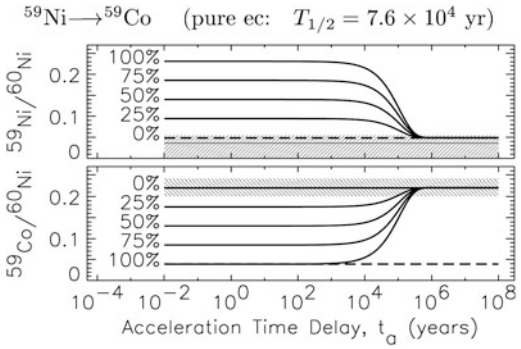

Fig. 7.27 Calculated abundances at Earth of ^{59}Ni/^{60}Ni (upper panel) and ^{59}Co/^{60}Ni (lower panel) are shown as a function of the time delay between nucleosynthesis and GCR acceleration. Calculated abundances are a combination of a secondary component (*dashed lines*) produced by nuclear fragmentation during transport and a surviving primary component. The different curves correspond to different assumed fractional contributions of ^{59}Ni in the primary A=59 material, as indicated by the labels on the curves. The time dependencies are the result of the exponential decay of the primary ^{59}Ni into ^{59}Co as the result of the electron-capture decay of ^{59}Ni before acceleration. The hatched regions indicate the abundances measured with CRIS, including 1 σ uncertainties. *From* Wiedenbeck et al. (1999)

Such a long timescale between nucleosynthesis and GCR acceleration would have important implications for our understanding of GCR composition. It would imply that SN cannot accelerate their own ejecta: even in a rarefied medium, the SN ejecta are completely diluted in (and mixed up with) the interstellar gas on timescales as long as 105 years.

There is a loop-hole to the above argument: while *e*-capture is essentially impossible at sufficiently high energies (>500 MeV/nucleon), it becomes possible at lower energies. The average energies of ACE/CRIS measurements (∼300 MeV/nucleon) correspond to ∼450 MeV/nucleon outside the heliosphere. If ^{59}Ni would not be directly accelerated to high energies after its ejected from the supernova source, it might capture an electron and decay before it became a cosmic-ray component. In that case, its absence in arriving GCR provides no information on a delay between its nucleosynthesis and acceleration.

Recent updates of supernova yields, including the effects of stellar rotation, however obtain (Neronov and Meynet 2016) a much lower abundance of ^{59}Ni compared to ^{59}Co, compared to the earlier supernova nucleosynthesis calculations (Woosley and Weaver 1995). This then reduces the abundances that would be expected in cosmic rays even excluding any decay prior to acceleration. Therefore the above-discussed exploitation of the decay properties of ^{59}Ni may have been premature.

There is an important issue of GCR, which is re-acceleration: do GCR get their high energies in a single SN blast wave, or in a series of SN shock waves (*distributed acceleration*)? Secondary radionuclides, unstable against *e*-capture, with short enough timescales, can be used as probes of such processes: these include ^{7}Be, ^{37}Ar, ^{44}Ti, ^{49}V, ^{55}Fe, with laboratory lifetimes extending up to 67 years. Comparing the measured abundance ratios of those nuclides to their stable daughter nuclei in various energy bands, one may, in principle, constrain the extent of re-acceleration. Unfortunately, the analysis of observations from various experiments (*Ulysses, Voyager, ACE*) has produced contradicting results up to now. However, as stressed in Mewaldt et al. (2001), measurements of *e*-capture radionuclides in GCR are still in their infancy. The same holds for models to interpret the data, which suffer from uncertainties related to cross-sections (for fragmentation, *e*-capture and loss as a function of energy), the history of GCR acceleration and re-acceleration, inhomogeneities of the ISM, etc. Improvements in both measurements and interpretation will contribute to a much better understanding of the physics of GCR propagation (Fig. 7.28).

Spallation of cosmic rays during their journey has been shown above to produce a number of interesting radioactive species. However, the discovery of ^{60}Fe in cosmic rays (Binns et al. 2016; Fig. 7.28) came as a surprise, because this cannot originate from such spallation.

The detection of ^{60}Fe thus must be understood from a different viewpoint: As Binns et al. (2016) argue, its detection presents an upper limit on the time it takes to accelerate cosmic rays. ^{60}Fe obviously survived a journey from its production through acceleration to detection, which is compatible with its 3.6 Myr radioactive lifetime, that, in this case, is independent of the atomic electron shell population.

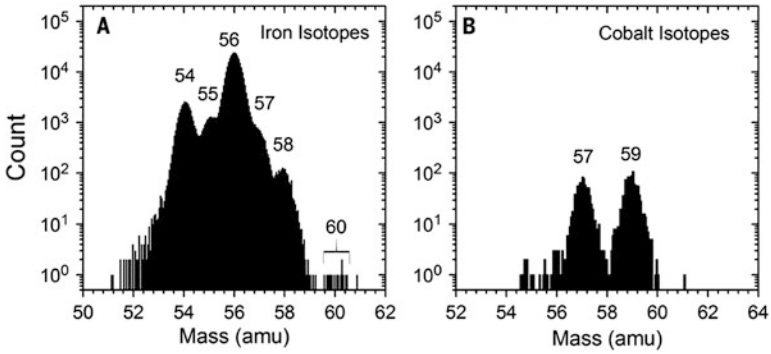

Fig. 7.28 Composition of iron and cobalt isotopes in cosmic rays near Earth (as observed with ACE/CRIS Binns et al. 2016)

Binns et al. (2016) argue that only less than 10% of their detected ^{60}Fe isotopes could originate from heavier nuclei being fragmented and hence be 'secondary', and most of the nuclei therefore are considered 'primary'. They use then a simple diffusive propagation model to argue for an origin within 620 pc of the Sun, making supernovae from the Scorpius-Centaurus association potential sources. The propagation of ejecta from source to detector obviously remains a major scientific issue today.

It is interesting that, from a different viewing point, Kachelrieß et al. (2015) infer from the anisotropy of the cosmic ray spectral signatures that a nearby supernova explosion a few Myrs ago is suggested, to provide peculiar conditions for cosmic ray acceleration in the nearby interstellar medium. Taken together, this is reminiscent of the scenario discussed above for the Scorpius Centaurus association and its history of the past 10–20 Myrs (Sect. 7.2.4.3).

7.5 Positrons and Their Annihilation

One of the most direct and unambiguous manifestations of radioactivity is the emission of positrons from the β^+ decay of unstable nuclei. Such nuclei are located on the proton rich side of the valley of nuclear stability in the isotope chart. This is the case, e.g., for ^{26}Al, ^{44}Ti or ^{56}Ni and ^{56}Co, produced in massive stars and supernova explosions, also for ^{13}N, ^{14,15}O, ^{17}F, and ^{22}Na produced in novae. If the lifetime of the unstable nucleus is larger than the timescale τ_T that may be characteristic for the *trapping* of the positrons within the expanding explosive production site, then a substantial fraction of the released positrons may escape from that site of nucleosynthesis and find its way into the interstellar medium. Most of the positrons from the decay of ^{44}Ti ($\tau \sim 89$ years) and ^{26}Al ($\tau \sim 1$ Myr), and ^{22}Na ($\tau \sim 3.8$ years) are therefore expected to be released within the interstellar medium, while the fate of those released by short-lived ^{56}Ni ($\tau \sim 8.8$ days) and

^{56}Co (τ ~77 days) is not clear. Note that, for example, the late bolometric emission from supernovae that is seen after 100–1000 days mostly is energised by the energy deposits from positrons within the expanding supernova.

But there is a variety of other candidate sources of positrons, either through pair plasma production in high-density and high-energy environments, or from high-energy particle collisions, or even dark matter annihilation or decay.

Positrons have been observed directly in particle detectors, but more commonly their annihilation is seen, through a characteristic gamma-ray signature that involves a unique line at 511 keV. First measured from the Sun in solar flares (Chupp et al. 1973), the gamma-ray signals of positron annihilation were observed from our Galaxy's central region (Leventhal et al. 1978; Purcell et al. 1993; Knödlseder et al. 2005; Siegert et al. 2016b) and also from transient sources (Sunyaev et al. 1992; Bouchet et al. 1991; Siegert et al. 2016a). By now, imaging and spectroscopic results have been established, which make cosmic positrons to be one of the major current puzzles in astrophysics. Prantzos et al. (2011) have reviewed this topic in great detail; we summarise this here, with some updates since their review. This Section describes the processes relating positrons across all energies to their annihilation gamma-ray signature, with an aim to learn about the contributions from radioactivities.

7.5.1 Candidate Sources and Expected Observables

Positrons can be produced either by radioactivity in stars, novae and supernovae, or through various high energy processes in compact objects (production of positrons by cosmic rays, which are accelerated by supernovae, belongs to the latter class); processes involving dark matter (DM) annihilation, decay or de-excitation is a third possibility.

Among the various astrophysical sources of positrons proposed so far, the only one known certainly[5] to release e^+ in the ISM is β^+ radioactivity of ^{26}Al; the observed intensity of its characteristic 1.8 MeV emission in the Galaxy corresponds to $\sim$ 3–4 $\times$ 10^{42} e^+ s^{-1}. A similar amount is expected from the decay of ^{44}Ti, on the grounds of nucleosynthesis arguments (it is the parent nucleus of stable ^{44}Ca). Both radionuclides are produced mostly in massive stars and their positrons should be released along the Galactic plane, as traced by the 1.8 MeV emission; they could thus account for the observed disk 511 keV emission.

Radioactivity of ^{56}Co from SNIa was traditionally considered to be the major e^+ producer in the Galaxy. Both the typical ^{56}Ni yield of a SNIa and the Galactic SNIa rate are rather well constrained, resulting in 5 $\times$ 10^{44} e^+ s^{-1} produced *inside* SNIa. If only f_{esc} ~4% of them escape the supernova to annihilate in the ISM, the

[5]That is, by proof from observations: ^{26}Al gamma rays are observed, and ^{26}Al decay is known to emit positrons.

observed total e^+ annihilation rate can be readily explained. However, observations of two SNIa, interpreted in the framework of 1-D (stratified) models, suggest that the positron escape fraction is negligible *at late times*. On the other hand, both observations of early spectra and 3-D models of SNIa suggest that a sizeable fraction of ^{56}Ni is found at high velocity (close to the surface), making—perhaps—easier the escape of ^{56}Co positrons. SNIa remain a serious candidate, with a potential Galactic yield of 2×10^{43} e^+ s^{-1}. But the expected spatial distribution of SNIa in the Galaxy would predict a much smaller bulge-to-disk ratio than the one of the observed 511 keV profile.

Several candidate sources will likely produce positrons through various high-energy processes: pulsars, millisecond pulsars, magnetars, accreting binary systems such as microquasars, and the central supermassive black hole (SMBH) in the Milky Way. There is little observational evidence that either of those sources produces positrons, however, and the e^+ yields evaluated by various authors are often (intentionally) optimistic rather than typical values. Among those sources, the most promising appear to be accreting binaries and the massive black hole at the Galactic centre. Binaries are observed as LMXRB X-ray sources; the microquasar variant of that class of sources with its plasma jets are plausible positron sources. In one case, a flaring microquasar has been shown to emit a gamma-ray signal that suggests the presence and ejection of high-energy positrons (see below). Because of the current low activity of the central SMBH it has to be assumed that the source was much more active in the past, thus dropping the assumption of *steady state* between e^+ production and annihilation, which is adopted in all other cases.

Positrons originating from radioactive decay are released with typical energies as they are characteristic of the difference between nuclear energy levels, i.e. of the order of ∼MeV. With their rest mass energy of 511 keV, these positrons will thus have relativistic velocities. The alternative source processes for positrons fall into two classes, with respect to positron energies: If pair plasma is involved, and the source is compact and at rather high density, back-reactions between charged particles and photons (also virtual photons representing a high magnetic field) will limit production processes by the pair creation threshold to energies around MeV. In the case of relativistic jets, this may be boosted by relativistic motion. If the production region is less extreme, the positron energy is not limited from such considerations, and depends on the primary particle energies. In pulsar magnetospheres, therefore, GeV to TeV energies can be reached. For secondary processes involving dark matter, the mass of the dark matter particle sets an upper limit; commonly, masses of GeV and above are considered plausible.

7.5.1.1 Signatures of Positron Annihilation

Once in the interstellar medium, the positrons slow down through the various processes of Inverse-Compton scattering, synchrotron emission, Coulomb collisions, ionization losses, and finally they can annihilate when at eV energies (Bussard et al. 1979). Annihilation may occur either directly with electrons, or after formation of

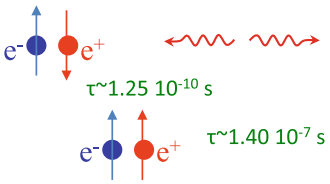

Fig. 7.29 The two configurations of the positronium atom, as an intermediate stage before annihilation of a positron with an electron

a *positronium* atom (with the positron substituting the positively-charged atomic nucleus); momentum conservation sets constraints. In both cases, the characteristic γ-ray line at 511 keV is emitted, whereas annihilation from a positronium also produces a γ-ray continuum below 511 keV.

The annihilation of a positron with an electron releases a total (rest-mass) energy of 1022 keV in the form of two or more photons. Direct annihilation of a e^--e^+ pair at rest produces two photons of 511 keV each. The situation is more complex in the case of positronium (Ps). Positronium has two basic states, depending on the relative orientations of the spins of the electron and the positron (see Fig. 7.29). The singlet state has antiparallel spins, total spin S = 0, is denoted as $^1S_0$ and is known as *para-positronium* (p-Ps). The triplet state has parallel spins, total spin S = 1, is denoted as $^3S_1$ and is known as *ortho-positronium* (o-Ps). From the (2S + 1) spin degeneracy, it follows that Ps will be formed 1/4 of the time in the p-Ps state and 3/4 of the time in the o-Ps state. The energy difference between the two spin states (*hyperfine splitting*) is 8.4×10^{-4} eV. Transitions between these states similar to the spin-flip transition in hydrogen, which produces the astrophysically-important 21 cm line of HI, are unimportant due to the short Ps lifetimes.

Spin and momentum conservation control the release of annihilation energy in the form of photons. Para-positronium annihilation releases two photons of 511 keV each in opposite directions (as in the case of direct e^--e^+ annihilation). Ortho-positronium annihilation requires a final state with more than two photons from spin conservation; momentum conservation distributes the total energy of 1022 keV among three photons producing a continuum of energies up to 511 keV (Fig. 7.30). The corresponding lifetimes before annihilation (in vacuum) are 1.2×10^{-10} s for para-Ps and 1.4×10^{-7} s for ortho-Ps (see Fig. 7.29).

If a fraction f_{Ps} of the positrons annihilate via positronium formation, then the 3-photon γ-ray continuum of ortho-positronium will have an integrated intensity of

$$I_{3\gamma} \propto \frac{3}{4}\, 3\, f_{Ps} \tag{7.5}$$

The remaining fraction $1 - f_{Ps}$ will annihilate directly to 2 photons of 511 keV each. We should add to this the 2-photon contribution of the para-Positronium state, so that the 2-photon (511 keV line) intensity will be:

$$I_{2\gamma} \propto 2(1 - f_{Ps}) + \frac{1}{4}\, 2\, f_{Ps} = 2 - 1.5\, f_{Ps} \tag{7.6}$$

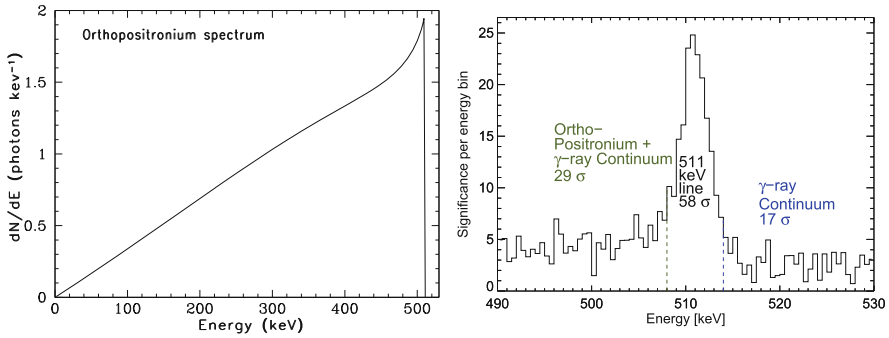

Fig. 7.30 *Left:* Spectrum of ortho-positronium annihilation with the three-photon continuum (from Ore and Powell 1949). *Right:* Spectrum of the annihilation emission measured by SPI, with the 511 keV line and the 3-photon continuum from annihilation through positronium. An underlying Galactic continuum emission is seen as well (from Siegert et al. 2016b)

This expected spectrum is shown in Fig. 7.30. By measuring the intensities of the 511 keV line and of the Ps continuum one can then derive the positronium fraction

$$f_{Ps} = \frac{8\, I_{3\gamma}/I_{2\gamma}}{9 + 6 I_{3\gamma}/I_{2\gamma}} \tag{7.7}$$

This quantity offers a valuable diagnostic of the physical conditions of the ISM where positrons annihilate, as these impact on the positronium formation efficiency.

7.5.1.2 Issues of Positron Transport in the Interstellar Medium

The propagation and transport of positrons has important implications for the interpretation of Galactic 511 keV emission with respect to positron origins (first raised by Prantzos 2006a). Positrons injected from various sources interact with the surrounding medium either through collisions (collisional transport) or through interaction with plasma waves (collisionless transport). If only limited by collisions with ambient gas, MeV particles can propagate large distances—of the order of 10 kpc/n (n is the local density in cm^{-3}). These distances would be shorter by a factor 0.75 if the tangled components of the magnetic field are added (Jean et al. 2009; Alexis et al. 2014). Such distances are much larger than the typical sizes of structures in the hot and warm phases of the ISM.

Collisionless transport is governed by wave-particle interactions (Bykov and Treumann 2011). In the case of a magnetised plasma, positrons spiral along the magnetic field lines. The gyroradius of a positron with Lorentz factor γ is $r_g \sim 1.7 \times 10^9\ B_{\mu G}^{-1} (\gamma^2 - 1)^{1/2}$ cm, where the local mean magnetic field $B_{\mu G}$ is expressed in μG. In a magnetised, turbulent, plasma, the most efficient of collisionless processes is scattering off magnetic fluctuations of size $r_B \simeq r_g$, which induce *resonant* pitch

angle scattering of positrons (e.g. Kulsrud 2005, and references therein), or *non-resonant* interactions with fluctuations on scales just above r_g (see e.g. Toptygin 1985; Ragot 2006). The resonant interactions involve either the particle gyromotion around the mean magnetic field (*cyclotrotron resonance*) or the parallel motion of the particle along the field line (*Cherenkov resonance*). The Larmor radius of the resonant positron being small—of the order of $r_g \simeq 10^9$cm and the positron-gyromotion polarisation being left-handed only MHD waves (Alfvén or fast magneto-sonic) can fulfil the resonance conditions. Non-resonant compressible perturbations may also affect the positron mean free path, as it seems to be the case for sub-MeV electrons in the solar wind, where there are strong indications for MeV electron re-acceleration (Ragot 1999). Moreover, *adiabatic deceleration* of positrons in jets or expanding shells (for example in SN remnants) results in positron cooling, even without Coulomb collisions; this occurs if the positron mean free path, which is dominated by e^+ scattering by waves, is shorter than the typical scale of bulk plasma motion.

In summary, wave-particle interactions, both resonant and adiabatic non-resonant, could result in particle deceleration, but also *re-acceleration*, depending strongly on the local conditions. The transport of energetic (>GeV) Galactic cosmic rays is driven by such collisionless processes. The case of MeV positrons is not clear, as the level and scale of interstellar turbulence is not well understood.

For low-energy positrons, Alexis et al. (2014) performed a detailed Monte Carlo study of propagation in the various phases of the ISM and found that propagation over distances larger than ∼1 kpc through the Galaxy seems rather unlikely (neglecting, however, any re-acceleration). This implies that the morphology of the 511 keV emission does not necessarily reflect the morphology of the underlying e^+ source distribution, as propagation up to kpc distances appears possible. As an example, positrons from SNIa are expected to be released away from dense gas and in the hot and rarefied ionised medium, since the scale height of SNIa is considerably larger than the scale height of the cool, dense gas in the Galactic disk (see Fig. 11.15). Another example is the release of massive star nucleosynthesis ejecta with preference in large superbubbles surrounding somewhat-evolved massive star groups (see Sect. 7.2.3). The e^+ propagation distances could then be quite large, possibly with channels open towards the Galactic halo ('chimneys'), thus allowing e^+ from the disk to annihilate far away from their sources (perhaps in the halo, where a low surface brightness emission should be expected). We shall discuss further those issues in the last section of this chapter.

7.5.2 *Observations of Positrons*

The 511 keV emission of interstellar e^+ annihilation was first detected from the general direction of the Galactic centre in the early 1970s, by balloon borne experiments of low energy resolution (Johnson et al. 1972). It was unambiguously identified a few years later with high resolution Ge detectors (Leventhal et al. 1978).

It is the first and most intense γ-ray line originating from outside the solar system that was ever detected. Its flux on Earth ($\sim 10^{-3}$ cm^{-2} s^{-1}), if combined with the distance to the Galactic center ($\sim$8 kpc) (assuming that annihilation occurs in the inner Galaxy), implies the annihilation of $\sim 2 \times 10^{43}$ e$^+$ s^{-1} (see below), releasing a power of $\sim 10^{37}$ erg s^{-1} or $\sim 10^4$ L$_\odot$ in γ-rays. Assuming a steady state, i.e. equality between production and annihilation rates of positrons, one should then seek for a source able to provide $\sim 2 \times 10^{43}$ e$^+$ s^{-1}. If the activity of that site were maintained at such level during the $\sim 10^{10}$ years of the Galaxy's lifetime, a total amount of positrons equivalent to $\sim$3 M$_\odot$ would have been annihilated.

Imaging the Galaxy in annihilation γ-rays was considered to be the exclusive way to identify the cosmic e$^+$ sources (assuming that the spatial morphology of the γ-ray emission reflects the spatial distribution of the sources, i.e. that positrons annihilate close to their production sites). Because of the difficulties of imaging in the MeV region, progress was extremely slow in that field: Only in the 1990s the first hints on the spatial distribution of the 511 keV emission were obtained by the OSSE instrument aboard the Compton Gamma Ray Observatory (CGRO, Cheng et al. (1997); Purcell et al. (1997); see Chap. 10). The first reliable imaging of the 511 keV emission was obtained by the SPI coded-mask imaging instrument aboard ESA's INTEGRAL Gamma Ray Observatory (see Chap. 10). Around 0.5 MeV, SPI has a spatial resolution of 3° (FWHM) and a spectral resolution of $\sim$2.1 keV (FWHM, at 0.5 MeV). This allows for imaging, but also a spatially resolved fine spectroscopy of the signal (including the underlying continuum emission).

7.5.2.1 Imaging Studies

The first all-sky maps of positron annihilation gamma rays, which have been presented from 1 year of observations by Knödlseder et al. (2005) for the 511 keV line and for the positronium continuum Weidenspointner et al. (2006b), respectively (see Fig. 7.31), showed that the emission is strongly concentrated in the inner Galaxy, and much weaker brightness is seen from the Galactic disk (Weidenspointner et al. 2008). These two maps are identical within their uncertainties, which suggests that the positronium fraction does not vary much over the different emission regions across the sky.

The images show a remarkable predominance of the spheroidal component from the inner Galaxy. The earlier imaging study with OSSE had suggested a clear emission component from the Galactic disk, but this seemed to be completely absent in the first images made with SPI (see Fig. 7.31 top). Also model fitting indicated only a marginal signal from the Galactic disk, and a bulge-to-disk flux ratio > 1 had been suggested (Knödlseder et al. 2005).

This emission morphology is strikingly-different than the ones seen in any other wavelength for radiation from the Galaxy. Such strong dominance of the Galactic bulge, unseen in any other wavelength, stimulated above-mentioned *unconventional* models involving dark matter.

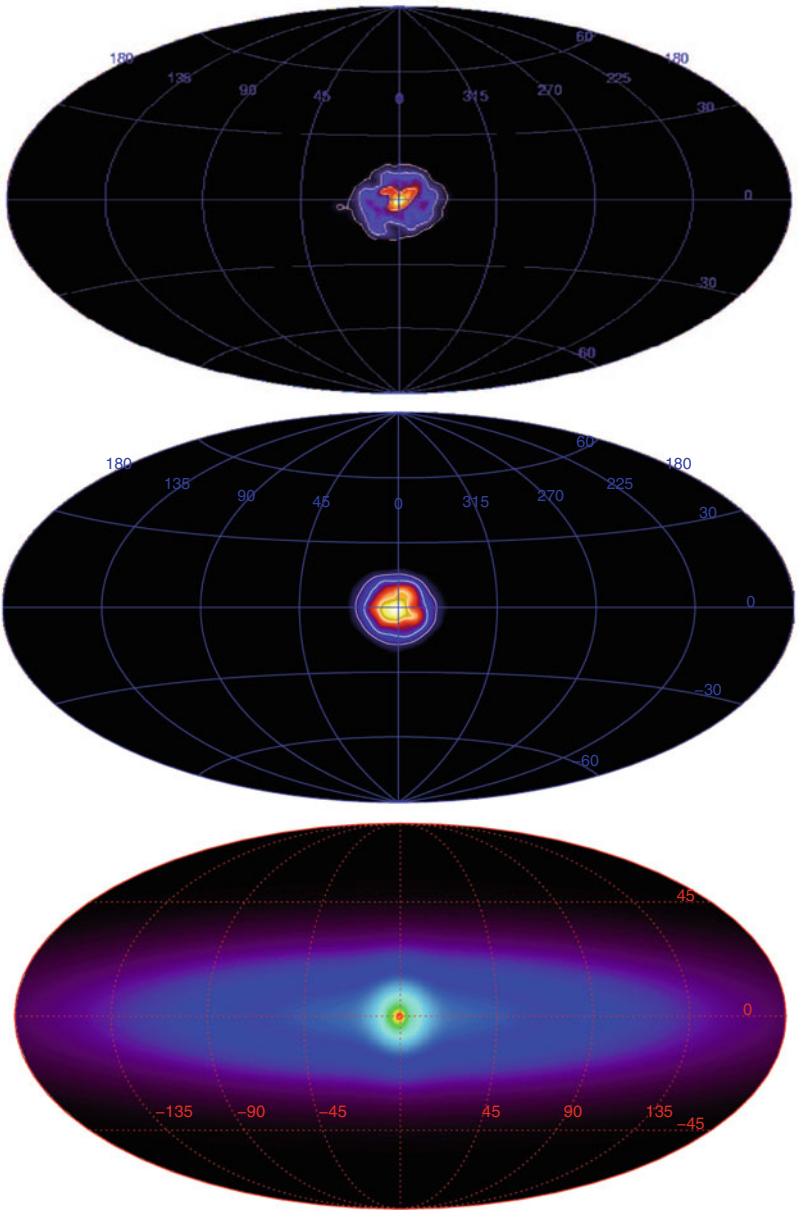

Fig. 7.31 Images of positron annihilation gamma rays as derived from INTEGRAL/SPI data. *Top:* First image from Richardson-Lucy deconvolution, the 511 keV line (Knödlseder et al. 2005). *Middle:* Image from Richardson-Lucy deconvolution, the positronium 3-photon continuum (Weidenspointner et al. 2006b). *Bottom:* Image from model fit optimisations, the 511 keV line (Siegert et al. 2016b; Skinner et al. 2014)

The detailed quantitative characterisation of the different components of 511 keV emission requires parameterising these in the form of (necessarily idealised) spatial emission models fitted to the data. Such decomposition is not unique, both the spheroid and the disk may have faint extensions contributing substantially to their total γ-ray emissivities. In the early years of INTEGRAL/SPI analyses, thin to moderately extended disk models had been tested. With more exposure, the disk emission became clear, and also why it had been difficult to detect it: In a parameter study from 13 years of observations, Siegert et al. (2016b) showed that the disk component appears to have a low surface brightness, although as a whole being as intense as the emission from the inner Galaxy. The bulge-to-disk flux ratio derived from these deeper observations now falls well below the values beyond 1 that stimulated the above discussions of exotic origins, and is determined as (0.58 ± 0.13) (Siegert et al. 2016b). The disk component of annihilation gamma rays seems quite extended, up to kpc in latitude. This suggests that positrons may fill a much larger volume than previously thought, and may annihilate as they leave the gaseous disk of the Galaxy towards the halo.

The bulge emission is best described by combining a narrow and a broad source region that can be described as a 2-dimensional Gaussian, with widths (FWHM, projected onto the sky) of 5–6° and 20°, respectively. The rather thick disk of vertical extent 25° (FWHM projected on the sky) also may not only be bright in the inner quadrants, as suggested by the large extent in latest model fits of almost 150° (FWHM) (Siegert et al. 2016b). But morphological modelling remains uncertain, even a very significant total-sky signal (see Fig. 7.30) becomes marginal as it is split up on the sky, in particular as the bulge region dominates so clearly in surface brightness.

There was considerable excitement about an apparent asymmetry of the emission with respect to the direction towards our Galaxy's centre. The flux asymmetry for fourth versus first galactic quadrant as reported by Weidenspointner et al. (2008) seemed like an invitation to look for positron sources with a similar asymmetric distribution in the Galaxy. Low-mass X-ray binaries appeared suggestive, although it remained unclear how those should emit large amounts of positrons. Their extreme variants, when the compact component would be a stellar-mass black hole, are called 'microquasars', and are known to eject plasma jets, as seen in radio emission. Although microquasars have been among the candidate sources, only few of those are identified in our Galaxy and appear throughout the disk; but from observational biases due to jet aspects, uncertainties are large. Currently, there is a consensus that the bright bulge component is not centred in the Galaxy, but rather offset by 1.2° towards the fourth quadrant. Although this is a conclusion that had first been suggested also by imaging deconvolution (Bouchet et al. 2010), and is different from an asymmetric disk component, this had stimulated ideas that the Galaxy altogether and including its candidate positron sources as possibly dominated by radioactivities was indeed not entirely symmetric nor centred at Galactic coordinates (0°,0°) (Higdon et al. 2009) (Fig. 7.32).

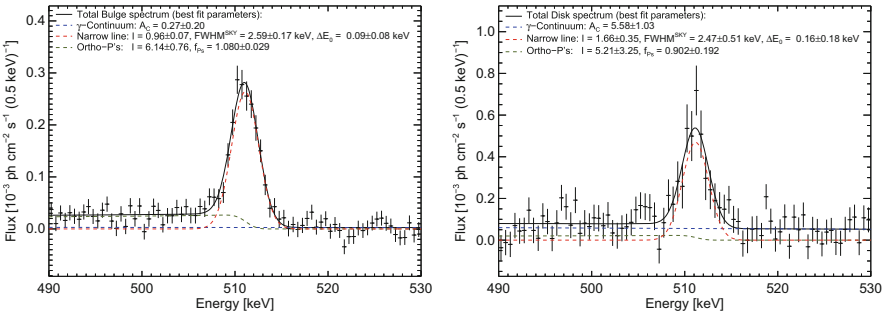

Fig. 7.32 Spectra of the annihilation emission from bulge (left) and disk (right) (Siegert et al. 2016b). The different annihilation conditions are indicated from the different intensities of the 3-photon continuum

7.5.2.2 Spectroscopy

The excellent spectral resolution of SPI allowed for the first time to study the spectrum of the 511 keV emission in great detail and for different regions (Figs. 7.32 and 7.33). The spectra of the Galactic spheroidal emission were analysed by Churazov et al. (2005) and Jean et al. (2006), based on the first year of SPI data. The line displays no significant overall spectral shift, i.e. it appears at the expected energy $E = 511\,\mathrm{keV}$ within 0.05 keV or less (Siegert et al. 2016b) and it is composed of two spectral components (assumed, to first order, to be represented by Gaussians): a narrow line with a width of FWHM $= 2 \pm 0.08\,\mathrm{keV}$ and a broad component with a width of FWHM $= 10 \pm 0.5\,\mathrm{keV}$ (Fig. 7.34 and Table 7.2). The width of the broad line is in agreement with the broadening expected from positronium annihilation via charge exchange with hydrogen atoms. The narrow line component contains $\sim 2/3$ of the total annihilation line flux while the broad one makes up the remaining $\sim 1/3$ of the flux. Table 7.2 summarises the results of the spectral analysis of the Galactic 511 keV emission after the first year of SPI data.

SPI also clearly detected the ortho-positronium continuum with an intensity that corresponds to a positronium fraction of $f_{Ps} = 100 \pm 10\%$ for bulge and for disk component (Siegert et al. 2016b) (see Eq. 7.7). This confirms earlier measurements obtained by SPI and other instruments for the bulge (Jean et al. 2006; Kinzer et al. 1996; Harris et al. 1998, (97±2 %) for SPI, for OSSE (97±3 %) and for TGRS (94± 4 %)). This suggests that practically all annihilations occur through the intermediate step of the positronium atom (Fig. 7.33).

The shape of the annihilation line and the relative intensity of the ortho-positronium continuum are closely related to the physical conditions such as density, temperature and chemical abundances of the interstellar medium in which positrons annihilate. Figure 7.34 shows that the 511 keV line is rather narrow, with some broadening indicated in the wings. The results of the spectral analysis of the bulge emission suggest that positrons annihilate mostly in a warm medium (T$\sim 10^4$ K)

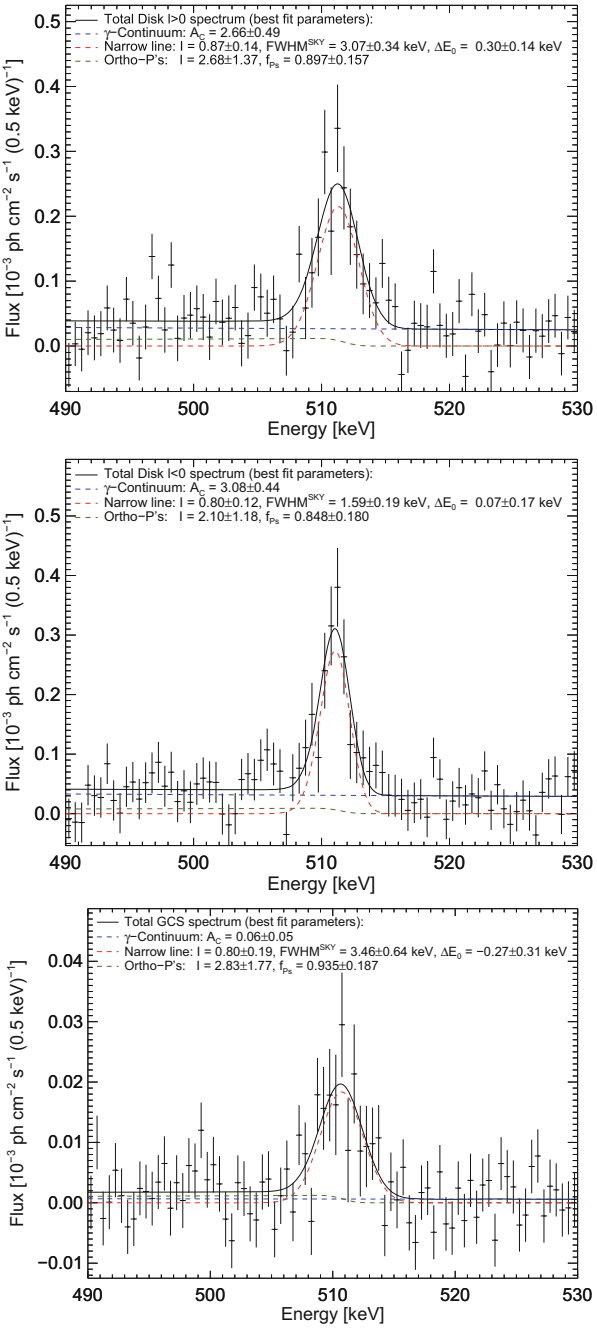

Fig. 7.33 Spectra of the different aspects of annihilation spectroscopy. The left and right (first and fourth) quadrants of the Galaxy show very similar spectra, although intensity differs slightly. The line for the point source located in the vicinity of Sgr A* may have a slightly broader line (from Siegert et al. 2016b)

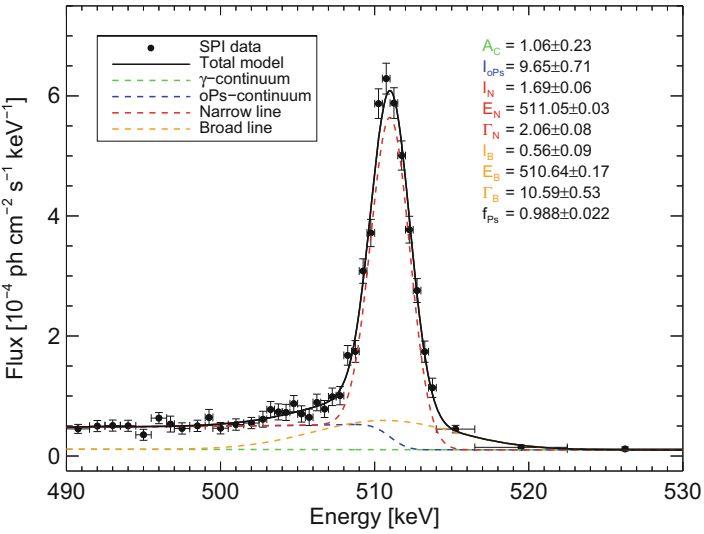

Fig. 7.34 Best fit of the spectrum measured by SPI using different components of the annihilation spectrum from the ISM and the Galactic continuum (Siegert et al. 2016b)

Table 7.2 Results of spectral analysis of Galactic 511 keV emission from the entire sky region exposed by INTEGRAL after 15 years

Parameter	Measured value
E_n (keV)	511.05 ± 0.03
I_n (10^{-3} s^{-1} cm^{-2})	1.69 ± 0.06
Γ_n (keV)	2.06 ± 0.08
I_b (10^{-3} s^{-1} cm^{-2})	0.56 ± 0.09
Γ_b (keV)	10.59 ± 0.53
$I_{3\gamma}$ (10^{-3} s^{-1} cm^{-2})	9.65 ± 0.71
A_c (10^{-6} s^{-1} cm^{-2} keV^{-1})	1.06 ± 0.23

Identified components are narrow and broad lines at 511 keV, and underlying continuum from ortho-positronium and Galactic diffuse emission. E_n the centroid of the narrow line, $I_{n/b}$ and $\Gamma_{n/b}$ are the flux and width (FWHM) of the narrow and broad lines, respectively. $I_{3\gamma}$ is the flux of the ortho-positronium continuum and A_c is the amplitude of the Galactic continuum at 511 keV (From Siegert et al. 2016b)

with a non-negligible ionised fraction: >1% (according to Churazov et al. 2005), and up to 50% (according to Jean et al. 2006). The latter adopted spectral models appropriate for e^+ annihilation in the different ISM phases, and adjusted the phase fractions f_i (with i = {molecular, cold, warm neutral, warm ionised, hot}) so as to obtain the best fit to the spectral details measured by SPI. Since the bulge is dominated by hot gas (see Chap. 11), one may ask how positrons end up annihilating in sub-dominant (by volume) phases of the ISM. This immediately

suggests that positron propagation may be crucial in understanding the 511 keV emission. Furthermore, the small width of the 511 keV line, along with the high positronium fraction, both suggest that positrons annihilate at very low energies (<10 keV).

7.5.2.3 Relevant Observations at MeV Energies

The observed γ-ray emission from the decay of ^{26}Al in the Galaxy (see Sect. 7.2) implies that ^{26}Al provides an important contribution to the Galactic amount of positrons. The detected flux translates into a decay rate of ^{26}Al which depends slightly on the adopted 3D distribution of ^{26}Al in the Galaxy. The most recent analysis of SPI data results in a rate of $\dot{N}_{26} = 4.3\ 10^{42}\ \mathrm{s}^{-1}$ or $2.7\,\mathrm{M}_{\odot}$/Myr (Wang et al. 2009). Assuming a steady state, i.e. equality between production and decay rates, this is also the present production rate of ^{26}Al in the Galaxy (Sect. 7.2).

Being predominantly a β^+-emitter (with a branching ratio of $f_{e^+,26} = 82\%$, see Fig. 1.3 in Chap. 1) ^{26}Al is itself a source of positrons. The corresponding Galactic e^+ production rate is $\dot{N}_{e^+,26} = f_{e^+,26}\dot{N}_{26} \sim 3.5 \times 10^{42}\ \mathrm{s}^{-1}$. This constitutes a significant contribution to the total Galactic e^+ production rate: 17% of the total e^+ annihilation rate and almost half of the (thick) disk in the baseline model, or 10% of the total and 70% of the thin disk in the Halo+thin disk model (Weidenspointner et al. 2006a). We shall see that positrons from this and other β^+-decaying nuclei could plausibly explain the disk emissivity, while the bulge emissivity remains a challenge for our understanding.

Important complementary information on the energies of the annihilating positrons is obtained from the analysis of the observed continuum emission at somewhat higher energies (above 511 keV and into the MeV region) The reason is that positrons in several e^+ candidate sources are typically emitted at relativistic energies, in some cases even far above 1 MeV. They behave essentially like relativistic electrons of cosmic rays, producing bremsstrahlung and inverse-Compton emission while slowing down to thermal energies (eV) of the interstellar medium, where they eventually annihilate. But positrons may also annihilate *in flight* while still having relativistic energies, giving rise to a unique γ-ray continuum signature at energies above 511 keV (as the centre-of-mass energy is transferred to annihilation photons, systematically increasing and broadening their typical energies in observer's frame). The shape and amplitude of this γ-ray emission depend on the injection spectrum of positrons and the corresponding total *in-flight* annihilation rate. For positrons injected at low energies (of the order of ~MeV, such as those released by radioactivity), the amplitude of the in-flight annihilation continuum above 1 MeV is quite small, while for sources injecting positrons at much higher energy (such as cosmic-ray positrons from pion decay), the annihilation γ-ray spectrum would extend up to GeV energies and include a considerable γ-ray flux. The high energy γ-ray continuum above 1 MeV therefore constrains the energy and the annihilation rate of relativistic positrons, when all other sources of such high energy emission are properly accounted for.

Diffuse Galactic continuum emission has been well-measured at least in the inner part of the Galactic disk (longitudes $-30° < l < 30°$) in the hard-X-ray through γ-ray regime by INTEGRAL, OSSE, COMPTEL, and EGRET Bouchet et al. (2008). It is mostly due to various interactions of cosmic rays propagating with interstellar gas, which also produce secondary positrons (Strong et al. 2007). In view of the uncertainties still affecting the propagation parameters, soe (albeit very little) room is still left for a contribution of in-flight e^+ annihilation to the MeV continuum.

The constraints to the injection energy of positrons have been pointed out a long time ago by Agaronyan and Atoyan (1981). They showed that the positrons which are responsible for the Galactic 511 keV line cannot be produced in a steady state by the decay of the π^+ created in proton-proton collisions (between cosmic rays and the ISM) or else the in-flight annihilation emission should have been detected. A similar argument was used by Beacom and Yüksel (2006) and Sizun et al. (2006) to constrain the mass of the candidate dark matter particle which could be the source of positrons in the Galactic spheroid. If such particles produce positrons (in their decay or annihilation) at a rate which corresponds to the observed 511 keV emission, then their mass should be less than a few MeV, otherwise the kinetic energy of the created positrons would have been sufficiently high to produce a measurable γ-ray continuum emission in the 1–30 MeV range (Fig. 7.35). The same argument allows one to constrain the initial kinetic energy of positrons and thus to eliminate several classes of candidate sources, like e.g. pulsars, ms pulsars, magnetars, cosmic rays etc., as major positron producers, due to their high positron injection energies.

An interesting opportunity occurred in 2015 when a nearby microquasar, called V404 Cygni, went into a spectacular outburst, and made it the brightest source on the gamma ray sky for about 2 weeks, at hard-X-ray brightness exceeding the Crab

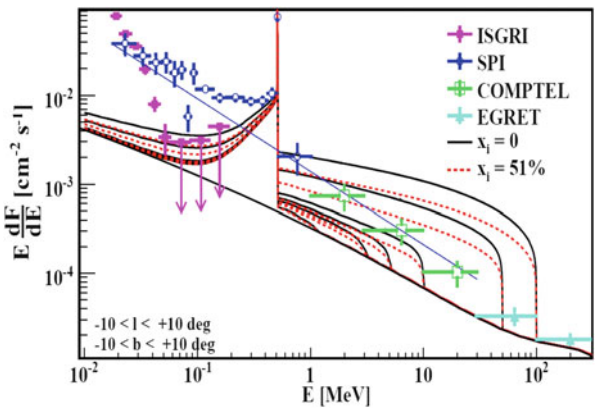

Fig. 7.35 Spectrum of the inner Galaxy as measured by various instruments, compared to various theoretical estimates made under the assumption that positrons are injected at high energy: the four pairs of curves result from positrons injected at 100, 30, 10 and 3 MeV (from top to bottom) and correspond to positrons propagating in neutral (*solid*) or 50% ionised (*dotted*) media (*from* Sizun et al. 2006). This constrains the injected positron energy (or, equivalently, the mass of decaying/annihilating dark matter particles) to a few MeV

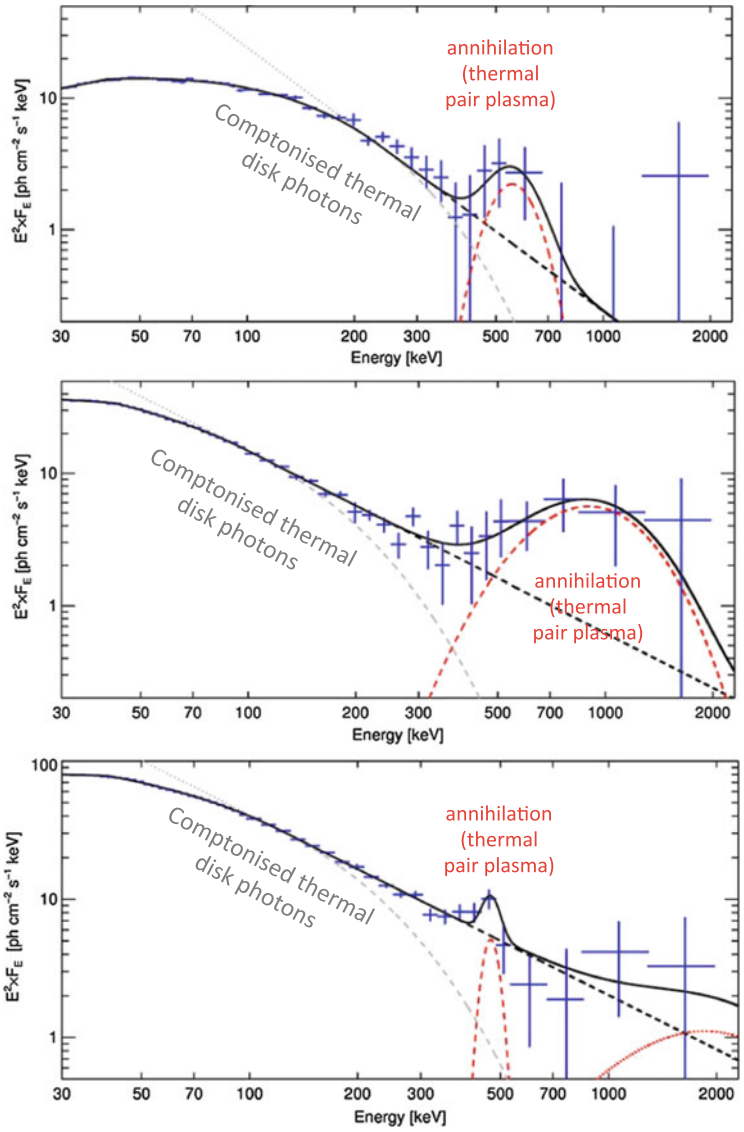

Fig. 7.36 Signature from pair plasma positron annihilation, as observed during the flaring episode June 2015 of microquasar V404 Cyg (Siegert et al. 2016a)

by a factor of 40. INTEGRAL observations were fortunate to catch transient spectral features at high energy, in addition to the bright hard X-ray emission that had been expected from such a flaring episode. After some study, the high-energy spectral features shown in Fig. 7.36 plausibly and best associated with positron annihilation of a relativistic plasma (Siegert et al. 2016a).

7.5.3 Assessment of Candidate Positron Sources

Each of the candidate positron sources should be critically discussed the light of the observational constraints in all different aspects as presented in the previous section. Here we use three main criteria: (1) the total e^+ annihilation rate ($\sim 5 \times 10^{43}\,s^{-1}$), (2) the typical energy of the injected positrons, or the equivalent mass of annihilating DM particles ($<$3–7 MeV) and (perhaps, most significantly) (3) the morphology of the 511 keV emission (parameterised by a bulge/disk ratio B/D$\sim$1, higher than in all other wavelengths.[6]

Positron Production Rate Assuming a steady state regime, the e^+ annihilation rate has to be equal to the *average* e^+*production rate during the lifetime of* e^+*in the ISM*. The only source definitely known to provide substantial amounts of e^+ at a well constrained rate is the radioactive decay of ^{26}Al: $0.4 \times 10^{43}\,e^+\,s^{-1}$. The decay of ^{44}Ti probably provides another $0.3 \times 10^{43}\,e^+\,s^{-1}$. GCRs probably provide $0.1 \times 10^{43}\,e^+\,s^{-1}$. Nova models (as constrained against several observables such as ejecta abundances, velocities etc.) may provide a e^+ yield from ^{22}Na decay not be much below the reported value of $10^{41}\,e^+\,s^{-1}$. The e^+ of all other candidate sources is entirely speculative at present. The values reported in Table 7.3 for the other candidate positron sources should be considered as optimistic rather than typical ones. Indeed, no useful observational constraints exist up to now on the e^+ yields of hypernovae/GRBs, pulsars, ms pulsars, magnetars, microquasars, the SMBH at the Galactic center, or dark matter annihilation. SNIa remain an intriguing, but serious candidate, with a potential Galactic yield of $2 \times 10^{43}\,e^+\,s^{-1}$ (assuming an escape fraction of 4%).

Positron Energy Radioactive decay produces positrons of $E \leq 1$ MeV, naturally fulfilling the observational constraint on continuum γ rays from in flight annihilation. The same applies to pair creation through $\gamma - \gamma$ collisions in the inner accretion disk or at the base of the jets of LMXRBs, microquasars and the SMBH at the Galactic centre. Conversely, pair creation involving very high energy photons, as in e.g. pulsars or magnetars, will produce positrons of too high energy. The same holds for energetic p-p collisions in Galactic cosmic rays or in the baryonic jets of LMXRBs, microquasars and the Galactic MBH. Those processes produce e^+ of $>$30 MeV, thus may be discarded as major e^+ sources in the Milky Way. Also, that same constraint limits the mass of putative decaying or annihilating DM particles to $<$10 MeV, while it does not constrain the mass of de-exciting DM particles.

Source Morphology None of the e^+ sources reproduces the large bulge-to-disk ratio$\sim$1 ratio inferred from SPI data. The best-established e^+ sources, β^+-decay from ^{26}Al and ^{44}Ti produced in massive stars, yield a bulge-to-disk ratio$\leq$0.2, as derived from the observed distribution of the 1.8 MeV ^{26}Al line (Fig. 7.37). Such

[6]We do no include in this list of constraints the intriguing disk asymmetry reported byWeidenspointner et al. (2008), since it has not been subsequently confirmed, e.g. Bouchet et al. (2008).

Table 7.3 Properties of candidate positron sources in the Milky Way (adapted from Prantzos et al. 2011)

Source	Process	E(e^+)[a] (MeV)	e^+ rate[b] $\dot{N}_{e^+}(10^{43}\ s^{-1})$	Bulge[c]/Disk[c] B/D	Comments
Massive stars: ^{26}Al	β^+	∼1	0.4	<0.2	$\dot{N}$, B/D: Observationally inferred
Supernovae: ^{44}Ti	β^+	∼1	0.3	<0.2	$\dot{N}$: Robust estimate
SNIa: ^{56}Ni	β^+	∼1	*2*	<0.5	Assuming $f_{e^+,esc} = 0.04$
SN91bg-like: ^{44}Ti	β^+	1	4	∼ 0.5	Assuming 0.03 $M_\odot$ of ^{44}Ti per SN
Novae	β^+	∼1	*0.02*	<0.5	Insufficient e^+ production
Hypern./GRB: ^{56}Ni	β^+	∼1	?	<0.2	Improbable in inner MW
Cosmic rays	p-p	∼30	0.1	<0.2	Too high e^+ energy
LMXRBs	$\gamma-\gamma$	∼1	*2*	<0.5	Assuming L_{e^+} ∼0.01 $L_{obs,X}$
Microquasars	$\gamma-\gamma$	∼ 1	*1*	<0.5	e^+ load of jets uncertain
Pulsars	$\gamma-\gamma$	>30	*0.5*	<0.2	Too high e^+ energy
ms pulsars	$\gamma-\gamma$	>30	*0.15*	<0.5	Too high e^+ energy
Magnetars	$\gamma-\gamma$	>30	*0.16*	<0.2	Too high e^+ energy
Central black hole	p-p $\gamma-\gamma$	High 1	? ?		 Requires e^+ diffusion to ∼1 kpc
Dark matter	Annih.	1 (?)	?		Light scalar particle, cuspy DM profile
	Deexcit.	1	?		Only cuspy DM profiles allowed
	Decay	1	?		Ruled out for all DM profiles
Observational constraints		<7	2	1.4	

[a]Typical values are given

[b]e^+ rates: in roman: observationally deduced or reasonable estimates; in italic: speculative (and rather closer to upper limits)

[c]Sources are simply classified as belonging to either young ($B/D < 0.2$) or old(<0.5) stellar populations

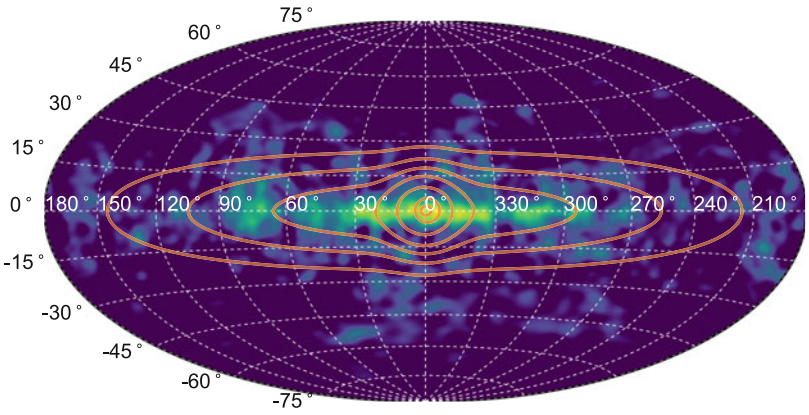

Fig. 7.37 Map of Galactic 511 keV emission detected with SPI/INTEGRAL (contours) superimposed onto the Galactic emission map at 1.8 MeV from ^{26}Al decay (color) (Siegert et al. 2016c)

a distribution reflects essentially the corresponding present star formation rates in the bulge and the disk. On the other hand, an older stellar population, reflecting the time-integrated rather than the present-day star formation, is expected to have a larger bulge/disk ratio (due to the inside-out formation of the Milky Way). Binaries involving low mass stars, such as SNIa, novae and LMXRBs, are expected to have a steeper longitude profile, with a maximal bulge-to-disk ratio$\leq$0.5 (see Prantzos et al. 2011, for a review of the expected profiles of the various candidate sources in the Galaxy).

The morphology of the observed 511 keV emission provides also some interesting constraints in the case of dark matter particles as positron sources (under the assumption of negligible e^+ propagation) (as analysed in Ascasibar et al. 2006): (1) Particle candidates with velocity dependent cross section are excluded as the main source of 511 keV emission, (2) Decaying dark matter cannot be the main source of low energy positrons, because the resulting flux profile is too flat, compared to SPI data. Notice that this latter feature is a generic property of all models involving decaying particles, where the positron production (and annihilation) rate is proportional to the DM density profile: even *cuspy* profiles, such as the *Navarro-Frenk-White* profile do not provide a γ-ray flux profile sufficiently peaked towards the inner Galaxy. Annihilating or de-exciting DM produces positrons at a rate proportional to the square of the DM density profile and leads to a much more peaked γ-ray profile. Light scalar annihilating particles remain a possible candidate, provided the dark matter halo is at least as cuspy as the Navarro-Frenk-White profile with $\gamma \sim 1$; however, astrophysical evidence favors flatter DM halo profiles.

A stacking analysis for 39 dwarf spheroidal galaxies nearby (Siegert et al. 2016c), finally, yields a strong argument against dark matter origin of any kind being the dominant source of Galactic positrons. Those galaxies are expected to be *dominated* in their mass by dark matter, as apposed to relatively little baryonic matter. The

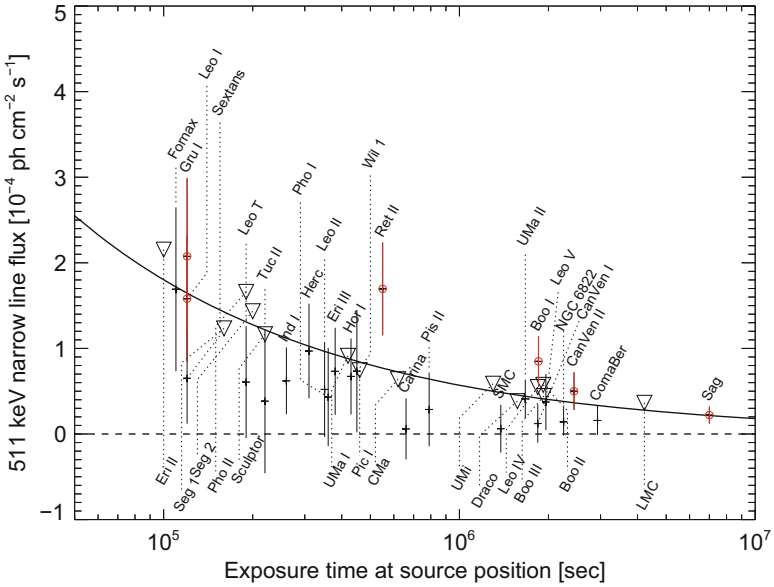

Fig. 7.38 Limits of positron annihilation signal in the 511 keV line from 39 nearby dwarf spheroidal galaxies. The continuous line shows the expected trend if dark matter and distance would contribute to a small signal contribution (Siegert et al. 2016c)

stacking analysis does not find a significant positron annihilation signal, with the exception of one galaxy that also is peculiar for other reasons, Ret II. But the limits obtained for all other dSph galaxies were expected to correlate at least somewhat with their distance and dark matter content, while even an opposite trend was found (see Fig. 7.38). Scaling with matter content, the stacking limit is incompatible with a dark-matter dominated positron annihilation luminosity for the Galaxy, and hence argues that dark matter contributions, if existing, must be small.

The main features of all these candidate e^+ sources are summarised in Table 7.3. The e^+ production rates of all those sources are extremely uncertain (except those of ^{26}Al, ^{44}Ti and GCRs) and the values listed above should be considered as optimistic rather than typical ones. Only in the case of novae may the estimated production value be used to eliminate those sources as important e^+ producers. Source morphology and high energy of produced positrons appear to exclude pulsars, magnetars and Galactic cosmic rays as major contributors to the observed 511 keV emission from the bulge. Source morphology alone would exclude CCSN, hypernovae and GRBs. The high energy of positrons disfavours ms pulsars, as well as p-p collisions from any source (micro-quasars, LMXRB jets, the central SMBH).

A rare sub-class of SNIa, named after their 'prototype' event, SN1991bg, has been recently suggested as the main source of Galactic positrons (Crocker et al. 2017). That class represents ∼15% of all SNIa and they are several times less luminous than the average SNIa. Theoretical ? and still uncertain ? models find

that their explosion may produce up to a few $0.01\,M_\odot$ of ^{44}Ti, providing enough positrons to explain the observed 511 keV emission *and* its Galactic distribution: indeed, assuming that the Delay Time Distribution (DTD) of those objects is different than the one of standard SNIa (peaking several Gy after the formation of the progenitor stars, in contrast to the DTD $\propto time^{-1}$ of SNIa), one finds that the early enhanced star formation in the bulge may produce today few SNIa but enough SNIbg to provide a large B/D ratio. That scenario might also explain the paucity of Galactic sources of ^{44}Ti: that radionuclide is the progenitor of stable ^{44}Ca and, if the source of the solar abundance of the latter is CCSN of low ^{44}Ti yield (as usually assumed), one should expect several SN remnants glowing in the ^{44}Ti γ-ray lines to be seen by INTEGRAL, whereas only Cas A is currently detected.

The possibility of explaining at one stroke both the Galactic 511 keV emission and the paucity of ^{44}Ti sources makes the idea of Crocker et al. (2017) appealing. However, two key ingredients of the model, namely the ^{44}Ti yields and the evolution of the rate of SNIbg-type supernovae should be substantiated by further studies (including 3D models of supernova nucleosynthesis) before concluding.

If positrons annihilate near their sources, one has to conclude that (1) either poorly understood class of sources (such as SNIbg-like objects) dominates e^+ production, or that (2) positrons are produced by a combination of the sources of Table 7.3, e.g. (a) ^{26}Al +^{44}Ti for the disk and dark matter for the bulge, or (b) ^{26}Al +^{44}Ti + LMXRBs(or microquasars) for the disk *and* the bulge plus a contribution from the central SMBH for the inner bulge, or (c) some other combination.

In order to alleviate the morphology problem, it has been suggested that positron transport might help. Prantzos (2006b) suggested that *if* the magnetic field of the Milky Way halo has a strong poloidal component, then some positrons escaping the disk may be channeled into the bulge and annihilate there, enhancing the bulge/disk e^+ annihilation ratio. In that case, positrons from SNIa may suffice to explain *quantitatively both* the total observed e^+ annihilation rate ($\sim 2\times10^{43}\,e^+\,s^{-1}$) *and* the corresponding bulge-to-disk ratio, *provided* that the escaping e^+ fraction from SNIa is ~3–4%. However, observations of external spirals suggest rather an X-shaped halo field in which case it would be difficult for disk positrons to find their way into the bulge. Still, the issue is of considerable interest to urge a better assessment of the poorly known global configuration of the Galactic magnetic field.

In the same framework of "outside-in" positron transport, Higdon et al. (2009) suggested that positron propagation through the Galaxy may be all that is needed for understanding not only the spatial morphology of the 511 keV emission, but also its spectral properties. They assumed that radioactivity (from ^{26}Al, ^{44}Ti and, mostly, from ^{56}Co) is the sole e^+ source in the Galaxy and they considered (1) a fairly detailed description of the various phases of the ISM and (2) a particular phenomenological model of collisionless scattering of MeV positrons by turbulent fluctuations of the ISM, allowing to transport positrons from the inner 3 kpc into the bulge region.

The aforementioned ideas were put in test through detailed numerical simulations of positron transport, either with Monte Carlo methods (Alexis et al. 2014) or with

cosmic ray propagation codes such as GALPROP (Martin et al. 2012). In both cases, it was found that although positrons may travel up to a few kpc from their birth place, the bulk of them is annihilated rather close to their birth places, making it difficult to reproduce the observed high B/D ratio; re-acceleration of positrons, not considered in those studies, might help in that respect.

Finally, the idea of an "inside-out" propagation of positrons was explored, in order to investigate the possibility of positrons produced by the activity of a central Galactic source (the super-massive black hole of SgA) and diffusing throughout the bulge. The spectral signature of the 511 keV emission, suggesting that positrons annihilate mostly in the warm ISM, provides a powerful constraint in that case. The Monte Carlo study of Jean et al. (2009) investigated collisional transport in the ISM of the bulge and found the diffusion length of positrons to exceed typical size scales of the warm ISM, where they are thought to annihilate. On the other hand, Panther et al. (2018) investigated the transport of positrons coupled to the turbulent, magnetized plasma outflowing from the inner Galaxy (as evidenced from infra-red and γ-ray observations). They found that although positrons may indeed be advected to scales of $\sim$2 kpc and fill the bulge, they would annihilate mostly in a hot, ionised plasma, while observations point to a warm ISM. That study concerns a steady plasma and positron outflow, while Alexis et al. (2014) argued that a burst of activity in the galactic center 1–10 My ago could make positrons annihilate in a warm environment, in agreement with observations.

In summary, more than 40 years after its discovery, the origin of positrons annihilating in the Galaxy remains unknown. Progress in the field will require advances in several directions:

1. *Observations of 511 keV emission*: what is the true spatial distribution of the emission? how far the spheroid and disk extend? are there yet undetected regions of low surface brightness? is the disk emission asymmetric indeed? how do the 1.8 MeV and 511 keV disk emissions compare to each other? A much deeper exposure of the Galaxy and a better understanding of the backgrounds will be required to tackle those issues. Even if INTEGRAL's mission is extended into 2020ies, it appears questionable that it will be able to provide the answers; even worse, no other mission in this energy range is scheduled at present.
2. *Physics of e^+ sources*: what is the e^+ escaping fraction in SNIa ? what is the SNIa rate in the inner (star forming) and in the outer (inactive) bulge? what are the e^+ yields, activity timescales, and spatial distribution in the inner bulge of LMXRBs or microquasars? how can the past level of activity of the central massive black hole be reliably monitored?
3. *Positron propagation:* what is the large scale configuration of the Galactic magnetic field? what are the properties of interstellar plasma turbulence and how they affect the positron transport? what are the dominant propagation modes of positrons and what the role of re-acceleration might be?

The many faces of the Galactic 511 keV emission make this problem one of the most intriguing problems in high energy astrophysics today and for the years to come.

References

Agaronyan FA, Atoyan AM (1981) Sov Astron Lett 7:395
Alexis A, Jean P, Martin P, Ferrière K (2014) Astron Astrophys 564:A108
Ascasibar Y, Jean P, Bœhm C, Knödlseder J (2006) Mon Not R Astron Soc 368:1695
Asplund M, Grevesse N, Sauval AJ, Scott P (2009) Annu Rev Astron Astrophys 47:481
Bally J (2008) Overview of the orion complex. In: Reipurth B (ed) ASP monograph publications. Handbook of star forming regions, Valencia, vol I. ASP, p 459
Beacom JF, Yüksel H (2006) Phys Rev Lett 97:071102
Binns WR, Wiedenbeck ME, Arnould M et al (2005) Astrophys J 634:351
Binns WR, Israel MH, Christian ER et al (2016) Science 352:677
Blair WP, Sankrit R, Raymond JC (2005) Astron J 129:2268
Bouchet L, Mandrou P, Roques J-P et al (1991) Astrophys J 383:L45+
Bouchet L, Jourdain E, Roques J-P et al (2008) Astrophys J 679:1315
Bouchet L, Roques JP, Jourdain E (2010) Astrophys J 720:1772
Bouchet L, Jourdain E, Roques J-P (2015) Astrophys J 801:142
Breitschwerdt D, de Avillez MA (2006) Astron Astrophys 452:L1
Breitschwerdt D, Freyberg MJ, Truemper J (eds) (1998) Lecture notes in physics. The local bubble and beyond, vol 506. Springer, Berlin
Breitschwerdt D, Feige J, Schulreich MM et al (2016) Nature 532:73
Brown AGA, de Geus EJ, de Zeeuw PT (1994) Astron Astrophys 289:101
Burrows DN, Singh KP, Nousek JA, Garmire GP, Good J (1993) Astrophys J 406:97
Bussard RW, Ramaty R, Drachman RJ (1979) Astrophys J 228:928
Bykov AM, Treumann RA (2011) Astron Astrophys Rev 19:42
Cash W, Charles P, Bowyer S et al (1980) Astrophys J 238:L71
Casse M, Paul JA (1982) Astrophys J 258:860
Chatterjee S, Cordes JM, Vlemmings WHT et al (2004) Astrophys J 604:339
Chen W, Diehl R, Gehrels N et al (1997) In: Winkler C, Courvoisier TJL, Durouchoux P (eds) The transparent universe. ESA special publication, vol 382, pp 105–+
Cheng LX, Leventhal M, Smith DM (1997) Astrophys J 481:L43+
Chieffi A, Limongi M (2013) Astrophys J 764:21
Chupp EL, Forrest DJ, Higbie PR et al (1973) Nature 241:333
Churazov E, Sunyaev R, Sazonov S, Revnivtsev M, Varshalovich D (2005) Mon Not R Astron Soc 357:1377+
Clayton DD, Nittler LR (2004) Annu Rev Astron Astrophys 42:39
Comerón F, Pasquali A, Figueras F, Torra J (2008) Astron Astrophys 486:453
Crocker RM, Ruiter AJ, Seitenzahl IR et al (2017) Nat Astron 1:0135
Dame TM, Hartmann D, Thaddeus P (2001) Astrophys J 547:792
de Geus EJ (1992) Astron Astrophys 262:258
de Geus EJ, de Zeeuw PT, Lub J (1989) Astron Astrophys 216:44
de Zeeuw PT, Hoogerwerf R, de Bruijne JHJ, Brown AGA, Blaauw A (1999) Astron J 117:354
Diehl R (2002) New Astron Rev 46:547
Diehl R (2013) Astron Rev 8:4
Diehl R (2016) J Phys Conf Ser 703:012001
Diehl R, Dupraz C, Bennett K et al (1995) Astron Astrophys 298:445
Diehl R, Kretschmer K, Plüschke S, Cerviño M, Hartmann DH (2003) In: van der Hucht K, Herrero A, Esteban C (eds) IAU symposium. A massive star odyssey: from main sequence to supernova, vol 212, pp 706–+
Diehl R, Halloin H, Kretschmer K et al (2006a) Nature 439:45
Diehl R, Halloin H, Kretschmer K et al (2006b) Astron Astrophys 449:1025
Diehl R, Lang MG, Martin P et al (2010) Astron Astrophys 522:A51+
Diehl R, Siegert T, Greiner J, Krause M, Kretschmer K, Lang M, Pleintinger M, Strong AW, Weinberger C, Zhang X (2018) Astron Astrophys 611:A12. https://doi.org/10.1051/0004-6361/201731815

Ekström S, Georgy C, Eggenberger P et al (2012) Astron Astrophys 537:A146
Ellison DC, Drury LO, Meyer J (1997) Astrophys J 487:197
Endt PM (1990) Nucl Phys A 521:1
Fernández D, Figueras F, Torra J (2008) Astron Astrophys 480:735
Fierlinger KM, Burkert A, Ntormousi E et al. (2016) Mon Not R Astron Soc 456:710
Fimiani L, Cook DL, Faestermann T et al. (2016) Phys Rev Lett 116:151104
Fitoussi C, Raisbeck GM, Knie K et al. (2008) Phys Rev Lett 101:121101
Forestini M, Charbonnel C (1997) Astron Astrophys Suppl Ser 123:241
Frisch PC (1995) Space Sci Rev 72:499
Fuchs B, Breitschwerdt D, de Avillez MA, Dettbarn C (2009) Space Sci Rev 143:437
Gaczkowski B, Preibisch T, Stanke T et al. (2015) Astron Astrophys 584:A36
Gaczkowski B, Roccatagliata V, Flaischlen S et al. (2017) Astron Astrophys 608:A102
Gehrz RD, Truran JW, Williams RE, Starrfield S (1998) Publ Astron Soc Pac 110:3
Genzel R, Stutzki J (1989) Annu Rev Astron Astrophys 27:41
Goswami A, Prantzos N (2000) Bull Astron Soc India 28:305
Groopman E, Zinner E, Amari S et al (2015) Astrophys J 809:31
Harris MJ, Teegarden BJ, Cline TL et al (1998) Astrophys J 501:L55+
Harris MJ, Knödlseder J, Jean P et al (2005) Astron Astrophys 433:L49
Heftrich T, Bichler M, Dressler R et al (2015) Phys Rev C 92:015806
Higdon JC, Lingenfelter RE, Ramaty R (1998) Astrophys J 509:L33
Higdon JC, Lingenfelter RE, Rothschild RE (2009) Astrophys J 698:350
Hoogerwerf R, de Bruijne JHJ, de Zeeuw PT (2000) Astrophys J 544:L133
Iliadis C, Champagne A, Chieffi A, Limongi M (2011) Astrophys J Suppl 193:16
Jean P, Knödlseder J, Gillard W et al (2006) Astron Astrophys 445:579
Jean P, Gillard W, Marcowith A, Ferrière K (2009) Astron Astrophys 508:1099
Johnson WN, Harnden FR, Haymes RC (1972) Astrophys J 172:L1+
Jones FC, Lukasiak A, Ptuskin VS, Webber WR (2001) Adv Space Res 27:737
Jose J, Hernanz M (1998) Astrophys J 494:680
Kachelrieß M, Neronov A, Semikoz DV (2015) Phys Rev Lett 115:181103
Karakas AI, Lattanzio JC (2014) Publ Astron Soc Aust 31:e030
Kinzer RL, Purcell WR, Johnson WN et al (1996) Astron Astrophys Suppl Ser 120:C317+
Knie K, Korschinek G, Faestermann T et al (2004) Phys Rev Lett 93:171103
Knödlseder J, Dixon D, Bennett K et al (1999) Astron Astrophys 345:813
Knödlseder J, Cerviño M, Le Duigou J-M et al (2002) Astron Astrophys 390:945
Knödlseder J, Jean P, Lonjou V et al (2005) Astron Astrophys 441:513
Korschinek G, Kutschera W (2015) Nucl Phys A 944:190
Krause M, Fierlinger K, Diehl R et al (2013) Astron Astrophys 550:A49
Krause M, Diehl R, Böhringer H, Freyberg M, Lubos D (2014) Astron Astrophys 566:A94
Krause MGH, Diehl R, Bagetakos Y et al (2015) Astron Astrophys 578:A113
Krause M et al. (2018) Astron Astrophys (in press)
Kretschmer K, Diehl R, Krause M et al (2013) Astron Astrophys 559:A99
Kuffmeier M, Frostholm Mogensen T, Haugbølle T, Bizzarro M, Nordlund Å (2016) Astrophys J 826:22
Kulsrud RM (2005) Plasma physics for astrophysics. Princeton University Press, Princeton
Kutschera W (2013) In: European physical journal web of conferences, vol 63, pp 03001
Lallement R (2007) Space Sci Rev 130:341
Lee T, Papanastassiou DA, Wasserburg GJ (1976) Bull Am Astron Soc 8:457
Leventhal M, MacCallum CJ, Stang PD (1978) Astrophys J 225:11+
Limongi M, Chieffi A (2006a) New Astron Rev 50:474
Limongi M, Chieffi A (2006b) Astrophys J 647:483
Li KA, Lam YH, Qi C, Tang XD, Zhang NT (2016) Phys Rev C 94(6):065807. https://doi.org/10.1103/PhysRevC.94.065807
Lingenfelter RE, Ramaty R (1978) Phys Today 31:40
Lozinskaya TA, Pravdikova VV, Finoguenov AV (2002) Astron Lett 28:223

Ludwig P, Bishop S, Egli R et al (2016) Proc Natl Acad Sci 113:9232
MacPherson GJ, Davis AM, Zinner EK (1995) Meteoritics 30:365
MacPherson GJ, Bullock ES, Janney PE et al (2010) Astrophys J 711:L117
Mahoney WA, Ling JC, Wheaton WA, Jacobson AS (1984) Astrophys J 286:578
Maíz-Apellániz J (2004) In: Alfaro EJ, Pérez E, Franco J (eds) How does the galaxy work?. Astrophysics and space science library, vol 315, pp 231
Martin P, Knödlseder J, Diehl R, Meynet G (2009) Astron Astrophys 506:703
Martin P, Knödlseder J, Meynet G, Diehl R (2010) Astron Astrophys 511:A86+
Martin P, Strong AW, Jean P, Alexis A, Diehl R (2012) Astron Astrophys 543:A3
Mewaldt RA, Yanasak NE, Wiedenbeck ME et al (2001) Space Sci Rev 99:27
Meyer J (1985) Astrophys J Suppl 57:151
Meyer J, Drury LO, Ellison DC (1997) Astrophys J 487:182
Meynet G, Arnould M, Prantzos N, Paulus G (1997) Astron Astrophys 320:460
Meynet G, Hirschi R, Maeder A, Ekström S (2006) In: Montmerle T, Kahane C (eds) EAS publications series, vol 19, pp 85–100
Naya JE, Barthelmy SD, Bartlett LM et al (1996) Nature 384:44
Neronov A, Meynet G (2016) Astron Astrophys 588:A86
Nittler LR, Alexander CMO, Gallino R et al (2008) Astrophys J 682:1450
Oberlack U, Bennett K, Bloemen H et al (1996) Astron Astrophys Suppl Ser 120:C311
Olano CA (1982) Astron Astrophys 112:195
Ore A, Powell JL (1949) Phys Rev 75:1696
Ostdiek KM, Anderson TS, Bauder WK et al (2017) Phys Rev C 95:055809
Palacios A, Meynet G, Vuissoz C et al (2005) Astron Astrophys 429:613
Panther FH, Crocker RM, Birnboim Y, Seitenzahl IR, Ruiter AJ (2018) Mon Not R Astron Soc 474:L17
Parikh A, José J, Karakas A, Ruiz C, Wimmer K (2014) Phys Rev C 90:038801
Pecaut MJ, Mamajek EE (2016) Mon Not R Astron Soc 461:794
Perrot CA, Grenier IA (2003) Astron Astrophys 404:519
Pignatari M, Herwig F, Hirschi R et al (2016) Astrophys J Suppl 225:24
Plüschke S, Diehl R, Schönfelder V et al (2001a) In: Gimenez A, Reglero V, Winkler C (eds) Exploring the gamma-ray universe. ESA special publication, vol 459, pp 55–58
Plüschke S, Kretschmer K, Diehl R, Hartmann DH, Oberlack UG (2001b) In: Gimenez A, Reglero V, Winkler C (eds) Exploring the gamma-ray universe. ESA special publication, vol 459, pp 91–95
Plüschke S, Cerviño M, Diehl R et al (2002) New Astron Rev 46:535
Pöppel W (1997) Fundam Cosm Phys 18:1
Pöppel WGL, Bajaja E, Arnal EM, Morras R (2010) Astron Astrophys 512:A83+
Prantzos N (1993) Astron Astrophys Suppl Ser 97:119
Prantzos N (2004) Astron Astrophys 420:1033
Prantzos N (2006a) αp 449:869
Prantzos N (2006b) Astron Astrophys 449:869
Prantzos N (2012) Astron Astrophys 538:A80
Prantzos N, Diehl R (1996) Phys Rep 267:1
Prantzos N, Arnould M, Arcoragi JP, Casse M (1985) In: Jones FC (ed) International cosmic ray conference, vol 3, pp 167–170
Prantzos N, Boehm C, Bykov AM et al (2011) Rev Mod Phys 83:1001
Preibisch T, Zinnecker H (1999) Astron J 117:2381
Preibisch T, Mamajek E (2008) In: Reipurth B (ed) The nearest OB association: Scorpius-Centaurus (Sco OB2), pp 235
Preibisch T, Brown AGA, Bridges T, Guenther E, Zinnecker H (2002) Astron J 124:404
Ptuskin VS, Soutoul A (1998) Space Sci Rev 86:225
Purcell WR, Grabelsky DA, Ulmer MP et al (1993) Astrophys J 413:L85
Purcell WR, Cheng L-X, Dixon DD (1997) Astrophys J 491:725+
Ragot BR (1999) Astrophys J 518:974

Ragot BR (2006) Astrophys J 642:1163
Ramaty R, Kozlovsky B, Lingenfelter RE (1979) Astrophys J Suppl 40:487
Robin AC, Reylé C, Derrière S, Picaud S (2003) Astron Astrophys 409:523
Rugel G, Faestermann T, Knie K et al (2009) Phys Rev Lett 103:072502
Schramm DN, Tera F, Wasserburg GJ (1970) Earth Planet Sci Lett 10:44
Schulreich MM, Breitschwerdt D, Feige J, Dettbarn C (2017) Astron Astrophys 604:A81
Siegert T (2017) PhD thesis, TU Munich
Siegert T, Diehl R (2017) In: Kubono S, Kajino T, Nishimura S, Isobe T, Nagataki S, Shima T, Takeda Y (eds) 14th international symposium on nuclei in the cosmos (NIC2016), pp 020305
Siegert T, Diehl R, Greiner J et al (2016a) Nature 531:341
Siegert T, Diehl R, Khachatryan G et al (2016b) Astron Astrophys 586:A84
Siegert T, Diehl R, Vincent AC et al (2016c) ArXiv e-prints 1608.00393
Sieverding A, Martínez-Pinedo G, Langanke K, Heger A (2017) In: Kubono S, Kajino T, Nishimura S, Isobe T, Nagataki S, Shima T, Takeda Y (eds) 14th international symposium on nuclei in the cosmos (NIC2016), pp 020701
Sizun P, Cassé M, Schanne S (2006) Phys Rev D 74:063514
Skinner G, Diehl R, Zhang X-L, Jean P (2014) Proc Sci INT2014:054
Slesnick CL, Hillenbrand LA, Carpenter JM (2008) Astrophys J 688:377
Smith DM (2004) In: Schoenfelder V, Lichti G, Winkler C (eds) 5th integral workshop on the integral universe. ESA special publication, vol 552, pp 45–+
Soutoul A, Casse M, Juliusson E (1978) Astrophys J 219:753
Srinivasan G, Chaussidon M (2013) Earth Planet Sci Lett 374:11
Strong AW, Moskalenko IV, Ptuskin VS (2007) Annu Rev Nucl Part Sci 57:285–327. http://dx.doi.org/10.1146/annurev.nucl.57.090506.123011
Sturner SJ, Naya JE (1999) Astrophys J 526:200
Sukhbold T, Ertl T, Woosley SE, Brown JM, Janka H-T (2016) Astrophys J 821:38
Sunyaev R, Churazov E, Gilfanov M et al (1992) Astrophys J 389:L75+
Taylor JH, Cordes JM (1993) Astrophys J 411:674
Thielemann F-K, Nomoto K, Hashimoto M-A (1996) Astrophys J 460:408
Tibaldo L, Grenier IA (2013) Nucl Phys B Proc Suppl 239:70
Timmes FX, Woosley SE, Hartmann DH et al (1995) Astrophys J 449:204
Toptygin IN (1985) Cosmic rays in interplanetary magnetic fields. D. Reidel Publishing Co., Dordrecht
Uyanıker B, Fürst E, Reich W, Aschenbach B, Wielebinski R (2001) Astron Astrophys 371:675
van der Hucht KA (2001) New Astron Rev 45:135
Voss R, Diehl R, Hartmann DH et al (2009) Astron Astrophys 504:531
Voss R, Diehl R, Vink JS, Hartmann DH (2010) Astron Astrophys 520:A51+
Wallner A, Feige J, Kinoshita N et al (2016) Nature 532:69
Wang W, Harris MJ, Diehl R et al (2007) Astron Astrophys 469:1005
Wang W, Lang MG, Diehl R et al (2009) Astron Astrophys 496:713
Wasserburg GJ, Lee T, Papanastassiou DA (1977) Meteoritics 12:377
Weidenspointner G, Shrader CR, Knödlseder J (2006a) Astron Astrophys 450:1013+
Weidenspointner G, Shrader CR, Knödlseder J et al (2006b) Astron Astrophys 450:1013
Weidenspointner G, Skinner G, Jean P et al (2008) Nature 451:159
Welsh BY, Shelton RL (2009) Astrophys Space Sci 323:1
Westphal AJ, Bradley JP (2004) Astrophys J 617:1131
Wiedenbeck ME, Binns WR, Christian ER et al (1999) Astrophys J 523:L61
Wiedenbeck ME, Binns WR, Cummings AC et al (2007) In: von Steiger R, Gloeckler G, Mason GM (eds) An overview of the origin of galactic cosmic rays as inferred from observations of heavy ion composition and spectra. Springer, New York, pp 415–+
Wilking BA, Gagné M, Allen LE (2008) In: Reipurth B (ed) Star formation in the ρ Ophiuchi molecular cloud, pp 351
Woosley SE, Heger A (2007) Phys Rep 442:269

Woosley SE, Weaver TA (1994) Astrophys J 423:371
Woosley SE, Weaver TA (1995) Astrophys J Suppl 101:181
Yanasak NE, Wiedenbeck ME, Mewaldt RA et al (2001) Astrophys J 563:768
Zinnecker H, Yorke HW (2007) Annu Rev Astron Astrophys 45:481